THE UNIVERSITY of ADELAIDE

Tailoring Cathode Nanostructures for Performance Improvement of Non-Aqueous Lithium-Oxygen Batteries

Heng Wang

A thesis submitted for the degree of Doctor of Philosophy

School of Chemical Engineering and Advanced Materials

The University of Adelaide

July 2019

Table of contents

Abstracts

Non-aqueous Li-O_2 battery has emerged as a promising energy storage technology. Unlike other intercalation-based methods, Li ions react with ambient oxygen directly, leading to a high specific energy density of up to 3600 W h kg^{-1} (energy per the mass of Li_2O_2), which is several times higher than that of the state-of-the-art Li-ion batteries. However, the low round-trip efficiency and poor cycling stability of non-aqueous Li-O_2 batteries have hindered their commercial use. This thesis aims to develop novel cathode materials by tailoring their nanostructures to improve the performance of non-aqueous Li-O_2 batteries and gain an in-depth understanding of the battery electrochemistry.

First, the relationship between the electrocatalyst structure and battery performance is explored through the investigation of $NiCo_2O_4$ (NCO) cathode materials as a model example. The {111} and {112} crystal planes exposed NCOs with identical morphology were developed via a hydrothermal method followed by calcination. The contribution of NCO nanostructures to their electrocatalytic activities was systematically evaluated through the investigation of crystal plane effects, surface areas and bulk compositions of cathodic NCOs. The {112} crystal planes are more active than {111} due to its availability to abundant dangling bonds and active octahedral Co^{3+} and Ni^{3+} sites. Ni^{3+} can improve oxygen evolution reaction (OER) activity and conductance, promoting the electrocatalytic performance of NCO. The NCO nanoplates with exposed {112} crystal planes, high surface areas and good conductance are identified as an ideal cathode material.

Next, macroporous nanocomposites of reduced graphene oxide aerogels (GA) and NCO nanoplates were developed via a one-pot self-assembly approach and used as freestanding cathodes. In these cathodes, NCO nanoplates can fully cover the walls of the macropores,

which provides active sites toward OER and protects GA support from corrosion. Moreover, the macroporous GA support can facilitate the mass and electron transportation as well as act as accommodation sites for Li_2O_2 discharge product. After systematic optimization, the nanocomposite cathode with a GA: NCO weight ratio of 1: 4 displays superior battery performance due to its optimal conductance and NCO coverage on the walls of macropores. Last, freestanding macroporous NCO@carbon nanotubes (CNT) cathodes were fabricated through a vacuum filtration-assisted self-assembly method followed by template removal to generate macropores. The surfaces of NCO@CNT are found to promote the formation of amorphous Li_2O_2 with improved conductivity. As a result, the layer can grow up to 50 nm before the cathode is fully passivated, which boosts Li_2O_2 production and discharge capacity of the batteries. During charge, the improved conductivity of amorphous Li_2O_2 promotes OER kinetics, leading to excellent cycling performance. The amorphous Li_2O_2 layer can be a viable alternative to crystalline Li_2O_2 toroid as the discharge product of high-performance Li-O_2 batteries.

Through systematic investigation of the structures of electrocatalysts and their supports on the electrocatalytic activities and discharge product properties, the correlations between cathode nanostructures and the battery performance have been established. These results provide insights into the underlying mechanisms of the electrochemistry and pave paths for the future rational designs of novel cathode materials in high-performance non-aqueous Li-O_2 batteries.

Thesis Declaration

I certify that this work contains no material which has been accepted for the award of any other degree or diploma in my name in any university or other tertiary institution and, to the best of my knowledge and belief, contains no material previously published or written by another person, except where due reference has been made in the text. In addition, I certify that no part of this work will, in the future, be used in a submission in my name for any other degree or diploma in any university or other tertiary institution without the prior approval of the University of Adelaide and where applicable, any partner institution responsible for the joint award of this degree.

The author acknowledges that copyright of published works contained within this thesis resides with the copyright holder(s) of those works.

I give permission for the digital version of my thesis to be made available on the web, via the University's digital research repository, the Library Search and also through web search engines, unless permission has been granted by the University to restrict access for a period of time.

Heng Wang

Signature:

Date: 17/07/2019

Acknowledgments

First, I would like to express my sincere gratitude towards my principle supervisor Prof. Sheng Dai and my co-supervisors Prof. Shizhang Qiao and Prof. Haihui Wang for their invaluable advices, guidance and support. Without them, it would be impossible for me to complete my research and this thesis.

I would like to express my gratefulness towards my colleagues at my laboratory for their continuous help with my research. They are Qi Bi, Dr. Yusak Hartanto, Afshin Karami, Huanyu Jin, Laiquan Li, Dr. Jinlong Liu, Xin Liu, Hesamoddin Rabiee, Dr Jingrun Ran, Qieqiong Shan, Yang Shi, Dr. Aabhash Shrestha, Xuesi Wang, Dr. Cui Xiaolin, Fangxi Xie, Chaochen Xu, Chao Ye, Seonho Yun, Dr. Bo You, Yongqiang Zhao, Jiabing Zhang, Dr. Ke Zhang, Yechuan Zhang, Dr. Pei Zheng, Xing Zhi, Dr. Dongdong Zhu. In addition, I would like to thank Dr. Chunxian Guo, Dr. Qiuhong Hu, Dr. Yan Jiao, Jason Peak, Dr. Diana Tran, Dr. Zheng Yao from the School of Chemical Engineering and Advanced Materials, and Dr Animesh Basak, Dr Lisa O'Donovan, Ken Neubauer, Dr Ashley Slattery, Lyn Waterhouse from Adelaide Microscopy for their technological assistance. Special thanks to Prof. Ping Chen from Anhui University and Prof. Jingtao Wang from Zhengzhou University for their suggestions on my experiments. My research has been benefited greatly from them.

Furthermore, I would like to give my thankfulness to my friends Lawrence Hryb, Wenwen Liu, Phil Spencer, Mo Shi, Yin Shu, Zheyang Wei for their company and support.

Last but not least, I give my sincerest appreciation and love to my parents and family in China. Without their encouragements and support, I would never achieve what I have today.

Chapter 1 Introduction

1.1. Background

With increasing concern regarding carbon emission and climate change, the transformation from fossil fuels to renewable energy is inevitable. There has been significant growth in renewable energy in Australia in the past two decades. In 2017, Australia produced over 38000 GWh of renewable energy, which is nearly 17% of the total production, and it is estimated that half of the electricity generated will be from renewable sources by 2030[1]. Renewable energy technologies such as wind and solar generally have variable outputs, which do not always coincide electric demand. Energy storage technologies, such as batteries, can ensure the electricity supply from renewable sources matches the demand reliably, even when the sources are unavailable. Therefore, they are the keys to integrating renewable energy into the current electric grid. The integration of energy storage technologies is rapidly growing around the globe. For instance, the state of South Australia is leading the way in the integration, with the world largest lithium battery (the 100MW/129MWh battery) already operational and several other projects, such as the 150MW SolarReserve Aurora Solar plant and the 250MW Virtual Power Plant for 50000 households[2] on the way.

However, it is unlikely current Li-ion technology is sufficient to meet the demand in the long run. Bruce et al.[3] provided a comprehensive comparison of practical specific energies for existing and future battery technologies, and their equivalent driving ranges in electric vehicles (EVs) (Figure 1.1). Among the proposed future technologies such as Zn-O_2, Li-S and Li-O_2 batteries, only Li-O_2 system is expected to reach the driving range goal of ~500 km between charges. To that end, the Li-O_2 system has gained much attention as one of the most promising energy storage technology, especially for EVs. To date, the development of

Li-O_2 batteries is still in its infancy, and there are paramount challenges to overcome before commercialization is possible.

In pursuit of practical Li-O_2 batteries, four systems, namely non-aqueous, aqueous, hybrid, and solid-state system, are proposed[4]. The latter three systems possess a stringent requirement for the separator to protect Li anode and facilitate Li^+ transport; therefore, the non-aqueous system is considered the most favorable[4]. In a typical non-aqueous Li-O_2 battery, O_2 is reduced during discharge through an oxygen reduction reaction (ORR) and combines Li^+ to form Li_2O_2 on cathode surfaces. Li_2O_2 is reversibly decomposed during charge via an oxygen evolution reaction (OER) to release O_2. Li_2O_2 proves to be problematic because it is insoluble in the electrolyte, which hinders efficient cathode usage and limits discharge capacity. In addition, Li_2O_2 is insulating, which shows sluggish kinetics during discharge and charge. Moreover, Li_2O_2 is reactive towards parasitic reactions, leading to low round-trip efficiency, high polarization and poor long-term stability for the batteries[5–8]. Because all electrochemical reactions during ORR and OER occur on cathode surfaces, the rational design of cathode is of utter importance. In the past decade, numerous carbons, precious metals and transition metal oxides-based cathode materials have been proposed. Unfortunately, none of these cathode materials are sufficiently active and stable for practical Li-O_2 batteries. Therefore, it is significant but challenging to develop novel cathode materials that can efficiently accommodate Li_2O_2, promote the decomposition of Li_2O_2 under low voltage and are stable against parasitic reactions.

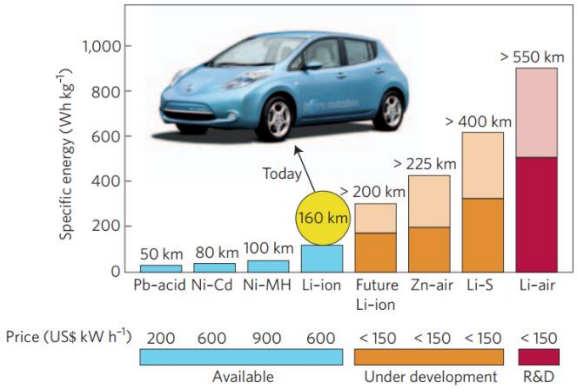

Figure 1.1. Practical specific energies for rechargeable batteries along with estimated driving distances and pack prices. For future technologies, a range of anticipated specific energies is given as shown by the lighter shaded region. The values for driving ranges are based on the minimum specific energy for each technology and scaled on the specific energy of the Li-ion cells and driving range of the Nissan Leaf.[3] The figure is reproduced with permission from Ref 3.

1.2. Aim and Objectives

The aim of this thesis is to design and synthesize effective and stable nanostructured cathode materials and illuminate the underlying structure-performance relations for non-aqueous Li-O_2 batteries. The specific objectives are as follows.

(1) To identify highly active $NiCo_2O_4$ (NCO) cathode materials and understand the design principles for high-performance cathodes through the investigation of surface atomic arrangement, surface areas and bulk compositions;

(2) To design and synthesize a macroporous reduced graphene oxide aerogel framework to support the above-optimized NCO and investigate the syngenetic effect between the aerogel support and NCO electrocatalysts to optimize the performance of the cathode;

(3) To explore the effect of NCO nanoparticles on the morphologies, crystallinities and spatial distributions of the discharge product and gain insights into novel cathode designs based on an alternative surface growth pathway; to design a freestanding cathode with

the proper porous structure for surface growth pathway to overcome the small discharge capacity issue with this pathway.

1.3. Thesis Layout

This thesis contains six chapters. Chapter 1 introduces the significance and objectives of the thesis. Chapter 2 presents a critical review of the cathode designs in non-aqueous Li-O_2 batteries. The mechanisms during the discharging and charging processes and their implications on the cathode design are discussed in detail. The recent development in cathode materials is also assessed. In Chapter 3, NCO nanoplates with exposed highly active crystal planes, high surface areas and high conductance are first developed as an effective electrocatalyst, which paves way for the development of novel macroporous cathode. In Chapter 4, the NCO nanoplates proposed in Chapter 3 are used in conjunction with macroporous reduced graphene oxide aerogel to fabricate a macroporous cathode for the effective accommodation of Li_2O_2 discharge product via the solution growth pathway. Chapter 5 explores the effect of NCO on the morphologies and crystallinities of the discharge product and presents a novel macroporous NCO@carbon nanotubes cathode that promotes the deposition of thick amorphous Li_2O_2 layer via surface growth pathway on cathode surfaces, which significantly improves the discharge capacity and cycling performance. Finally, Chapter 6 summarizes the key achievement of this thesis and provides perspectives for potential future work.

References

(1) Clean Energy Council. Clean Energy Australia Report 2018 https://www.cleanenergycouncil.org.au/resources/resources-hub/clean-energy-australia-report.

(2) Hendriks, M. South Australia Leads the Way in Energy Storage Integration. *Energy News* **2018**, *36* (1), 15.

(3) Bruce, P. G.; Freunberger, S. A.; Hardwick, L. J.; Tarascon, J.-M. Li-O_2 and Li-S Batteries with High Energy Storage. *Nat. Mater.* **2012**, *11* (1), 19–29.

(4) Lyu, Z.; Zhou, Y.; Dai, W.; Cui, X.; Lai, M.; Wang, L.; Huo, F.; Huang, W.; Hu, Z.; Chen, W. Recent Advances in Understanding of the Mechanism and Control of Li_2O_2 Formation in Aprotic Li-O_2 Batteries. *Chem. Soc. Rev.* **2017**, *46* (19), 6046–6072.

(5) Belova, A. I.; Kwabi, D. G.; Yashina, L. V.; Shao-Horn, Y.; Itkis, D. M. Mechanism of Oxygen Reduction in Aprotic Li-Air Batteries: The Role of Carbon Electrode Surface Structure. *J. Phys. Chem. C* **2017**, *121* (3), 1569–1577.

(6) Wang, L.; Zhang, Y.; Liu, Z.; Guo, L.; Peng, Z. Understanding Oxygen Electrochemistry in Aprotic Li-O_2 Batteries. *Green Energy & Environment* **2017**, *2* (3), 186–203.

(7) Wang, Y.; Yuan, H. Discharge Precipitate's Impact in Li-Air Battery: Comparison of Experiment and Model Predictions. *J. Electrochem. Soc.* **2017**, *164* (9), A2283–A2289.

(8) Zhao, Z.; Huang, J.; Peng, Z. Achilles' Heel of Lithium-Air Batteries: Lithium Carbonate. *Angew. Chem. Int. Ed.* **2018**, *57*, 2–15.

Chapter 2 Literature Review

This chapter provides a critical review on Li_2O_2 formation mechanism during oxygen reduction reaction (ORR) and Li_2O_2 decomposition mechanism during oxygen evolution reaction (OER). Recent advances in novel cathode designs are also highlighted.

2.1. Li_2O_2 Formation during ORR

In this section, the electrochemistry of non-aqueous Li-O_2 batteries during the discharge process is discussed. Solid Li_2O_2 is formed and deposited at cathode surfaces as the discharge product. The morphologies and spatial distributions of the insoluble Li_2O_2 have a significant impact on both discharge and charge performance of non-aqueous Li-O_2 batteries. Therefore, it is essential to identify key factors that affect Li_2O_2 property and production, which will aid the rational design of high-performance cathode materials. Alternative discharge products and mechanisms for novel non-aqueous Li-O_2 systems will also be discussed.

2.1.1. Mechanisms of Li_2O_2 Formation

In a typical non-aqueous Li-O_2 battery, the formation of Li_2O_2 discharge product is considered as multi-step reactions[1–3]. Oxygen is first adsorbed on surface active sites (S) to generate surface adsorbed O_2^* (the * denotes adsorbed species):

$$O_2 + S \rightarrow O_2^* \tag{2.1}$$

Then, O_2^* is chemically reduced on cathode surfaces and reacts with Li^+ to form surface adsorbed LiO_2^*:

$$O_2^* + e^- + Li^+ \rightarrow LiO_2^* \tag{2.2}$$

Finally, LiO_2^* can directly undergo an electrochemical reduction process to form Li_2O_2 via:

$$LiO_2^* + Li^+ + e^- \rightarrow Li_2O_2 \quad (2.3)$$

or Li_2O_2 can be generated through a chemical disproportionation of LiO_2^*:

$$2LiO_2^* \rightarrow Li_2O_2 + O_2 \quad (2.4)$$

The electrochemical reduction pathway through equations (2.1)-(2.3) is favored because its kinetic barrier is lower[4,5]. In this pathway, the surface adsorbed LiO_2^* directly accepts an electron from cathode surfaces to from Li_2O_2 and is therefore referred to as the surface growth pathway. Alternatively, experimental evidence[6–8] suggests that the equation (2.2) can consist of two solution steps. The dissolved oxygen in the electrolyte can directly trap an electron via:

$$O_2 + e^- \rightarrow O_{2(sol)}^- \quad (2.2a)$$

then the O_2^- combines with Li^+ to form LiO_2 that nucleates in solution via:

$$O_{2(sol)}^- + Li^+ \rightarrow LiO_{2(sol)} \quad (2.2b)$$

The solvated $LiO_{2(sol)}$ can generate Li_2O_2 in solution via a chemical disproportionation pathway through equation (2.4), and this is referred to as solution growth pathway.

The growth of Li_2O_2 formed via these pathways results in drastically different morphologies[9,10]. For the surface growth pathway, Li_2O_2 is formed on cathode surfaces via the electrochemical reduction of LiO_2^*, which leads to direct and homogenous deposition of Li_2O_2 on cathode surfaces with a layer morphology. The close contact of the Li_2O_2 layer with cathode can enhance the kinetics and reduce the potential[11] during battery charge, which improves the round-trip efficiency and long-term stability of battery. However, due to the low electrical conductivity (10^{-12} to 10^{-13} S cm^{-1})[12] of bulk Li_2O_2, the layer cannot grow thicker than 5-10 nm. Beyond this thickness, electrons cannot tunnel through the layer to sustain the electrochemistry, and cathode surfaces are passivated, which prevents further

Li_2O_2 production and results in small discharge capacity[13,14]. For the solution growth pathway, Li_2O_2 is first formed in electrolyte solution; when its concentration exceeds the solubility limit, Li_2O_2 crystallites precipitate on the nucleation sites of cathode surfaces and grow into large (up to several micrometers) toroids. Mitchell et al.[15] described the formation mechanism of these large toroids in detail: initially, thin (~10 nm) Li_2O_2 plates grow roughly parallel to each other to form small Li_2O_2 disks, then, additional plates nucleate in the void space between the splayed plates to form a rim around the disks, eventually resulting in the characteristic toroidal morphology. These toroids are formed in the pores of cathode and away from cathode surfaces, delaying the blockage of the electrochemically active surface area on cathode surfaces. This allows a much higher Li_2O_2 production and large discharge capacity performance before cathode surfaces are fully passivated[16]. However, the efficient decomposition of these large toroids is difficult, which often leads to high potential during battery charge. In brief, surface growth pathway shows low charge potential but small capacity, while the solution growth pathway shows high charge potential but large capacity (Figure 2.1a).

The discharge current density of the battery is a critical descriptor for determining Li_2O_2 formation pathway. It is often observed that Li_2O_2 toroids are dominantly formed at a low current density while thin Li_2O_2 layers tend to be produced at a high current density[1] (Figure 2.1b). At a low current density, the electron transportation is slower than LiO_2 solvation, so equation (2.4) is more favorable than equation (2.3), and the solution growth pathway is dominant. At a high current density, the fast electron transportation can generate a high concentration of LiO_2^*, which promotes equation (2.3) and suppresses equation (2.4), and the surface growth pathway is favored. Furthermore, the size of Li_2O_2 toroids in solution

growth pathway is also current density-dependent. Lau et al.[18] described a model (Figures 2.1c and 2d) for the nucleation and growth of Li_2O_2 toroids and proposed that the high current density can cause the crowding of the nuclei and a reduction of Li_2O_2 particle size, which ultimately results in lower Li_2O_2 production on cathode surfaces.

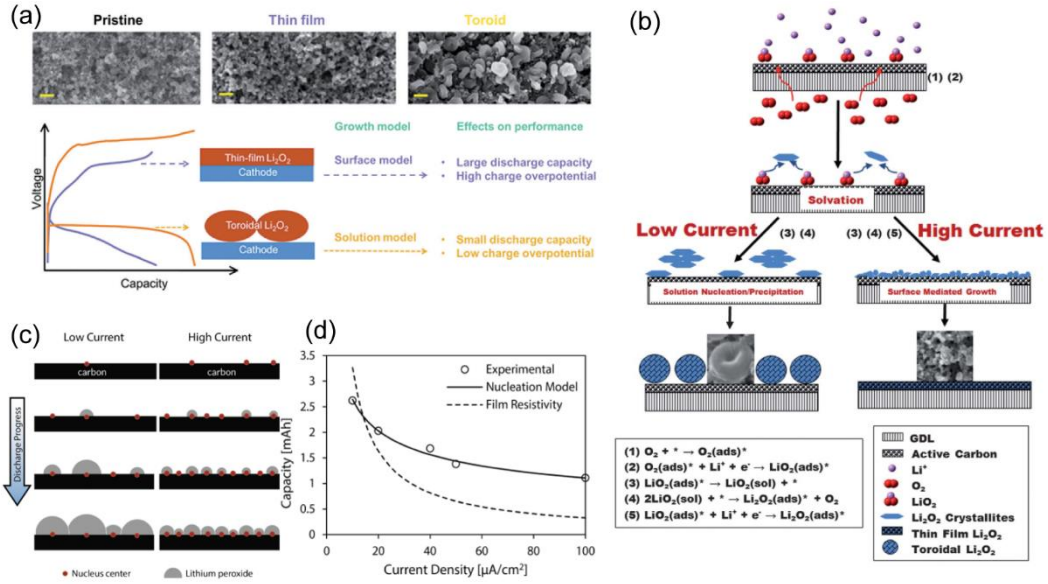

Figure 2.1. (a) SEM images of the cathodes with thin-film and toroidal Li_2O_2 morphologies (scale bars indicate 400 nm) and their scheme for the effect of the typical Li_2O_2 morphologies on battery performance via different pathways; (b) scheme of ORR mechanism as a function of the current density; (c) scheme of the effect of current density on nucleation rate and the final amount of Li_2O_2 deposited; (d) fit of capacity as a function of current density. Figures are reproduced with permission from (a) ref 17, (b) ref 1, (c, d) ref 18.

2.1.2. Effect of Cathode Materials on Li_2O_2 Formation

Controlling the formation of Li_2O_2 with desirable morphology is crucial for high-performance non-aqueous Li-O_2 battery. In practice, Li-O_2 batteries are almost always tested under low current density conditions, and electrolytes employed can always solvate LiO_2^* to some extent, both of which promote the solution growth pathway. Therefore, the toroid Li_2O_2 formation via the solution growth pathway is dominantly observed on most cathode materials. However, Yimaz et al.[19] first provided experimental evidence that a RuO_2/MWCNT cathode can generate Li_2O_2 with a thin layer morphology at a current density that toroid Li_2O_2 would typically occur (Figure 2.2a). It is proposed that RuO_2 nanoparticles show strong O_2 adsorption, which results in the formation of Li_2O_2 with a layer morphology via the surface growth pathway. Later, Yang et al.[20] reported that on a Pd/graphene cathode, worm-like small Li_2O_2 particles that can cover most cathode surfaces are formed via the surface growth pathway. Density functional theory studies reveal that Pd in Pd/graphene cathode shows strong LiO_2 adsorption, so Li_2O_2 can be formed via the direct electrochemical reduction of LiO_2 and cover most cathode surfaces (Figure 2.2b).

Evidently, the adsorption ability of O_2 and LiO_2 on cathode surfaces play a critical role in determining Li_2O_2 formation pathway. Recently, the correlation between the cathode O_2 adsorption ability and the Li_2O_2 formation pathway is established by Lyu et al.[21] For the cathodes with strong O_2 adsorption (e.g., Co_3O_4), surface adsorbed O_2^* can accept an electron directly from cathode surfaces via an inner-sphere electron transfer mechanism (ISET), which favors the surface growth pathway to form thin Li_2O_2 layer (Figure 2.2c). For the cathodes with weak O_2 adsorption (e.g., CNT), the solvated $O_{2(sol)}$ can trap an electron

via an out-sphere electron transfer mechanism (OSET), which favors the solution growth pathway to form large Li_2O_2 toroids (Figure 2.2d). The ISET and OSET mechanisms are determined by the double-layer structure[22] of cathodes. For cathodes with strong O_2 adsorption, the direct electron transfer to surface adsorbed O_2^* is dominant at the inner Helmholtz plane (IHP) via ISET, leading to the direct reduction of LiO_2^* for surface growth pathway. While on cathodes with weak O_2 adsorption, electrons can transfer from the inner Helmholtz plane to the outer Helmholtz plane (OHP) via OSET (Figure 2.2e), which enables the formation of $LiO_{2(sol)}$ for the solution growth pathway. The correlation of battery performance and Li_2O_2 morphology controlled via O_2 adsorption is summarized in Figure 2.2f.

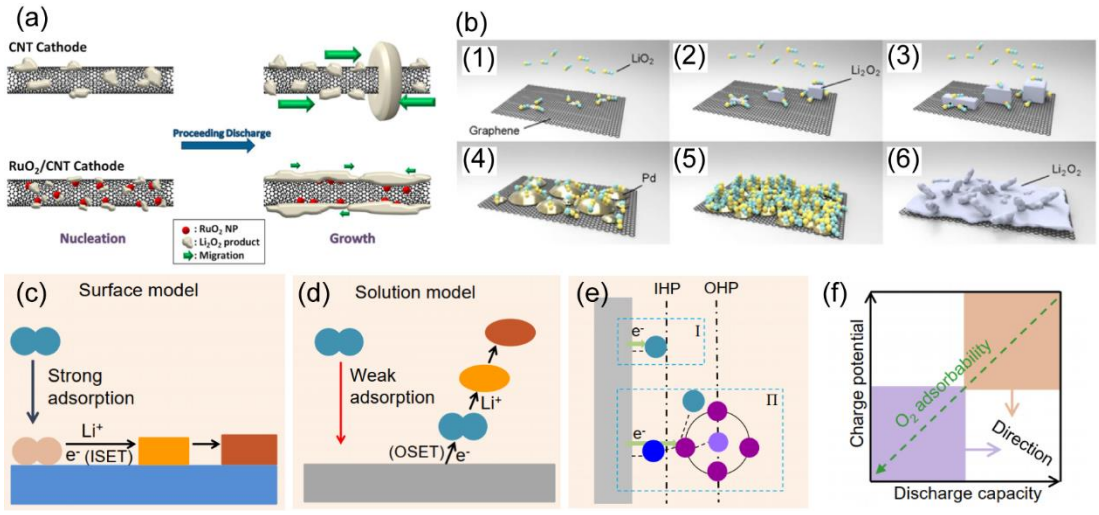

Figure 2.2. (a) Scheme of the toroid Li_2O_2 formation on CNT cathode and the layer Li_2O_2 formation on RuO_2/CNT cathode; (b) scheme of Li_2O_2 formation process on graphene and Pd/G electrodes; (c) scheme of Li_2O_2 growth on cathode with strong O_2 adsorption and (d) Li_2O_2 growth on cathode with weak O_2 adsorption; (e) scheme of double-layer structure with IHP and OHP, the ISET and OSET mechanisms are demonstrated in rectangles I and II; (f) plot of the correlation of performance and Li_2O_2 morphology controlled via O_2 adsorption. Figures are reproduced with permission from (a) ref 19, (b) ref 20, (c-f) ref 21.

As previously pointed out, the solution growth pathway shows superior capacity performance to the surface growth pathway. To that end, the solution growth pathway is preferred, and recent research focuses on macroporous cathode designs with high pore volume, such as hierarchical cathodes with open-end nanostructures, to accommodate large Li_2O_2 deposited in the macropores. For instance, Liu et al.[23] designed a hierarchical $NiCo_2O_4$ nanowire array on carbon cloth cathode. Large Li_2O_2 particles (1 μm) are grown on the tips of the $NiCo_2O_4$ instead of carbon surfaces so that carbon passivation is delayed (Figure 2.3a). To promote the capacity in the solution growth pathway further, a general strategy is to suppress the nucleation of Li_2O_2 particles so these particles can grow as large as possible before cathode surfaces are fully covered[18]. For example, Lu et al.[24] demonstrated that by covering carbon cathode defect sites that will otherwise act as nucleation sites, the size of the Li_2O_2 particle grows from ~200 nm on carbon cathode to ~ 1 μm on the Al_2O_3 coated carbon cathode (Figure 2.3b). Similarly, Tran et al.[25] modified carbon surfaces with long-chain hydrophobic molecules, which deactivates the -OH defects as potential nucleation sites. The modified carbon cathode demonstrates a five-fold increase in capacity in comparison with the non-modified carbon.

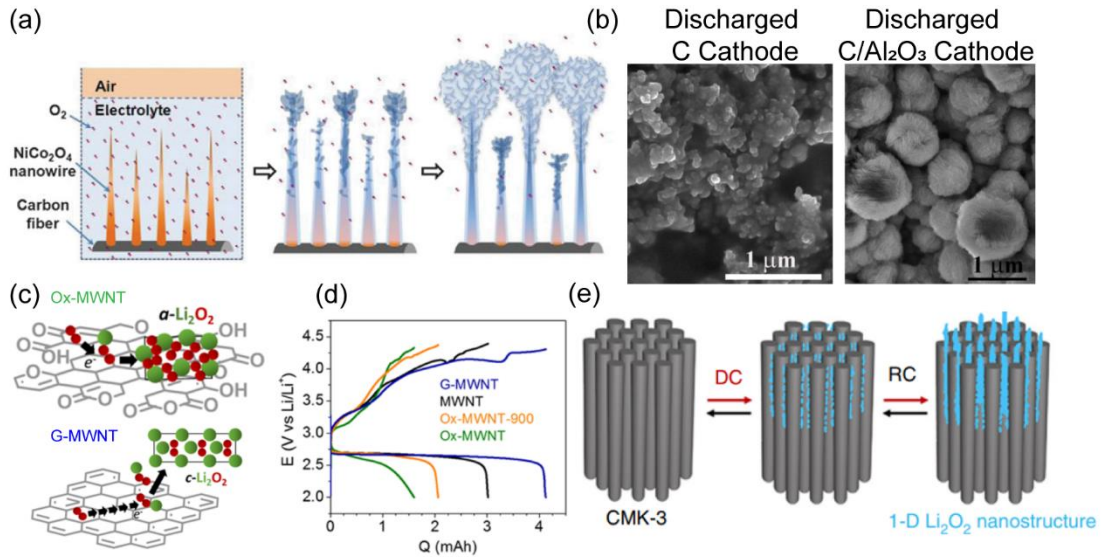

Figure 2.3. (a) Scheme of the morphological evolution of cathode for nucleation and growth of large Li_2O_2 on $NiCo_2O_4$@CF cathode; (b) comparison of Li_2O_2 morphologies on fully discharged C and C/Al_2O_3 cathode; (c) scheme of the formation of *a*-Li_2O_2 on Ox-MWNT and *c*-Li_2O_2 on G-MWNT; (d) galvanostatic discharge and charge profiles of the Ox-MWNT, Ox-MWNT-900, MWNT and G-MWNT cathodes at 50 mA g^{-1}; (e) scheme of growth of Li_2O_2 (blue) from CMK-3 electrode. Figures are reproduced with permission from (a) ref 23, (b) ref 24, (c, d) ref 26, (e) ref 27.

Although large Li_2O_2 toroids generated via the solution growth pathway can significantly improve the discharge capacity of non-aqueous Li-O_2 batteries, the inefficient decomposition of these large, well-crystalline particles is often attributed to the high potential during charge. For this reason, some researchers seek novel cathode materials with proper surface structures to shift Li_2O_2 formation towards surface growth pathway. Previously, the thin layer formations are only observed on precious metals and their oxides[19,20,28,29]. Based on the work of Lyu et al.[21], the formation of Li_2O_2 layers is ascribed to the superior oxygen adsorption of the precious metals[19]. Cathode surfaces can then be designed accordingly to enhance the O_2 adsorbability without resorting to the expensive precious metals. For example, Wong et al.[26] tailored the surfaces of multi-walled CNT

(MWNT) to obtain oxygen-functioned MWNT (Ox-MWNT), oxygen-functioned MWNT with heat treatment-induced defects (Ox-MWNT-900), and highly ordered graphitic MWNT (G-MWNT). G-MWNT displays weak $O_2(LiO_2)$ adsorption, leading to the formation of crystalline Li_2O_2 (*c*-Li_2O_2) via solution growth pathway while Ox-MWNT shows strong $O_2(LiO_2)$ adsorption, which favors the surface growth pathway to form amorphous Li_2O_2 (*a*-Li_2O_2) layer (Figure 2.3c). Ox-MWNT displays lower charge potential but only deliver less than half the capacity of G-MWNT cathode (Figure 2.3d).

The low discharge capacity issue with surface growth pathway is mainly caused by the thin Li_2O_2 layer, which cannot efficiently utilize the pore volume in macroporous cathodes[21]. Ideally, in order to achieve high discharge capacity, Li_2O_2 layer should be deposited on a rationally designed ultra-porous cathode with ultra-high surface area and small pores, such as two-dimensional metal or metal oxides[17]. The design of such cathode remains challenging, especially considering such small pores can be easily blocked. Very recently, Dutta et al.[27] proposed a mesoporous carbon cathode (CMK-3) with micropores (0.71 nm) and small mesopores (3.74 nm) together with ultra-high BET surface area (1128 $m^2\ g^{-1}$). The cathode can modulate the growth of Li_2O_2 to produce a one-dimensional Li_2O_2 with a high surface area (Figure 2.3e). However, this novel cathode is still susceptible to pore clogging, especially at a higher current density[27]. Alternatively, because the thickness of the Li_2O_2 layer is fundamentally limited by the poor conductivity of the bulk Li_2O_2, it is possible to improve the layer thickness as well as battery capacity by promoting the formation of non-crystalline Li_2O_2 with enhanced conductivity. For example, for the previously mentioned RuO_2/MWCNT cathode[19], RuO_2 nanoparticles are proposed to show strong adsorption towards O_2 as well as weak adsorption towards Li^+, which leads to the formation of Li

vacancy-rich and poorly crystalline Li_2O_2. The Li_2O_2 layer with improved conductivity can grow to ~20 nm in thickness, which exceeds the 5-10 nm limitation of bulk crystalline Li_2O_2.

2.1.3. Effect of Electrolyte on Li_2O_2 Formation

As mentioned before, the LiO_2^* intermediate plays a critical role in the formation of Li_2O_2, and by increasing the $O_2(LiO_2)$ adsorption ability of the cathode, the Li_2O_2 formation can be shifted towards surface growth pathway. On the other hand, if LiO_2^* is soluble in the electrolyte, the solution growth pathway can be promoted. Although electrolyte does not directly affect cathode designs, because electrolyte can drastically alter the formation and deposition of Li_2O_2, the compatibility between cathodes and electrolyte should be taken into consideration.

Several parameters for the electrolyte, including the Gutmann donor number (DN) of the solvent, the ionic association of salt anions and the water content, have a significant influence on Li_2O_2 deposition and battery performance[30] (Figure 2.4). Johnson et al.[10] proposed a unified mechanism that describes the partition among these parameters by the solubilization of LiO_2 via:

$$LiO_2^* \leftrightarrow Li^+_{(sol)} + O^-_{2(sol)} + \text{ion pairs} + \text{higher aggregates} \qquad (2.5)$$

The DNs of the commonly employed electrolyte solvents cover a wide range, such as nitriles and sulfones (DN = 14-16), glymes (DN = 20-24), amides (DN ~ 26), sulfoxide (DN ~30), etc.[31] For solvent with high DN, the Gibbs free energy of solvated LiO_2 is lower than LiO_2^*, which shifts the equilibrium in equation (2.5) to the right and promotes the solution growth pathway. While for low-DN solvent, the equilibrium moves to the left and promotes the surface growth pathway.

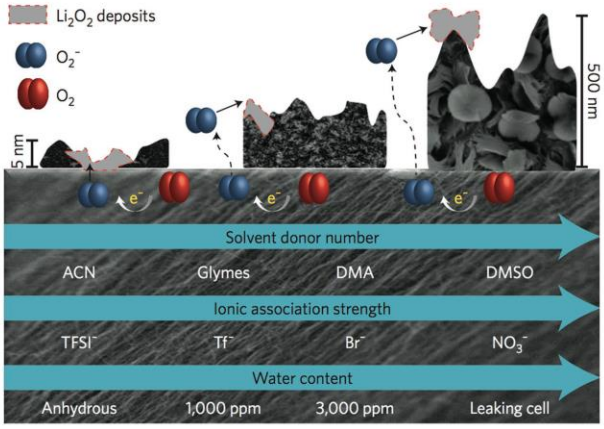

Figure 2.4. Surface and solution growth mechanisms of Li_2O_2 in different electrolyte solutions. Figure is reproduced with permission from ref 30.

The anion in the electrolyte can also control the solvation behavior of the LiO_2 intermediates and enhance discharge capacity. Burke et al.[32] demonstrated that batteries with a high concentration of NO_3^- in DME electrolyte can provide a four-fold larger capacity than that with $TFSI^-$. The NO_3^- anions have a higher DN than DME, so the electrochemically formed O_2^- anions are more stable in the electrolyte solvent. The solubility of the LiO_2 intermediates is also greatly increased, so a larger capacity is achieved. The combination of a low-DN solvent and high-DN anion can enhance the discharge capacity of non-aqueous Li-O_2 batteries, shedding lights on the rational selection of solvent and salt combinations.

Water is a common contamination in the electrolyte and can significantly alter the growth of Li_2O_2[33,34]. Schwenke et al.[35] first reported that water in the electrolyte can boost the discharge capacity of the battery. Later, Aetukuri et al.[9] proposed a mechanism that the water additive can solvate LiO_2^* to form solvated Li^+ and O_2^-, promoting the solution growth pathway. The size of the formed Li_2O_2 toroids is also highly dependent on the water concentration, e.g., Li_2O_2 toroids as large as 1 μm can be observed in the electrolyte with 4000 ppm water content.

However, the addition of water also results in high charge potential and poor cyclability[36], as well as corrosion at the anode[37].

2.1.4. Alternative Discharge Products and Mechanisms

Li_2O_2 is generally considered to be the desired discharge product in non-aqueous Li-O_2 battery because it is more stable than LiO_2 and can be decomposed under a relatively low potential[38]. However, its insulating and insoluble nature still proves to be problematic. Efforts have been made to seek alternative discharge products and mechanisms. Li et al.[34] employed a Ru and MnO_2 nanoparticles-decorated Super P cathode and achieved the reversible cycling of LiOH by applying a trace amount of water in the electrolyte. The mechanism of the reactions is summarized in Figure 2.5a. During discharge, Li_2O_2 is first generated via a common solution growth pathway. Meanwhile, Li_2O_2 reacts with water facilely to form LiOH. Although the conversion of Li_2O_2 to LiOH and H_2O_2 (step i) is an equilibrium[35], MnO_2 catalyst can readily decompose H_2O_2 (step ii) and move the equilibrium to the right side. LiOH can be generated as long as water is present in the electrolyte. During charge, LiOH is facilely decomposed in the presence of Ru (step iii). Impressively, the battery can operate at a low charge potential of ~3.2 V throughout most of the charging process and remain stable for over 200 cycles (at 500 mA g^{-1} and 1000 mAh g^{-1}).

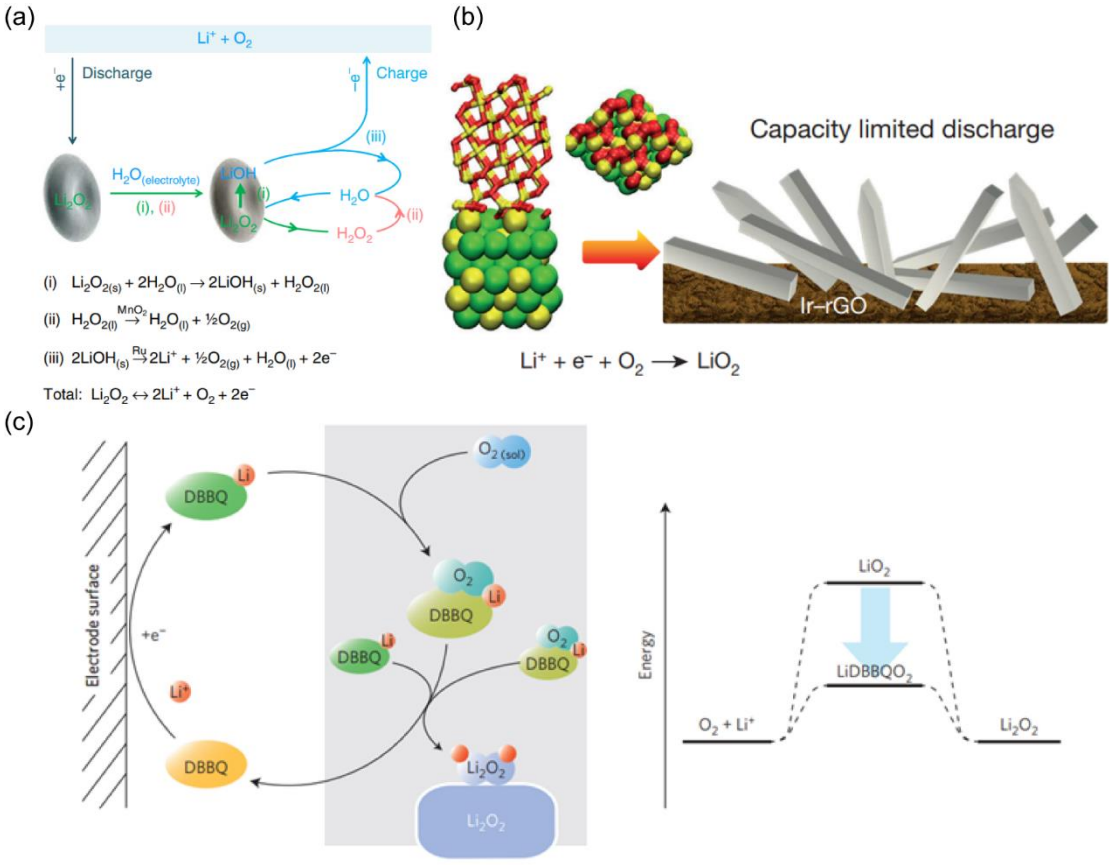

Figure 2.5. (a) Proposed reaction mechanism of LiOH cycling on Ru/MnO_2/SP cathode; (b) scheme showing lattice match between LiO_2 and Ir_3Li that is responsible for the LiO_2 discharge product found on the Ir-rGO cathode; (c) schemes of reactions on discharge (left) and the effect of DBBQ on the potential determining step (right). Figures are reproduced with permission from (a) ref 34, (b) ref 39, (c) ref 40.

Lu et al.[39] reported that LiO_2 can be stabilized on an Ir-decorated reduced graphene oxide cathode. Ir_3Li intermetallic compound is observed on cathode surfaces. Density functional theory calculations on the interface between LiO_2 and Ir_3Li reveal good lattice matches between the two crystal faces (Figure 2.5b). Ir_3Li can then act as a template for the nucleation and growth of the crystalline LiO_2, which cannot undergo further disproportionation to form Li_2O_2. Kinetic studies reveal that the prevention of disproportionation is due to the high energy barrier (0.9 eV) for O_2 desorption on crystalline LiO_2. Crystalline LiO_2 displays better conductivity than bulk Li_2O_2, and the cathode can achieve a low charge potential of ~ 3.2 V.

This work has provided insights into template-induced control of the discharge product.

The LiO_2 intermediates are reactive towards common electrolyte solvent and are often ascribed as the reason for electrolyte instability[41,42]. Efforts have been made to persuade the discharge mechanism to a different pathway. Gao et al.[40] described a strategy to use 2,5-di-tert-butyl-1,4-benzoquinone (DBBQ) as an additive in the electrolyte solution to avoid the generation of LiO_2 intermediates. During discharge, DBBQ is first reduced to $DBBQ^-$ on cathode surfaces, where it combines with Li^+ and O_2 to form a $LiDBBQO_2$ complex. Sequentially, $LiDBBQO_2$ undergoes disproportionation to generate Li_2O_2, and DBBQ is reformed. The free energy of the $LiDBBQO_2$ intermediates is lower than that of the LiO_2 intermediates, which results in higher discharge potential of the battery (Figure 2.5c). This new mechanism enables the formation of Li_2O_2 toroids via the solution growth pathway without the need for a high-DN solvent to solvate LiO_2. As a result, stable electrolyte with low DN can be used without compromising discharge capacity performance. Because the electrochemistry occurs only in the electrolyte, future cathode design can move away from the problematic heterogeneous catalysis at the solid - gas - liquid interface.

2.2. Li_2O_2 Decomposition during OER

During the charging process, Li_2O_2 is oxidized and decomposed, which evolves oxygen during OER. The OER process is well-known for being troubled by numerous side reactions. Although the Li_2O_2 oxidation has been complicated by these reactions, much progress has been made in understanding the mechanism of Li_2O_2 oxidation in recent years, which will be detailed in the following section. The effect of OER electrocatalyst and parasitic reactions and their implications on cathode design will also be discussed in detail.

2.2.1. Mechanism of Li_2O_2 Decomposition

The oxidation and decomposition of Li_2O_2 during OER is significantly complicated by the ambiguity regarding the effects of Li_2O_2 morphology and the parasitic reactions. The principle electrochemistry for the oxidation of Li_2O_2 is usually considered to be a one-step reaction[43]:

$$Li_2O_2 \rightarrow 2Li^+ + O_2 + 2e^- \quad (6)$$

Theoretical studies have provided evidence of minimal charge overpotentials (< 0.2 V) for O_2 evolution during Li_2O_2 decomposition[44], yet this low charge overpotential can only be observed during the early stages of charge. The typical charge potential profile for a non-aqueous Li-O_2 battery is characterized by a charging slightly above 3.0 V followed by an ever-increasing potential as the charging progresses. The increasing potential is partially related to the increasing impedance imposed by the slow electron transport in bulk Li_2O_2[45], but mostly to the carbonate parasitic products at the Li_2O_2/electrolyte interface[46,47].

Various mechanisms have been proposed for the decomposition of Li_2O_2 toroids. Early studies assigned the starting low potential region and later high potential region to the respective oxidations of LiO_2 and Li_2O_2. However, LiO_2 is unstable and readily undergoes

disproportionation to form Li_2O_2[48]. It is unlikely LiO_2 is stable enough to be a discharge product under normal circumstance. Later, Kang et al.[49] described an alternative mechanism based on the topotactic delithiation of Li_2O_2 to form Li-deficient $Li_{2-x}O_2$. The topotactic delithiation mechanism is calculated to be possible at a small overpotential of ~ 0.3-0.4 V, which is more favorable kinetically than direct Li_2O_2 decomposition. Ganapathy et al.[50] used *operando* X-ray diffraction to reveal the presence of Li-deficient $Li_{2-x}O_2$ during the charging process. The decomposition mechanism of the electrochemically generated Li_2O_2 (E-Li_2O_2) is schematically illustrated in Figure 2.6a and b. E-Li_2O_2 displays a flat platelet morphology embedded in an amorphous lithium-bearing component. The amorphous region is decomposed first at low potentials. At a higher potential, crystalline Li_2O_2 can be decomposed via a Li deficient solid-solution reaction. The thinnest and smallest platelet crystallites are preferentially oxidized, resulting in a "plate-by-plate" oxidization process. Recently, Hong et al.[51] described the decomposition process of Li_2O_2 layers: the thinner part of the layer decomposes first at < 3.7V resulting in the appearance of pits, while thicker part of the layer decomposes at > 4.0 V in the lateral direction, revealing the sluggish charge transport towards layer surface even at a thickness of merely ~3 nm (Figure 2.6e). This study highlights the challenges to efficiently decompose Li_2O_2 because of its poor charge transport properties.

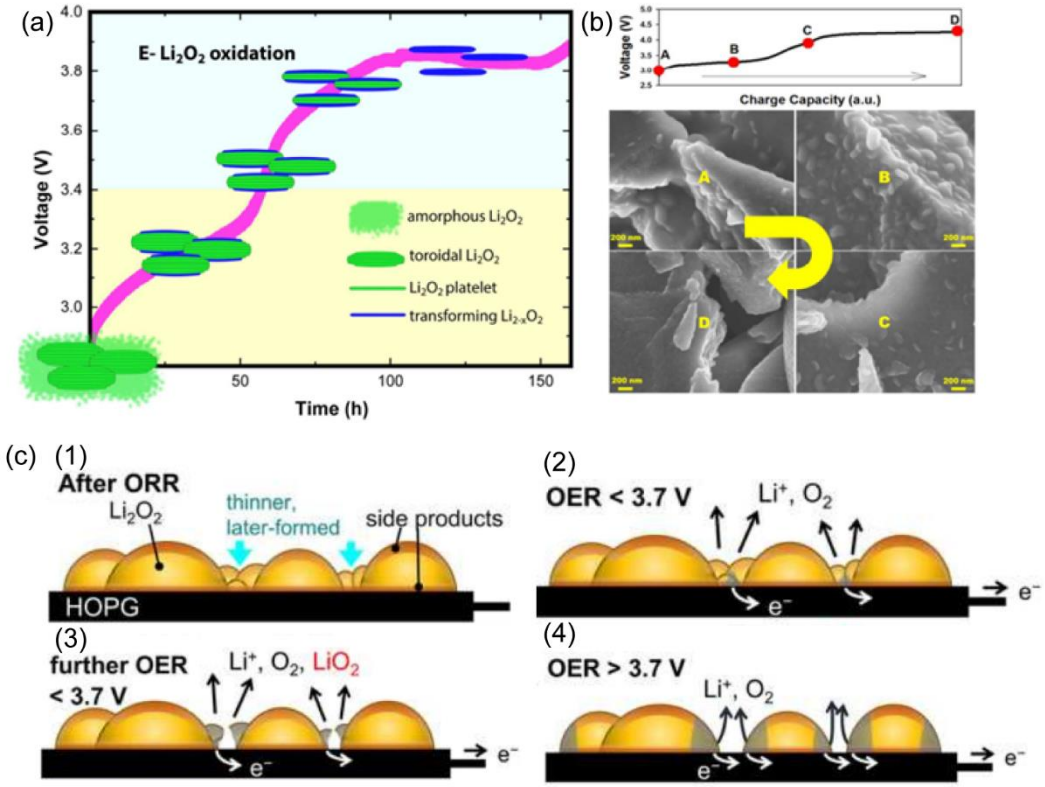

Figure 2.6. (a) Scheme of the E-Li_2O_2 decomposition process; (b) the visualization of E-Li_2O_2 decomposition; (c) scheme of the Li_2O_2 layer decomposition process, the gray parts indicate the active Li_2O_2 area for OER. Figures are reproduced with permission from (a, b) ref 50, (c) ref 51.

One intriguing prospect to overcome the sluggish charge transport properties of Li_2O_2 is to promote the amorphous region in Li_2O_2. Theoretical and experimental studies reveal that the electronic conductivity of amorphous Li_2O_2 is several magnitudes higher than its crystalline counterpart; the enhanced Li^+ mobility and increased O_2^- concentration can improve the ionic and electronic conductivity of amorphous Li_2O_2[52,53]. The defects and grain boundaries in Li_2O_2 have also been attributed to the enhanced OER performance[54]. Li_2O_2 formed via surface growth pathway can be tweaked with a significant portion of amorphous Li_2O_2[19,20]. The rational designs of cathode materials that promote the formation of amorphous Li_2O_2 can enhance the charge transport properties of Li_2O_2 and promote the OER performance.

2.2.2. Effect of Electrocatalyst on Li_2O_2 Decomposition

In order to reduce the high overpotential during charge, researches in the past decade have been focused on the identification of an effective electrocatalyst, especially for the OER process. Precious metals and transition metal oxides, usually in the form of nanoparticles that can be loaded on a porous carbon cathode, have been proposed[55,56]. The underlying mechanism for the electrocatalysis of Li_2O_2 decomposition is not well-understood. Nevertheless, much effort has been made to provide guidance on the rational design of electrocatalysts and cathode materials.

Theoretical calculation revealed the oxygen evolution step has a high energy barrier because oxygen is strongly bonded on most Li_2O_2 facets[57]. Song et al.[58] argued that the reduction of this energy barrier is the primary role of electrocatalysts. Gao et al.[59] employed density functional theory to simulate the OER pathways on Co_3O_4 (111) and (001) facets. They found that $Li^+ \rightarrow Li^+ \rightarrow O_2$ pathway is favored over $Li^+ \rightarrow O_2 \rightarrow Li^+$ pathway on both facets. The energy barrier for oxygen desorption on Co_3O_4 (111) facet is reduced to 1.27 eV from 1.92 eV on Co_3O_4 (001) facet, which can lead to reduced charge overpotential on Co_3O_4 (111), as confirmed by the experimental results (Figures 2.7a and b). It is a promising prospect to design electrocatalyst with a tailored surface atomic arrangement to boost the OER performance of the battery[60,61].

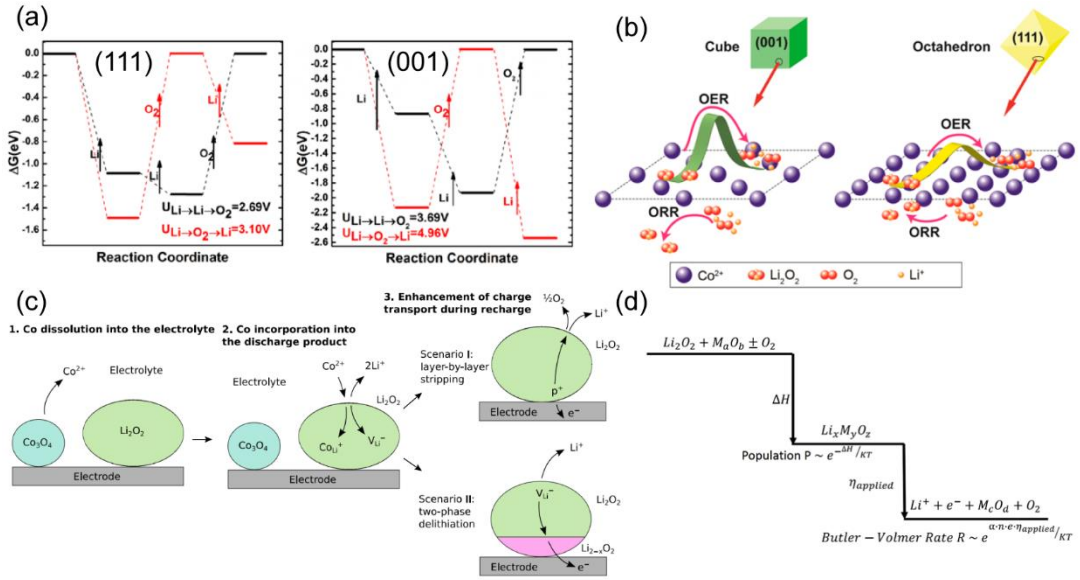

Figure 2.7. (a) Energy profiles of OER paths on Co_3O_4 (111) and (001) facets; (b) scheme of the facet-dependent electrocatalytic mechanism of ORR and OER on Co_3O_4 (001) and Co_3O_4 (111); (c) proposed mechanism for the promotion of OER in Co_3O_4-containing electrodes; (d) scheme of proposed mechanism of chemical conversion of Li_2O_2 and catalyst to $Li_xM_yO_z$ followed by delithiation. Figures are reproduced with permission from (a, b) ref 59, (c) ref 62, (d) ref 63.

Radin et al.[62] proposed that electrocatalyst could enhance the charge transport property of Li_2O_2 by *in-situ* doping. For example, a small amount of Co in Co_3O_4 catalyst can be dissolved in the electrolyte and be incorporated in Li_2O_2, which enhances the charge transport properties of Li_2O_2 and reduces charge overpotential of the battery (Figure 2.7c). Yao et al.[63] studied the kinetics of Li_2O_2 oxidation on Co, Mo, Cr, Ru and their oxides using electrodes pre-loaded with crystalline Li_2O_2. The enhancement of Li_2O_2 oxidation is facilitated by the chemical conversion of Li_2O_2 to a lithium metal oxide via $Li_2O_2 + M_aO_b \pm O_2 \rightarrow Li_xM_yO_z$, where M_aO_b is the surface composition of the metal or metal oxide. During charge, $Li_xM_yO_z$ is decomposed via electrochemical delithiation which generally shows better kinetics compared to the direct decomposition of Li_2O_2 (Figure 2.7d). It should be

noted that the delithiation of $Li_xM_yO_z$ cannot necessarily regenerate original metal or metal oxide, as such, the metals and their oxides should not be considered as catalysts[64].

The true effectiveness of solid catalysts relies heavily on the close contact of the catalysts and discharge products. In the case of the solution grown Li_2O_2 toroids, because neither Li_2O_2 nor the electrocatalysts have mobility, the electrocatalysts fixated on cathode surfaces do not have access to the large Li_2O_2 toroids located away from those electrocatalysts. Therefore, no true electrochemical activity may occur except for a small portion of the charging process during the final dissolution phase[65]. Nevertheless, the employment of these electrocatalysts has universally shown reduced charge overpotential, even for solution grown Li_2O_2. It is possible they can benefit the charging process in some other way as Radin et al.[62] and Yao et al.[63] proposed, but not as true electrocatalysts. However, the matter is inconclusive.

On the other hand, the surface growth pathway can circumvent some limitations of the solid electrocatalyst, because the surface grown Li_2O_2 layers are in close contact with cathode surfaces and electrocatalysts, which is often attributed to the reduced charge overpotential compared to the solution grown Li_2O_2[1,11]. Therefore, solid electrocatalysts might benefit the decomposition of Li_2O_2 from the surface growth pathway more than that from the solution growth pathway, and the cathode materials should be designed accordingly.

To address the inefficient decomposition of large Li_2O_2 toroids with solid electrocatalysts, soluble oxidation mediators are proposed. Chen et al.[66] first proposed tetrathiafulvalene (TTF) as an electron-hole transfer agent that enables efficient oxidization of Li_2O_2 at a low charge potential of ~3.5 V. Later, various oxidation mediators, including organic meditators (e.g., tris[4-(diethylamino)phenyl]amine [67], 2,2,6,6-tetramethylpiperidinyloxyl [68]), organo-metallic meditators (e.g., iron-phthalocyanine[69], cobalt bis(terpyridine)[70]), halide meditators

(e.g., LiI[71], LiBr[72]), etc., are proposed. These mediators show a high diffusion coefficient and charge transfer kinetics, allowing the oxidation of Li_2O_2 at near zero charge overpotential. It should be noted that these mediators can also promote side reactions with electrolyte and Li anode[73]. The commonly used organic and organometallic mediators also suffer from intrinsic instability in the potential window of non-aqueous Li-O_2 batteries and are susceptible to attack from peroxide and superoxide[74]. The search for a stable redox mediator remains challenging.

2.2.3. Parasitic Reactions at Cathode

The electrochemistry of non-aqueous Li-O_2 batteries at the cathode is susceptible to parasitic reactions induced by reactive oxygen species[16], primarily O^{2-} and O_2^{2-}. Carbon materials have been widely used as cathode materials due to their high conductivity, high surface areas, and low weight. During discharge, the nucleophilic and reactive O^{2-} and O_2^{2-} can attack carbon materials and form carbonate (Li_2CO_3) and carboxylates (HCO_2Li, CH_3CO_2Li), which can also promote the decomposition of the electrolyte[75]. However, carbon corrosion during discharge only constitutes a small portion of the total corrosion, considering charge has much more side reactions than discharge[16]. The apparent high potential (> 4.0 V) needed for the charge can lead to the direct oxidization of carbon in an oxygen-rich environment. Further study[75] reveals that in the presence of Li_2O_2, carbon is only stable below 3.5 V. Beyond this potential, carbon decomposes significantly, leading to the formation of Li_2CO_3 on cathode surfaces. The Li_2CO_3 parasitic products increase charge overpotential and passivate the electrocatalytic active surfaces of carbon[64]. McCloskey et al.[37,47] described the charge profile for Li_2O_2 oxidation in the presence of interfacial Li_2CO_3. After discharge, a

monolayer of Li_2CO_3 is formed on the interface of Li_2O_2 and carbon as the result of carbon decomposition. Upon charging, Li_2CO_3 cannot be oxidized at a low potential and start to concentrate on the surface of Li_2O_2 layer. As the Li_2O_2 layer declines, the charge potential must continuously rise to maintain the galvanostatic charge rate until a high potential is reached, where Li_2CO_3 can be oxidized to evolve CO_2 (Figure 2.8). Their kinetic model also suggests that even ~1 monolayer of carbonate at the Li_2O_2-carbon interface can cause a ~10-100-fold decrease in the exchange current density due to the interfacial resistance.

Several approaches have been proposed to alleviate the decomposition. The passivation and protection of carbon is an effective approach to minimize carbon decomposition, and it can be achieved with atomic layer deposition. For example, Xie et al.[76] reported the passivation of a three-dimensional ordered mesoporous carbon cathode through the atomic layer deposition of FeO_x on carbon surfaces. Differential electrochemical mass spectrometry results confirm that after passivation, carbon decomposition is significantly suppressed. FeO_x can also promote OER activity and improve battery performance. Bae et al.[77] recently demonstrated that ZnO coating on carbon cathode could suppress electrolyte decomposition. This approach allows full utilization of the light-weight and high surface area porous carbon. Alternatively, carbon-free cathodes, such as $NiCo_2O_4$ nanosheet array on Ni foam[78], Ru decorated Ni foam[79], nanoporous Au[80], etc., have been proposed to avoid the use of carbon altogether. However, these cathodes are heavy and deliver less specific capacity.

An intriguing option to minimize the accumulation of Li_2CO_3 is to employ an electrocatalyst to reduce the potential at which Li_2CO_3 can be oxidized. Few such electrocatalysts have been identified. Hong et al.[81] first provided evidence that nanoporous NiO hexagonal plates can reduce the potential of the complete oxidation of carbonates and carboxylates at ~4.0 V.

Recently, Song et al.[82] also discovered that a carbon-free Ir/B_4C cathode can decompose Li_2CO_3 below 4.37 V with an efficiency close to 100 %. However, their oxidation potentials are still significantly higher than the 3.5 V threshold for stable carbon.

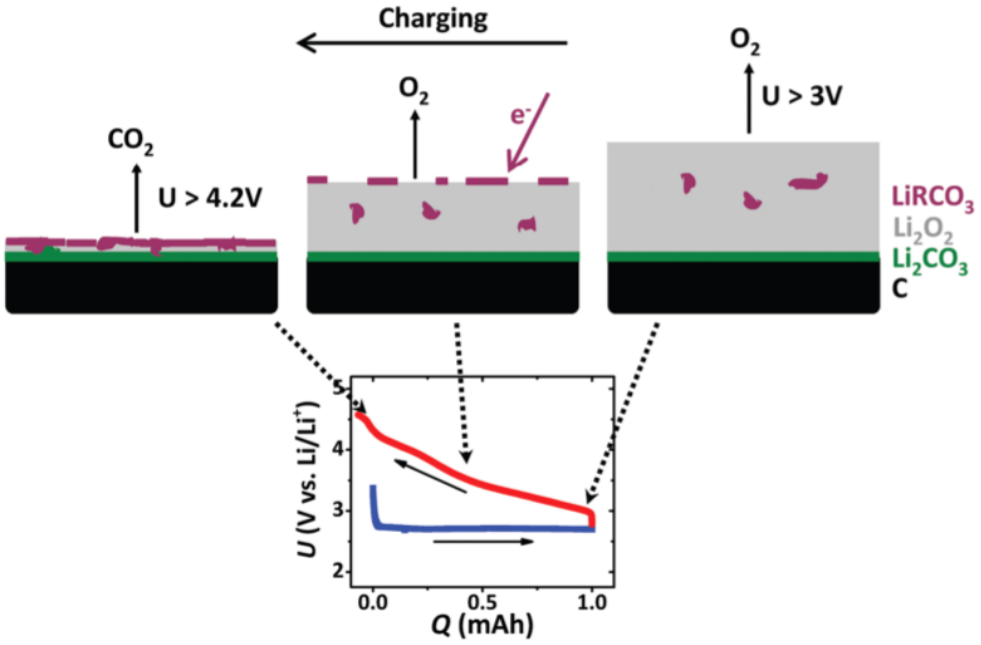

Figure 2.8. Scheme of the C cathode (black) and a picture of what may happen to the deposit during charging to cause the rising charging potential. ~1 monolayer of Li_2CO_3 forms at the C interface, some dispersed carboxylate or other solid decomposition products form as a result of electrolyte decomposition in the Li_2O_2 deposit, and some more deposit forms at the electrolyte interface during charging. The e^- represents some unspecified electrochemical reaction producing carbonate at the interface during charging. The proportions are not to scale. The inset shows the potential typically observed for galvanostatic discharge-charge. The dashed arrows indicate qualitatively the charging potential appropriate for the three panels measured by quantitative differential electrochemical mass spectrometry. Figures are reproduced from ref 37.

Another major source of parasitic reactions is the decomposition of electrolyte solvent, especially high-DN solvent because they are more susceptible to the attack of reactive oxygen species[83]. Low-DN electrolyte solvents are more stable, but they also favor the surface growth pathway, which can lead to low discharge capacity. In addition, cautions should be taken when selecting cathode materials to avoid parasitic reactions introduced by these materials. A well-known example is Pt, which displays a low apparent charge potential of 3.6 V in the presence of DME electrolyte[84]. However, differential electrochemical mass spectrometry results indicate that the true reaction is the decomposition of the electrolyte rather than Li_2O_2[85]. Therefore, the ideal cathodic electrocatalysts should not promote the decomposition of the electrolyte, and cathode designs should not be considered in isolation and without compatible electrolyte[30,75].

2.3. Recent Advances in Cathode Material Development

The ideal cathode materials based primarily on the electrochemical formation and decomposition of Li_2O_2 should provide proper pore structures for discharge product accommodation, sufficient electron and mass transport properties, high activity towards ORR and OER together with excellent stability against various parasitic reactions. In this section, the most popular and promising cathode materials will be detailed. Selected work with great implications for further designs will be highlighted and discussed.

2.3.1. Carbon Materials

Carbon materials, such as CNT, graphene, active carbon, etc., have been widely used as cathode materials for their excellent physiochemical properties, including high surface areas, high conductivity, low toxicity and chemically modifiable surfaces[86,87]. Compared to

cathodes using metal and metal oxides, the metal-free carbon-based cathodes for non-aqueous Li-air batteries are inexpensive and are available form abundant environmental-friendly sources, such as recycled waste and biomass (e.g., orange feel and bamboo)[88,89].

It is well-known that metal-free carbon cathodes suffer from low OER activity and high charge overpotential. Surface modifications of these carbon cathodes, most notably heteroatom-doping, have been proposed to tackle this issue. N-doping has been well-known for enhancing battery performance: the pyridinic-N and graphitic-N sites on carbon can change the electronic properties of the carbon and act as active sites for the oxidization and decomposition of Li_2O_2[90,91]. Other elements, such as P and S[92,93], have also been successfully incorporated into carbon for metal-free air cathodes. Recently, Wu et al.[94] synthesized a novel B-doped reduced graphene oxide as a cathode material, which achieves a high discharge capacity (~ 18000 mAh g^{-1} at 100 mA g^{-1}). The vacant orbital of B can extract electrons from the graphite carbon π system via the conjugation effect and greatly activate the electrons, leading to improved performance (Figure 2.9a). Density functional theory results suggest the strong binding strength with the discharge product intermediate (represented by a Li_5O_6 cluster) is attributed to the effective activation of Li-O bonds that can promote Li_2O_2 decomposition (Figure 2.9b). The surface modification of carbon is a highly versatile technique that can be utilized to tailor cathode surfaces for non-aqueous Li-O_2 batteries. As mentioned earlier, the surface modifications of MWNT can even promote Li_2O_2 formation via the surface growth pathway[26].

In addition, carbon materials enable the design and facile synthesis of porous cathodes with well-defined size and shape. Macroporous CNT and reduced graphene oxide foams can be synthesized with the aid of sacrificial templates, which are sequentially removed to generate

desired pore structure[97,98]. Xu et al.[95] designed a 3D hierarchically porous carbon membrane (HPCM) using ordered ZnO nanorods (15 μm in length and 300-420 nm in diameter) array template. The through macropores generated from ZnO provide abundant cross-section area for both ORR and OER, which promotes the rate performance and capacity retention capability of the battery (Figure 2.9c). Recently, the importance of the pore shape, interconnectivity and tortuosity of the cathodes has been realized considering the toroid morphology of Li_2O_2[99]. Oh et al.[96] used rod-like *E. Coli* as a template to synthesize MWCNT foam (E-MWCNT) with cylindrical macropores (Figure 2.9d). Li_2O_2 is only deposited on the surfaces of a pore-less MWCNT cathode, while on E-MWCNT, Li_2O_2 can grow deeper and throughout the whole foam, leading to higher Li_2O_2 production and 2-3 times larger discharge capacity (Figure 2.9e). The pores in these macroporous carbon cathodes can serve as adequate Li_2O_2 accommodation sites for high-capacity batteries.

It should be noted despite the best efforts, carbon-only cathodes might not be sufficiently active or stable for non-aqueous Li-O_2 batteries. A common compromise is to use carbon as a support for metal and metal oxide electrocatalysts so the rich pore structure, high surface area and high conductivity of the porous carbon materials can still be taken advantage of.

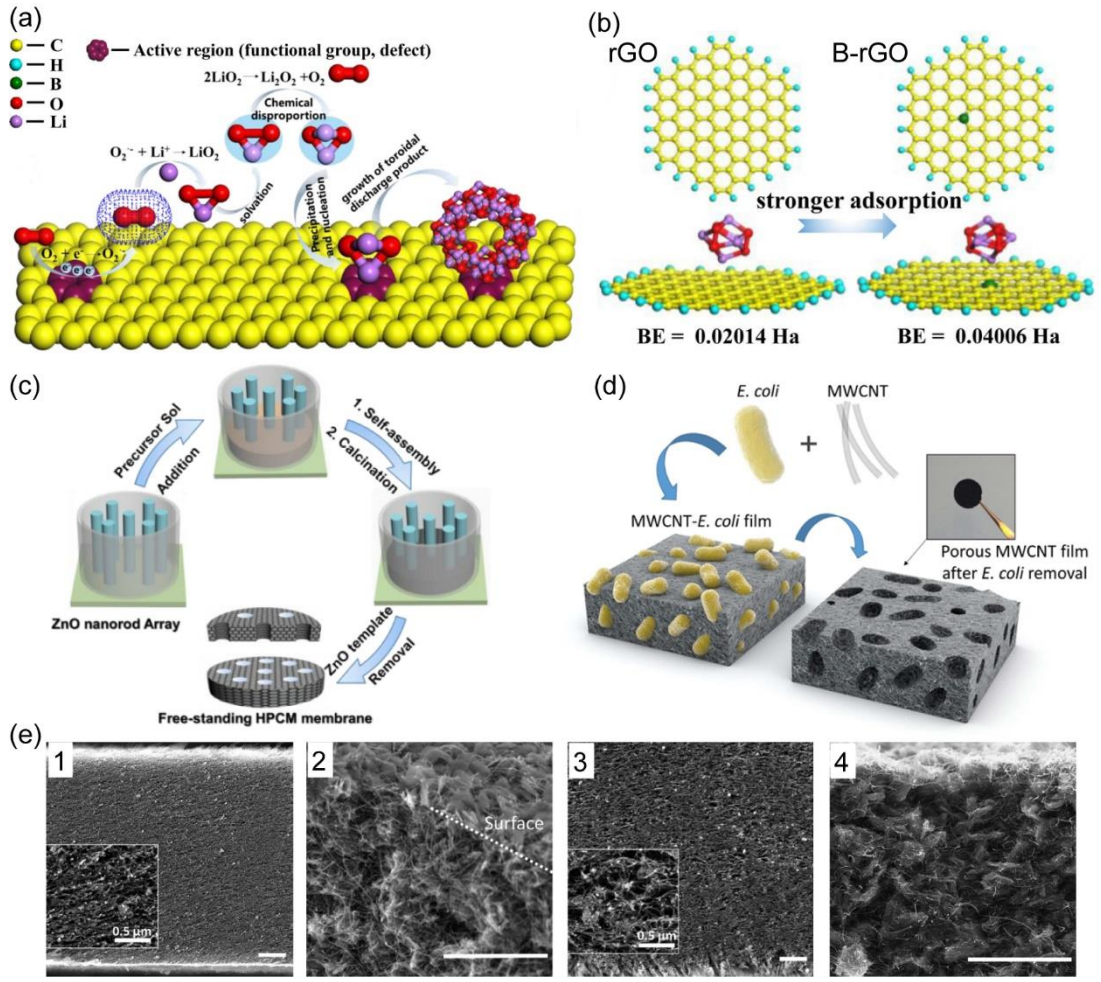

Figure 2.9. (a) Scheme of formation of the toroidal Li_2O_2 on the active region of the graphene layer; (b) optimized geometries of the Li_5O_6 intermediates on rGO and B-rGO and their binding energy values; (c) fabrication of freestanding hierarchically porous carbon membranes by inverse transformation from ZnO nanorod array; (d) scheme of the porous E-MWCNT film fabrication; (e) SEM images of (1) pristine and (2) discharged MWCNT cathode; SEM images of (3) pristine and (4) discharged E-MWCNT cathode (scale bars indicate 2 μm). Figures are reproduced with permission from (a, b) ref 94, (c) ref 95, (d, e) ref 96.

2.3.2. Precious Metals and their Oxides

Precious metal and their oxides are well-known for their superior electrocatalytic activity. Unsurprisingly, the employment of Pt[100], Ag[101], Ru[102], RuO_2[103], etc., can significantly reduce charge overpotentials. Despite the superior performance, the scarce and expensive nature of

these precious metals will hinder their feasibility in potential commercial usages. In response, a common strategy it to alloy precious metals with much cheaper transition metals, and bi-metallic systems such as Pt_3Ni[104] and PdFe[105] are recently used as cathode materials for non-aqueous Li-O_2 batteries. Alternatively, the micro- and nanostructures of the cathodes can be optimized, so the loadings of the precious metals are minimized. For example, ultra-fine RuO_2 nanoparticles were uniformly deposited on a freestanding Mn_3O_4/CNT film via atomic layer deposition and the loading of RuO_2 is 2.84 wt%. The Mn_3O_4/CNT film modulates the electronic structure of RuO_2 to enhance the LiO_2 adsorption ability and promote the surface growth pathway. Consequently, Li_2O_2 nanosheet that can be facilely decomposed is formed, resulting in long cycle stability of 251 cycles[106]. Huang et al.[107] synthesized an ultra-thin (2.6 nm) and highly conductive (35 S cm^{-1}) RuO_2 nanosheet using GO as a sacrificial template, which is sequentially hybridized with CNT. RuO_2 shows a strong affinity with Li_2O_2 with a binding energy of -3.74 eV (Figure 2.10a), which leads to the formation of a dumbbell-shaped RuO_2/Li_2O_2 heterostructure that can be facilely decomposed (Figure 2.10b).

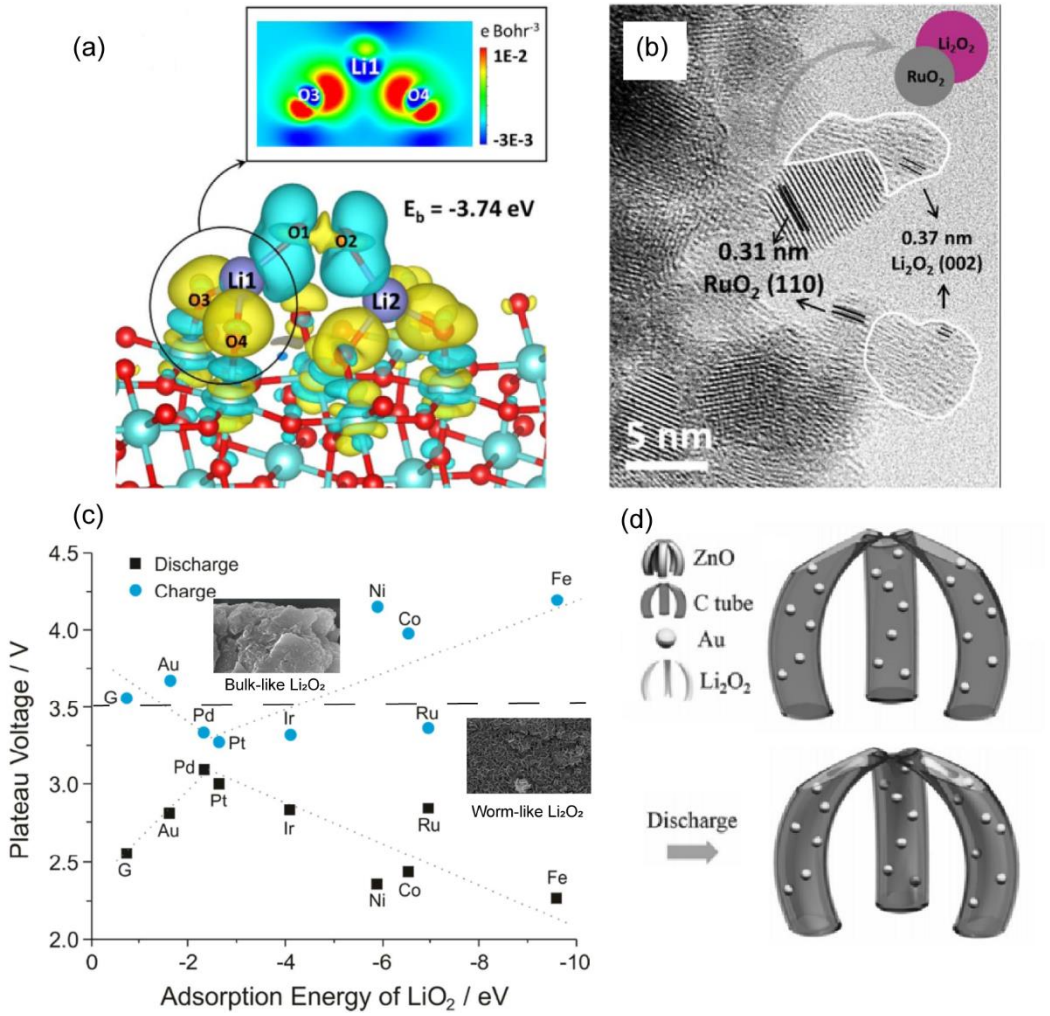

Figure 2.10. (a) Charge density difference when Li_2O_2 nucleates at the RuO_2 (110) slab with the cross-section data of the plane of Li1, O3 and O4 (insert); (b) TEM image of RuO_2/CNT electrodes after discharge and scheme of RuO_2/Li_2O_2 dumbbell structure (insert); (c) volcano-type relationship among discharge/charge plateau voltage, the adsorption energy of LiO_2 on the planar model electrodes and the morphology of formed Li_2O_2; (d) scheme of Li_2O_2 growth inside Au@CST cathode. Figures are reproduced with permission from (a, b) ref 107, (c) ref 108, (d) ref 28.

The ability to modulate the morphology of Li_2O_2 discharge product is not exclusive to RuO_2. Recently, Yang et al.[108] conducted a systematical study on precious metal together with 3d transition metals and proposed a comprehensible "volcano plot" that correlates the potential profiles to the adsorption energies of LiO_2. The metals near the top of the "volcano" promote the surface growth pathway and produce worm-like Li_2O_2 (Figure 2.10c). This paves the path for novel cathode designs tailored for the surface growth pathway. For example, Tu et al.[28] designed a carbon tube arrays cathode with Au nanoparticles grown on the inner tubular walls of the carbon support (Au@CST). Crucially, Au nanoparticles modulate Li_2O_2 layer formation via the surface growth pathway on the inner tubular walls and leave outer tubular wall intact, so the conductive carbon support is not passivated by Li_2O_2 even when the battery is deeply discharged (Figure 2.10d).

2.3.3. Transition Metal Oxides

Transition metal oxides have attracted enormous attention in the field of electrocatalysis due to their unique electronic configurations of the transition metals, which show multiple oxidation states within a single bulk material[109]. For non-aqueous Li-O_2 batteries, the mixed-valence cations can often act as different active sites and lead to bifunctional characteristics that can modulate both the formation and decomposition of Li_2O_2[109]. In recent years, attempts have been made to tailor the electronic structures of the transition metal oxides to enhance their performance. Introducing oxygen vacancies, for example, is an inexpensive and facile approach to modify the surfaces of transition metal oxides that can modulate Li_2O_2 nucleation and growth[110]. Wang et al.[111] designed a Co_3O_4 nanosheet material with Co^{3+}-rich surface and oxygen vacancy-rich interior. The oxygen vacancies in the interior facilitate

electron and Li^+ transportation. Co^{3+} is more active towards OER than Co^{2+} so the concentrated Co^{3+} on the nanosheet surfaces can further enhance the battery performance in comparison to bulk Co_3O_4 material (Figure 2.11a). Gu et al.[112] demonstrated a novel approach to modify the surface electronic structure of α-MnO_2 nanowire. The anchoring of the highly electronegative selenate (SeO_4^{2-}) cluster on α-MnO_2 enhances the oxygen adsorption of the cathode, which leads to improved ORR/OER activity (Figure 2.11b). Ternary metal oxides, such as spinel oxides[113] (general formula AB_2O_4) and perovskite oxides[114] (general formula ABO_3), display a wide range of compositions and even richer electrocatalytic activities than binary systems. The electronic structures of ternary metal oxides are highly complicated, but they also can be fine-tuned for non-aqueous Li-O_2 batteries via rational design. For example, Cong et al.[115] developed an α-Fe_2O_3-$LaFeO_{3-x}$ cathode for the first time by the segregation of α-Fe_2O_3 in $La_{0.85}FeO_{3-\delta}$. The unique α-Fe_2O_3-$LaFeO_{3-x}$ structure can promote the adsorption of oxygen and enhance battery performance. Another fascinating property of transition metal oxides is their rich nanostructures. Unlike precious metals that are usually in the form of small zero-dimensional nanoparticles, a wide variety of transition metal oxides, namely 0D (e.g., $NiFe_2O_4$ nanoparticles[119]), 1D (e.g., CoO nanorods[120]), 2D (e.g., ultra-thin Co_3O_4 nanosheet[121]) and 3D (e.g., 3D $MnCo_2O_4$ nanowire bundles[122]) nanostructures, have been proposed as cathode materials. More importantly, unique hetero-structure consists of different chemical composition and morphology can be achieved. Lower dimension nanostructures can be used as building blocks to construct advanced three-dimensional hetero-structure tailored for non-aqueous Li-O_2 batteries[123]. For example, Lee et al.[124] proposed a hetero-structured MnO_2 decorated Co_3O_4 nanoplatelet as an efficient cathode material, with MnO_2 mainly prompting ORR and Co_3O_4 promoting OER.

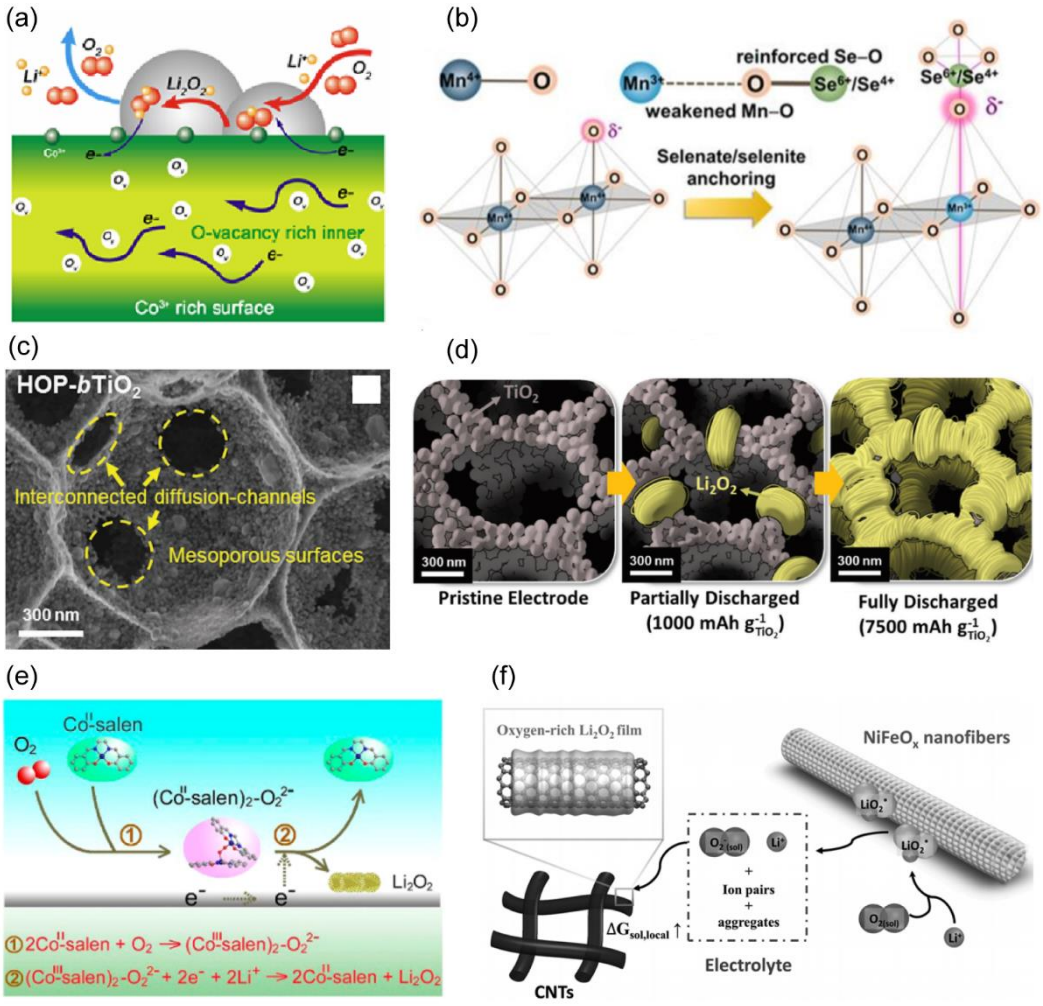

Figure 2.11. (a) Scheme of the synergetic effect of the 2D Co_3O_4 nanosheets, with a high concentration of oxygen vacancies in the interior and high Co^{3+} concentration on the surface; (b) scheme for the beneficial effect of selenate anchoring on the local geometry and oxygen electron charge of α-MnO_2 NW; (c) the SEM image of HOP-bTiO_2; (d) scheme of the growing tendency of Li_2O_2 that is guided by the ordered electrode architecture; (e) scheme and reaction mechanism of Co-salen in the electrolyte during discharge and charge; (f) scheme of the effect of $NiFeO_x$ on formation of Li_2O_2. Figures are reproduced with permission from (a) ref 111, (b) ref 112, (c, d) ref 116, (e) ref 117, (f) ref 118.

The versatile electronic structures and morphologies of the transition metal oxides offer abundant opportunities for novel cathode designs. One prospect is to build a three-dimensional macroporous cathode suited for solution growth pathway. Hierarchical porous cathode consisted of $MnCo_2O_4$ nanoneedle array, for example, can promote oxygen diffusion and electrolyte infiltration, and more importantly, offer large open spaces for the accommodation of large Li_2O_2 toroids[125]. Based on this design, Kang et al.[116] recently synthesized a novel hierarchically ordered porous black TiO_2 (HOP-bTiO_2) cathode (Figure 2.11c). The macroporous (the pore size is ~ 1 μm) TiO_2 framework allows efficient mass transport deep inside the cathode, so all TiO_2 materials are utilized for Li_2O_2 accommodation. Moreover, the highly ordered architecture can guide the regular deposition of Li_2O_2 toroids on the cathode (Figure 2.11d). Unlike most hierarchical porous cathodes in which Li_2O_2 is deposited at the irregular interspaces and cathode surfaces[125], the highly ordered Li_2O_2 production throughout the totality of the cathode enables a high discharge capacity (~ 7500 mAh g^{-1} at 500 mA g^{-1}). HOP-bTiO_2 cathode displays a low overpotential of ~ 1.1 V and cycling stability of 260 cycles (at 500 mA g^{-1} and 1000 mAh g^{-1}). Moreover, LiI is introduced as a redox mediator for HOP-bTiO_2 and further reduces the overpotential of the battery to 0.37 V and improves the cyclability to 340 cycles. To achieve high-performance non-aqueous Li-O_2 batteries, the synergetic effect among the cathode, the electrolyte, and the redox mediator can be taken into consideration. Hu et al.[117] proposed an N,N′-bis(salicylidene)ethylenediaminocobalt(II) (Co-salen) meditator in conjunction with a δ-MnO_2 coated MWCNT (MCNTs@MnO_2) cathode. The MCNTs@MnO_2 cathode can reduce the charge potential and prolong cyclability (98 cycles at 500 mA g^{-1} and 1000 mAh g^{-1}). Co-salen can serve as a mediator to coordinate with O_2 to form $(CO^{III}\text{-salen})_2\text{-}O_2^{2-}$ that

circumvents the highly reactive LiO_2 intermediates. Also, it can act as an oxygen carrier that facilitates O_2 uptake and delivers large discharge capacity (13050 mAh g^{-1} at 500 mA g^{-1}) even in synthetic air where the oxygen partial pressure is much lower than pure oxygen (Figure 2.11e). The Co-salen meditator and MCNTs@MnO_2 cathode work in synergy for the battery, which is stable for over 300 cycles (at 500 mA g^{-1} and 1000 mAh g^{-1}).

Lastly, through rational design, transition metal oxide cathodes can modulate the formation pathway of Li_2O_2. Huang et al.[118] demonstrated that $NiFeO_x$ can promote the formation of Li_2O_2 layer with small crystallites, rich Li vacancies and large contact area with the cathode and electrolyte. The defects on $NiFeO_x$ surfaces can enhance O_2 adsorption, which promotes the surface growth pathway (Figure 2.11f). Crucially, the smaller crystallites and Li vacancies allowed the Li_2O_2 film via surface growth pathway to grow beyond the 5-10 nm limits and to a thickness of 19 nm, achieving a large discharge capacity of ~17000 mAh g^{-1} (at 500 mAh g^{-1}).

2.3.4. Metal Sulfides, Carbides and Nitrides

In order to overcome the general poor conductivity of the transition metal oxides, non-oxides such as sulfides, carbides and nitrides have also been explored for non-aqueous Li-O_2 batteries. Transition metal sulfides can be derived from metal oxides via a sulfidation process while keeping the rich nanostructures of the metal oxide precursors. Owing to their unique electronic and chemical properties[126], transition metal sulfides have attracted attention as potential electrocatalysts. During the past few years, MoS_2 has emerged as a promising cathode material for non-aqueous Li-O_2 batteries. The high surface area and two-dimensional MoS_2 nanosheets can serve as building blocks to construct highly porous three-

dimensional structures with facile electron and mass transport properties[127,128]. Zhang et al.[129] constructed a novel three-dimensional metastable MoSSe solid solution (3D M-MoSSe) by introducing lattice distortion in MoS_2. The modulation of the atomic structure in 3D M-MoSSe can significantly improve electrochemical activity and facilitate ion transport, which is confirmed by *in-situ* transmission electron microscopy. When used as a freestanding cathode, the ultra-thin MoSSe nanosheet with high surface area can offer abundant active sites for ORR and OER, and the 3D M-MoSSe cathode can maintain a stable structure even under high potential (Figure 2.12a).

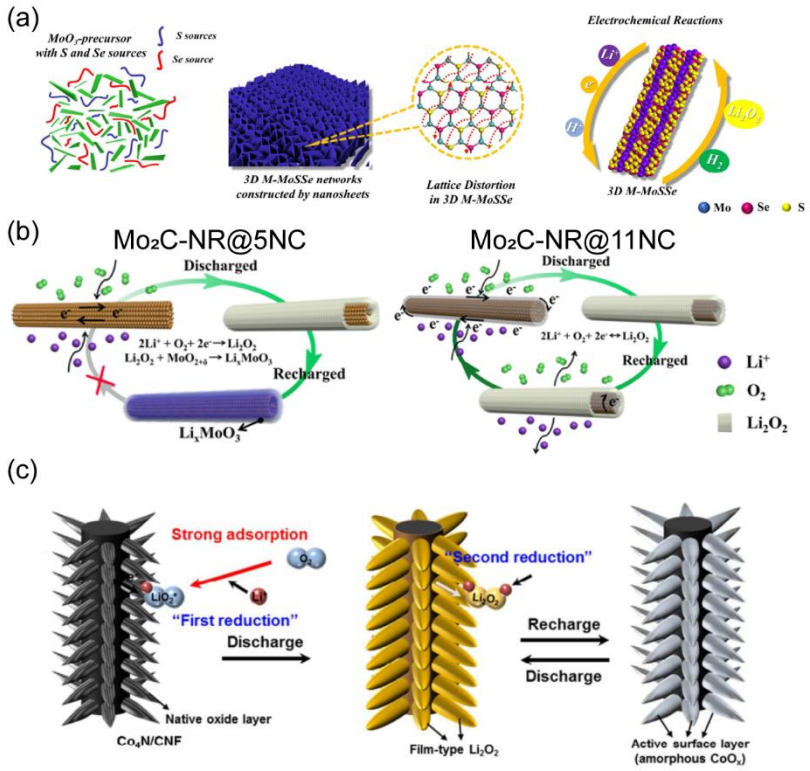

Figure 2.12. (a) Schemes depicting the synthesis procedure of 3D M-MoSSe with distorted lattice structure; (b) scheme of the electrochemical mechanisms for the cells with Mo_2C-NR without carbon protection and Mo_2C-NR@11NC with carbon protection; (c) proposed reaction mechanism of Li-O_2 cells with Co_4N/CNF electrode. Figures are reproduced with permission from (a) ref 129, (b) ref 130, (c) ref 131.

Transition metal carbides are another group of promising electrocatalyst. The broadening of the d-band and the redistribution of DOS via orbital hybridization in transition metal carbides can lead to high catalytic performance[132]. In addition, covalent, ionic and metallic bonds can co-exist in transition metal carbides, which results in good ionic and electronic conductivity[132]. Moreover, they have good chemical stability against electrolyte eroding[132]. Mo_2C is a representative transition metal carbide and attracts tremendous attention due to its Pt-like structure[133]. However, its ORR and OER activity in non-aqueous Li-O_2 systems is still lacking[134]. In response, Sun et al.[130] recently proposed a three-dimensional foam consists of N-doped carbon-decorated Mo_2C nanorods (Mo_2C-NR@11NC). It is revealed that the poor performance of Mo_2C is ascribed to the parasitic reaction between surface oxidized $MoO_{2+\delta}$ and Li_2O_2 to form Li_xMoO_3, which cannot be electrochemically decomposed. The N-doped carbon serves as a protective coating that suppresses the participation of $MoO_{2+\delta}$ in parasitic reactions (Figure 2.12b). The protected Mo_2C-NR@11NC cathode delivers a discharge capacity of 6962 mAh g^{-1} (at 100 mA g^{-1}) and exhibits a cyclability of 200 cycles (at 100 mA g^{-1} and 500 mAh g^{-1}) with an overpotential of 0.28 V during the first cycle.

Transition metal nitrides, notably CoN_4, exhibit metallic properties due to the presence of the metal-metal bond, with N covalently bonds to metal at the interstitial position. Recently, they have also been employed as cathode material for non-aqueous Li-O_2 batteries. Yoon et al.[131] proposed a brush-like CoN_4-decorated carbon nanofiber film as a cathode material. The surfaces of CoN_4 exhibit an amorphous CoO_x layer that protects the metallic Co_4N electrocatalyst. The CoO_x layer displays favorable LiO_2 adsorption ability, which promotes the formation of film-like Li_2O_2 via the surface growth pathway (Figure 2.12c). Co_4N can efficiently decompose the side products, leading to low overpotentials of 1.24 V and a good

cyclability of over 100 cycles (at 200 mA g^{-1} and 1000 mAh g^{-1}).

It is worth mentioning that these non-oxides can be subjected to nature oxidation over time[135] and lose their true electrochemical activity. Metal sulfides such as MoS_2 are metastable and often suffer from sulfur leaching and poor long-term stability[136]. Carbides and nitrides are generally considered to be chemically stable, but as the above two studies[130,131] indicate, they also show evidence of oxidations under high potentials and highly oxidative environments typically presented in non-aqueous Li-O_2 system. Once again, cautions should be taken when utilizing these novel materials.

2.4. Summary and Outlook

Much progress has been made for the development of non-aqueous Li-O_2 batteries in the past few years. The mechanisms for the generation of LiO_2 intermediates and the formation of Li_2O_2 are well-understood. By tuning cathode surfaces or selecting appropriate electrolyte, the formation of Li_2O_2 can be driven to follow either a solution growth pathway to form toroids or a surface growth pathway to form thin layers. For the oxidation of Li_2O_2, the role of the conventional solid catalyst is unclear. Through the design of cathode surfaces, the morphology, spatial distribution, and crystallinity of Li_2O_2 can be controlled, and the apparent high charge overpotential can be effectively reduced. Alternatively, soluble redox mediators are effective electrocatalysts for the oxidization of large Li_2O_2 toroids. The decompositions of the carbon cathodes and electrolyte have been identified as the origins for the formation of parasitic species such as Li_2CO_3. It is possible to suppress carbon corrosion by surface protection of carbon or employ carbon-free cathodes. On the other hand, the suppression of electrolyte decomposition may require the search for a novel electrolyte. Ideally, stable low-DN electrolyte solvent should be used, but it is also undesirable for Li_2O_2

growth via the solution growth pathway. It should be emphasized that the design for the cathodes, electrolyte, and redox mediators should not be considered in isolation. Integration of these elements should be adopted for the optimization of high performance non-aqueous Li-O_2 batteries.

Based on the above review, a personal outlook for the most promising approaches for future cathode design in non-aqueous Li-O_2 batteries are:

(i) To design a high pore volume cathode with macropores tailored for large Li_2O_2 toroids accommodation, which can provide high discharge capacity. These macroporous cathodes are generally carbon-based, therefore, the challenge of this approach is to incorporate electrocatalysts that can both enhance the OER performance and suppress the corrosion of carbon;

(ii) To design cathodes that promote the thickness of the thin layer Li_2O_2 deposited via surface growth pathway, which provides good discharge capacity performance and superior cyclability of the battery. The challenge of this approach is the rational design of cathode surfaces that promotes the formation of complete amorphous Li_2O_2, which has yet to be achieved.

In this thesis, Chapter 3 aims to identify an effective OER catalysts, namely NCO nanoplates. In Chapter 4, NCO nanoplates are utilized to enhance the OER and cycling performance of macroporous rGO aerogel to address the first proposed approach. Chapter 5 then aims to address the second approach, and a novel macroporous NCO@CNT cathode that promotes the formation of complete amorphous Li_2O_2 is proposed.

References

(1) Adams, B. D.; Radtke, C.; Black, R.; Trudeau, M. L.; Zaghib, K.; Nazar, L. F. Current Density Dependence of Peroxide Formation in the Li-O_2 Battery and Its Effect on Charge. *Energy Environ. Sci.* **2013**, *6* (6), 1772.

(2) Safari, M.; Adams, B. D.; Nazar, L. F. Kinetics of Oxygen Reduction in Aprotic Li-O_2 Cells: A Model-Based Study. *J. Phys. Chem. Lett.* **2014**, *5* (20), 3486–3491.

(3) Lu, J.; Li, L.; Park, J.-B.; Sun, Y.-K.; Wu, F.; Amine, K. Aprotic and Aqueous Li-O_2 Batteries. *Chem. Rev.* **2014**, *114* (11), 5611–5640.

(4) Kwabi, D. G.; Tułodziecki, M.; Pour, N.; Itkis, D. M.; Thompson, C. V.; Shao-Horn, Y. Controlling Solution-Mediated Reaction Mechanisms of Oxygen Reduction Using Potential and Solvent for Aprotic Lithium-Oxygen Batteries. *J. Phys. Chem. Lett.* **2016**, *7* (7), 1204–1212.

(5) Lim, H.-K.; Lim, H.-D.; Park, K.-Y.; Seo, D.-H.; Gwon, H.; Hong, J.; Goddard, W. A.; Kim, H.; Kang, K. Toward a Lithium-"Air" Battery: The Effect of CO_2 on the Chemistry of a Lithium-Oxygen Cell. *J. Am. Chem. Soc.* **2013**, *135* (26), 9733–9742.

(6) Luo, L.; Liu, B.; Song, S.; Xu, W.; Zhang, J.-G.; Wang, C. Revealing the Reaction Mechanisms of Li-O_2 Batteries Using Environmental Transmission Electron Microscopy. *Nat. Nanotechnol.* **2017**, *12* (6), 535–539.

(7) Peng, Z.; Chen, Y.; Bruce, P. G.; Xu, Y. Direct Detection of the Superoxide Anion as a Stable Intermediate in the Electroreduction of Oxygen in a Non-Aqueous Electrolyte Containing Phenol as a Proton Source. *Angew. Chem. Int. Ed.* **2015**, *54* (28), 8165–8168.

(8) Hassoun, J.; Croce, F.; Armand, M.; Scrosati, B. Investigation of the O_2 Electrochemistry in a Polymer Electrolyte Solid-State Cell. *Angew. Chem. Int. Ed.* **2011**, *50* (13), 2999–3002.

(9) Aetukuri, N. B.; McCloskey, B. D.; García, J. M.; Krupp, L. E.; Viswanathan, V.; Luntz, A. C. Solvating Additives Drive Solution-Mediated Electrochemistry and Enhance Toroid Growth in Non-Aqueous Li-O_2 Batteries. *Nat. Chem.* **2015**, *7* (1), 50–56.

(10) Johnson, L.; Li, C.; Liu, Z.; Chen, Y.; Freunberger, S. A.; Ashok, P. C.; Praveen, B. B.; Dholakia, K.; Tarascon, J.-M.; Bruce, P. G. The Role of LiO_2 Solubility in O_2 Reduction in Aprotic Solvents and Its Consequences for Li-O_2 Batteries. *Nat. Chem.* **2014**, *6* (12), 1091–1099.

(11) Viswanathan, V.; Nørskov, J. K.; Speidel, A.; Scheffler, R.; Gowda, S.; Luntz, A. C. Li-O_2 Kinetic Overpotentials: Tafel Plots from Experiment and First-Principles Theory. *J. Phys. Chem. Lett.* **2013**, *4* (4), 556–560.

(12) Viswanathan, V.; Thygesen, K. S.; Hummelshøj, J. S.; Nørskov, J. K.; Girishkumar, G.; Mccloskey, B. D.; Luntz, A. C. Electrical Conductivity in Li_2O_2 and Its Role in Determining Capacity Limitations in Non-Aqueous Li-O_2 Batteries. *J. Chem. Phys.* **2011**, *135* (21), 214704.

(13) Yin, Y.; Gaya, C.; Torayev, A.; Thangavel, V.; Franco, A. A. Impact of Li_2O_2 Particle Size on Li-O_2 Battery Charge Process: Insights from a Multiscale Modeling Perspective. *J. Phys. Chem. Lett.* **2016**, *7* (19), 3897–3902.

(14) Xia, C.; Waletzko, M.; Chen, L.; Peppler, K.; Klar, Peter. J.; Janek, J. Evolution of Li_2O_2 Growth and Its Effect on Kinetics of Li-O_2 Batteries. *ACS Appl. Mater. Interfaces* **2014**, *6* (15), 12083–12092.

(15) Mitchell, R. R.; Gallant, B. M.; Shao-Horn, Y.; Thompson, C. V. Mechanisms of Morphological Evolution of Li_2O_2 Particles during Electrochemical Growth. *J. Phys. Chem. Lett.* **2013**, *4* (7), 1060–1064.

(16) Mahne, N.; Fontaine, O.; Thotiyl, M. O.; Wilkening, M.; Freunberger, S. A. Mechanism and Performance of Lithium-Oxygen Batteries - a Perspective. *Chem. Sci.* **2017**, *8* (10), 6716–6729.

(17) Lyu, Z.; Zhou, Y.; Dai, W.; Cui, X.; Lai, M.; Wang, L.; Huo, F.; Huang, W.; Hu, Z.; Chen, W. Recent Advances in Understanding of the Mechanism and Control of Li_2O_2 Formation in Aprotic Li-O_2 Batteries. *Chem. Soc. Rev.* **2017**, *46* (19), 6046–6072.

(18) Lau, S.; Archer, L. A. Nucleation and Growth of Lithium Peroxide in the Li-O_2 Battery. *Nano Lett.* **2015**, *15* (9), 5995–6002.

(19) Yilmaz, E.; Yogi, C.; Yamanaka, K.; Ohta, T.; Byon, H. R. Promoting Formation of Noncrystalline Li_2O_2 in the Li-O_2 Battery with RuO_2 Nanoparticles. *Nano Lett.* **2013**, *13* (10), 4679–4684.

(20) Yang, Y.; Zhang, T.; Wang, X.; Chen, L.; Wu, N.; Liu, W.; Lu, H.; Xiao, L.; Fu, L.; Zhuang, L. Tuning the Morphology and Crystal Structure of Li_2O_2: A Graphene Model Electrode Study for Li-O_2 Battery. *ACS Appl. Mater. Interfaces* **2016**, *8* (33), 21350–21357.

(21) Lyu, Z.; Yang, L.; Luan, Y.; Renshaw Wang, X.; Wang, L.; Hu, Z.; Lu, J.; Xiao, S.; Zhang, F.; Wang, X.; et al. Effect of Oxygen Adsorbability on the Control of Li_2O_2 Growth in Li-O_2 Batteries: Implications for Cathode Catalyst Design. *Nano Energy* **2017**, *36*, 68–75.

(22) Ramaswamy, N.; Mukerjee, S. Influence of Inner- and Outer-Sphere Electron Transfer Mechanisms during Electrocatalysis of Oxygen Reduction in Alkaline Media. *J. Phys. Chem. C* **2011**, *115* (36), 18015–18026.

(23) Liu, W.-M.; Gao, T.-T.; Yang, Y.; Sun, Q.; Fu, Z.-W. A Hierarchical Three-Dimensional $NiCo_2O_4$ Nanowire Array/Carbon Cloth as an Air Electrode for Nonaqueous Li-Air Batteries. *Phys. Chem. Chem. Phys.* **2013**, *15* (38), 15806–15810.

(24) Lu, J.; Lei, Y.; Lau, K. C.; Luo, X.; Du, P.; Wen, J.; Assary, R. S.; Das, U.; Miller, D. J.; Elam, J. W.; et al. A Nanostructured Cathode Architecture for Low Charge Overpotential in Lithium-Oxygen Batteries. *Nat. Commun.* **2013**, *4*, 2383.

(25) Tran, C.; Kafle, J.; Yang, X.-Q.; Qu, D. Increased Discharge Capacity of a Li-Air Activated Carbon Cathode Produced by Preventing Carbon Surface Passivation. *Carbon* **2011**, *49* (4), 1266–1271.

(26) Wong, R. A.; Dutta, A.; Yang, C.; Yamanaka, K.; Ohta, T.; Nakao, A.; Waki, K.; Byon, H. R. Structurally Tuning Li_2O_2 by Controlling the Surface Properties of Carbon Electrodes: Implications for Li-O_2 Batteries. *Chem. Mater.* **2016**, *28* (21), 8006–8015.

(27) Dutta, A.; Wong, R. A.; Park, W.; Yamanaka, K.; Ohta, T.; Jung, Y.; Byon, H. R. Nanostructuring One-Dimensional and Amorphous Lithium Peroxide for High Round-Trip Efficiency in Lithium-Oxygen Batteries. *Nat. Commun.* **2018**, *9* (1).

(28) Tu, F.; Hu, J.; Xie, J.; Cao, G.; Zhang, S.; Yang, S. A.; Zhao, X.; Yang, H. Y. Au-Decorated Cracked Carbon Tube Arrays as Binder-Free Catalytic Cathode Enabling Guided Li_2O_2 Inner Growth for High-Performance Li-O_2 Batteries. *Adv. Funct. Mater.* **2016**, *26* (42), 7725–7732.

(29) Tang, C.; Sun, P.; Xie, J.; Tang, Z.; Yang, Z.; Dong, Z.; Cao, G.; Zhang, S.; Braun, P. V.; Zhao, X. Two-Dimensional IrO_2/MnO_2 Enabling Conformal Growth of Amorphous Li_2O_2 for High-Performance Li-O_2 Batteries. *Energy Storage Mater.* **2017**, *9*, 206–213.

(30) Aurbach, D.; McCloskey, B. D.; Nazar, L. F.; Bruce, P. G. Advances in Understanding Mechanisms Underpinning Lithium-Air Batteries. *Nat. Energy* **2016**, *1* (9), 16128.

(31) Gutmann, V. Solvent Effects on the Reactivities of Organometallic Compounds. *Coord. Chem. Rev.* **1976**, *18* (2), 225–255.

(32) Burke, C. M.; Pande, V.; Khetan, A.; Viswanathan, V.; McCloskey, B. D. Enhancing Electrochemical Intermediate Solvation Through Electrolyte Anion Selection to Increase Nonaqueous Li-O_2 Battery Capacity. *Proc. Natl. Acad. Sci.* **2015**, *112* (30), 9293–9298.

(33) Kwabi, D. G.; Batcho, T. P.; Feng, S.; Giordano, L.; Thompson, C. V.; Shao-Horn, Y. The Effect of Water on Discharge Product Growth and Chemistry in Li-O_2 Batteries. *Phys. Chem. Chem. Phys.* **2016**, *18* (36), 24944–24953.

(34) Li, F.; Wu, S.; Li, D.; Zhang, T.; He, P.; Yamada, A.; Zhou, H. The Water Catalysis at Oxygen Cathodes of Lithium-Oxygen Cells. *Nat. Commun.* **2015**, *6*, 7843–7843.

(35) Schwenke, K. U.; Metzger, M.; Restle, T.; Piana, M.; Gasteiger, H. A. The Influence of Water and Protons on Li_2O_2 Crystal Growth in Aprotic Li-O_2 Cells. *J. Electrochem. Soc.* **2015**, *162* (4), A573–A584.

(36) Cho, M. H.; Trottier, J.; Gagnon, C.; Hovington, P.; Clément, D.; Vijh, A.; Kim, C.-S.; Guerfi, A.; Black, R.; Nazar, L.; et al. The Effects of Moisture Contamination in the Li-O_2 Battery. *J. Power Sources* **2014**, *268*, 565–574.

(37) Luntz, A. C.; McCloskey, B. D. Nonaqueous Li-Air Batteries: A Status Report. *Chem. Rev.* **2014**, *114* (23), 11721–11750.

(38) McCloskey, B. D.; Valery, A.; Luntz, A. C.; Gowda, S. R.; Wallraff, G. M.; Garcia, J. M.; Mori, T.; Krupp, L. E. Combining Accurate O_2 and Li_2O_2 Assays to Separate Discharge and Charge Stability Limitations in Nonaqueous Li-O_2 Batteries. *J. Phys. Chem. Lett.* **2013**, *4* (17), 2989–2993.

(39) Lu, J.; Jung Lee, Y.; Luo, X.; Chun Lau, K.; Asadi, M.; Wang, H.-H.; Brombosz, S.; Wen, J.; Zhai, D.; Chen, Z.; et al. A Lithium-Oxygen Battery Based on Lithium Superoxide. *Nature* **2016**, *529*, 377–382.

(40) Gao, X.; Chen, Y.; Johnson, L.; Bruce, P. G. Promoting Solution Phase Discharge in Li-O_2 Batteries Containing Weakly Solvating Electrolyte Solutions. *Nat. Mater.* **2016**, *15* (8), 882–888.

(41) McCloskey, B. D.; Bethune, D. S.; Shelby, R. M.; Girishkumar, G.; Luntz, A. C. Solvents' Critical Role in Nonaqueous Lithium-Oxygen Battery Electrochemistry. *J. Phys. Chem. Lett.* **2011**, *2* (10), 1161–1166.

(42) Khetan, A.; Luntz, A.; Viswanathan, V. Trade-Offs in Capacity and Rechargeability in Nonaqueous Li-O_2 Batteries: Solution-Driven Growth Versus Nucleophilic Stability. *J. Phys. Chem. Lett.* **2015**, *6* (7), 1254–1259.

(43) Peng, Z.; Freunberger, S. A.; Hardwick, L. J.; Chen, Y.; Giordani, V.; Bardé, F.; Novák, P.; Graham, D.; Tarascon, J.-M.; Bruce, P. G. Oxygen Reactions in a Non-Aqueous Li^+ Electrolyte. *Angew. Chem. Int. Ed.* **2011**, *50* (28), 6351–6355.

(44) Hummelshøj, J. S.; Luntz, A. C.; Nørskov, J. K. Theoretical Evidence for Low Kinetic Overpotentials in Li-O_2 Electrochemistry. *J. Chem. Phys.* **2013**, *138* (3), 034703.

(45) Wang, J.; Zhang, Y.; Guo, L.; Wang, E.; Peng, Z. Identifying Reactive Sites and Transport Limitations of Oxygen Reactions in Aprotic Lithium-O_2 Batteries at the Stage of Sudden Death. *Angew. Chem. Int. Ed.* **2016**, *55* (17), 5201–5205.

(46) Mekonnen, Y. S.; Garcia-Lastra, J. M.; Hummelshøj, J. S.; Jin, C.; Vegge, T. Role of Li_2O_2@Li_2CO_3 Interfaces on Charge Transport in Nonaqueous Li-Air Batteries. *J. Phys. Chem. C* **2015**, *119* (32), 18066–18073.

(47) McCloskey, B. D.; Speidel, A.; Scheffler, R.; Miller, D. C.; Viswanathan, V.; Hummelshøj, J. S.; Nørskov, J. K.; Luntz, A. C. Twin Problems of Interfacial Carbonate Formation in Nonaqueous Li-O_2 Batteries. *J. Phys. Chem. Lett.* **2012**, *3* (8), 997–1001.

(48) Halder, A.; Wang, H.-H.; Lau, K. C.; Assary, R. S.; Lu, J.; Vajda, S.; Amine, K.; Curtiss, L. A. Identification and Implications of Lithium Superoxide in Li-O_2 Batteries. *ACS Energy Lett.* **2018**, *3* (5), 1105–1109.

(49) Kang, S.; Mo, Y.; Ong, S. P.; Ceder, G. A Facile Mechanism for Recharging Li_2O_2 in Li-O_2 Batteries. *Chem. Mater.* **2013**, *25* (16), 3328–3336.

(50) Ganapathy, S.; Adams, B. D.; Stenou, G.; Anastasaki, M. S.; Goubitz, K.; Miao, X.-F.; Nazar, L. F.; Wagemaker, M. Nature of Li_2O_2 Oxidation in a Li-O_2 Battery Revealed by *Operando* X-Ray Diffraction. *J. Am. Chem. Soc.* **2014**, *136* (46), 16335–16344.

(51) Hong, M.; Yang, C.; Wong, R. A.; Nakao, A.; Choi, H. C.; Byon, H. R. Determining the Facile Routes for Oxygen Evolution Reaction by In Situ Probing of Li-O_2 Cells with Conformal Li_2O_2 Films. *J. Am. Chem. Soc.* **2018**, *140* (20), 6190–6193.

(52) Tian, F.; Radin, M. D.; Siegel, D. J. Enhanced Charge Transport in Amorphous Li_2O_2. *Chem. Mater.* **2014**, *26* (9), 2952–2959.

(53) Zhang, Y.; Cui, Q.; Zhang, X.; McKee, W. C.; Xu, Y.; Ling, S.; Li, H.; Zhong, G.; Yang, Y.; Peng, Z. Amorphous Li_2O_2: Chemical Synthesis and Electrochemical Properties. *Angew. Chem. Int. Ed.* **2016**, *55* (36), 10717–10721.

(54) Wang, Y.; Yuan, H. Discharge Precipitate's Impact in Li-Air Battery: Comparison of Experiment and Model Predictions. *J. Electrochem. Soc.* **2017**, *164* (9), A2283–A2289.

(55) Chitturi, V. R.; Ara, M.; Fawaz, W.; Ng, K. Y. S.; Arava, L. M. R. Enhanced Lithium-Oxygen Battery Performances with Pt Subnanocluster Decorated N-Doped Single-Walled Carbon Nanotube Cathodes. *ACS Catal.* **2016**, *6* (10), 7088–7097.

(56) Li, Z.; Ganapathy, S.; Xu, Y.; Zhu, Q.; Chen, W.; Kochetkov, I.; George, C.; Nazar, L. F.; Wagemaker, M. Fe_2O_3 Nanoparticle Seed Catalysts Enhance Cyclability on Deep (Dis)Charge in Aprotic Li-O_2 Batteries. *Adv. Energy Mater.* **2018**, *8* (18), 1703513.

(57) Mo, Y.; Ong, S. P.; Ceder, G. First-Principles Study of the Oxygen Evolution Reaction of Lithium Peroxide in the Lithium-Air Battery. *Phys. Rev. B* **2011**, *84* (20), 205446.

(58) Song, K.; Agyeman, D. A.; Jung, J.; Jo, M. R.; Yang, J.; Kang, Y.-M. A Review of the Design Strategies for Tailored Cathode Catalyst Materials in Rechargeable Li-O_2 Batteries. *Isr. J. Chem.* **2015**, *55* (5), 458–471.

(59) Gao, R.; Zhu, J.; Xiao, X.; Hu, Z.; Liu, J.; Liu, X. Facet-Dependent Electrocatalytic Performance of Co_3O_4 for Rechargeable Li-O_2 Battery. *J. Phys. Chem. C* **2015**, *119* (9), 4516–4523.

(60) Zhu, J.; Wang, F.; Wang, B.; Wang, Y.; Liu, J.; Zhang, W.; Wen, Z. Surface Acidity as Descriptor of Catalytic Activity for Oxygen Evolution Reaction in Li-O_2 Battery. *J. Am. Chem. Soc.* **2015**, *137* (42), 13572–13579.

(61) Su, D.; Dou, S.; Wang, G. Single Crystalline Co_3O_4 Nanocrystals Exposed with Different Crystal Planes for Li-O_2 Batteries. *Sci. Rep.* **2014**, *4*, 5767.

(62) Radin, M. D.; Monroe, C. W.; Siegel, D. J. How Dopants Can Enhance Charge Transport in Li_2O_2. *Chem. Mater.* **2015**, *27* (3), 839–847.

(63) Yao, K. P. C.; Risch, M.; Sayed, S. Y.; Lee, Y.-L.; Harding, J. R.; Grimaud, A.; Pour, N.; Xu, Z.; Zhou, J.; Mansour, A.; et al. Solid-State Activation of Li_2O_2 Oxidation Kinetics and Implications for Li-O_2 Batteries. *Energy Environ. Sci.* **2015**, *8* (8), 2417–2426.

(64) Yao, X.; Dong, Q.; Cheng, Q.; Wang, D. Li-Oxygen Battery: Parasitic Reactions. In *Metal-Air Batteries*; Zhang, X., Ed.; Wiley-VCH Verlag GmbH & Co. KGaA: Weinheim, Germany, 2018; pp 95–124.

(65) Luntz, A. C.; McCloskey, B. D.; Gowda, S.; Horn, H.; Viswanathan, V. Cathode Electrochemistry in Nonaqueous Lithium Air Batteries. In *The Lithium Air Battery*;

Imanishi, N., Luntz, A. C., Bruce, P., Eds.; Springer New York, 2014; pp 59–120.

(66) Chen, Y.; Freunberger, S. A.; Peng, Z.; Fontaine, O.; Bruce, P. G. Charging a Li-O_2 Battery Using a Redox Mediator. *Nat. Chem.* **2013**, *5* (6), 489–494.

(67) Kundu, D.; Black, R.; Adams, B.; Nazar, L. F. A Highly Active Low Voltage Redox Mediator for Enhanced Rechargeability of Lithium-Oxygen Batteries. *ACS Cent. Sci.* **2015**, *1* (9), 510–515.

(68) Bergner, B. J.; Hofmann, C.; Schürmann, A.; Schröder, D.; Peppler, K.; Schreiner, P. R.; Janek, J. Understanding the Fundamentals of Redox Mediators in Li-O_2 Batteries: A Case Study on Nitroxides. *Phys. Chem. Chem. Phys.* **2015**, *17* (47), 31769–31779.

(69) Sun, D.; Shen, Y.; Zhang, W.; Yu, L.; Yi, Z.; Yin, W.; Wang, D.; Huang, Y.; Wang, J.; Wang, D.; et al. A Solution-Phase Bifunctional Catalyst for Lithium-Oxygen Batteries. *J. Am. Chem. Soc.* **2014**, *136* (25), 8941–8946.

(70) Yao, K. P. C.; Frith, J. T.; Sayed, S. Y.; Bardé, F.; Owen, J. R.; Shao-Horn, Y.; Garcia-Araez, N. Utilization of Cobalt Bis(Terpyridine) Metal Complex as Soluble Redox Mediator in Li-O_2 Batteries. *J. Phys. Chem. C* **2016**, *120* (30), 16290–16297.

(71) Lim, H.-D.; Song, H.; Kim, J.; Gwon, H.; Bae, Y.; Park, K.-Y.; Hong, J.; Kim, H.; Kim, T.; Kim, Y. H.; et al. Superior Rechargeability and Efficiency of Lithium-Oxygen Batteries: Hierarchical Air Electrode Architecture Combined with a Soluble Catalyst. *Angew. Chem. Int. Ed.* **2014**, *53* (15), 3926–3931.

(72) Kwak, W.-J.; Park, S.-J.; Jung, H.-G.; Sun, Y.-K. Optimized Concentration of Redox Mediator and Surface Protection of Li Metal for Maintenance of High Energy Efficiency in Li-O_2 Batteries. *Adv. Energy Mater.* **2018**, *8* (9), 1702258.

(73) Park, J.-B.; Lee, S. H.; Jung, H.-G.; Aurbach, D.; Sun, Y.-K. Redox Mediators for Li-O_2 Batteries: Status and Perspectives. *Adv. Mater.* **2018**, *30* (1), 1704162.

(74) Kwak, W.-J.; Kim, H.; Jung, H.-G.; Aurbach, D.; Sun, Y.-K. Review-A Comparative Evaluation of Redox Mediators for Li-O_2 Batteries: A Critical Review. *J. Electrochem. Soc.* **2018**, *165* (10), A2274–A2293.

(75) Ottakam Thotiyl, M. M.; Freunberger, S. A.; Peng, Z.; Bruce, P. G. The Carbon Electrode in Nonaqueous Li-O_2 Cells. *J. Am. Chem. Soc.* **2013**, *135* (1), 494–500.

(76) Xie, J.; Yao, X.; Cheng, Q.; Madden, I. P.; Dornath, P.; Chang, C.-C.; Fan, W.; Wang, D. Three Dimensionally Ordered Mesoporous Carbon as a Stable, High-Performance Li-O_2 Battery Cathode. *Angew. Chem.* **2015**, *127* (14), 4373–4377.

(77) Bae, Y.; Ko, D.-H.; Lee, S.; Lim, H.-D.; Kim, Y.-J.; Shim, H.-S.; Park, H.; Ko, Y.; Park, S. K.; Kwon, H. J.; et al. Enhanced Stability of Coated Carbon Electrode for Li-O_2 Batteries and Its Limitations. *Adv. Energy Mater.* **2018**, *8* (16), 1702661.

(78) Yuan, J.; Liu, Z.; Wen, Y.; Hu, H.; Zhu, Y.; Thangadurai, V. Hierarchical Carbon-Free $NiCo_2O_4$ Cathode for Li-O_2 Batteries. *Ionics* **2018**.

(79) Liu, Z.; Feng, N.; Shen, Z.; Li, F.; He, P.; Zhang, H.; Zhou, H. Carbon-Free O_2 Cathode with Three-Dimensional Ultralight Nickel Foam-Supported Ruthenium Electrocatalysts for Li-O_2 Batteries. *ChemSusChem* **2017**, *10* (13), 2714–2719.

(80) Yang, H.; Xia, J.; Bromberg, L.; Dimitrov, N.; Whittingham, M. S. Electrochemically Synthesized Nanoporous Gold as a Cathode Material for Li-O_2 Batteries. *J. Solid State Electrochem.* **2017**, *21* (2), 463–468.

(81) Hong, M.; Choi, H. C.; Byon, H. R. Nanoporous NiO Plates with a Unique Role for Promoted Oxidation of Carbonate and Carboxylate Species in the Li-O_2 Battery. *Chem. Mater.* **2015**, *27* (6), 2234–2241.

(82) Song, S.; Xu, W.; Zheng, J.; Luo, L.; Engelhard, M. H.; Bowden, M. E.; Liu, B.; Wang, C.-M.; Zhang, J.-G. Complete Decomposition of Li_2CO_3 in Li-O_2 Batteries Using Ir/B_4C as Noncarbon-Based Oxygen Electrode. *Nano Lett.* **2017**, *17* (3), 1417–1424.

(83) Balaish, M.; Kraytsberg, A.; Ein-Eli, Y. A Critical Review on Lithium-Air Battery Electrolytes. *Phys. Chem. Chem. Phys.* **2014**, *16* (7), 2801–2822.

(84) McCloskey, B. D.; Scheffler, R.; Speidel, A.; Bethune, D. S.; Shelby, R. M.; Luntz, A. C. On the Efficacy of Electrocatalysis in Nonaqueous Li-O_2 Batteries. *J. Am. Chem. Soc.* **2011**, *133* (45), 18038–18041.

(85) Rus, E. D.; Wang, H.; Wang, D.; Abruña, H. D. A Mechanistic Differential Electrochemical Mass Spectrometry (DEMS) and in Situ Fourier Transform Infrared Investigation of Dimethoxymethane Electro-Oxidation at Platinum. *J. Phys. Chem. C* **2011**, *115* (27), 13293–13302.

(86) Veerakumar, P.; Thanasekaran, P.; Subburaj, T.; Lin, K.-C. A Metal-Free Carbon-Based Catalyst: An Overview and Directions for Future Research. *C* **2018**, *4* (4), 54.

(87) Lim, H.-D.; Yun, Y. S.; Cho, S. Y.; Park, K.-Y.; Song, M. Y.; Jin, H.-J.; Kang, K. All-Carbon-Based Cathode for a True High-Energy-Density Li-O_2 Battery. *Carbon* **2017**, *114*, 311–316.

(88) Liu, Q.-C.; Liu, T.; Liu, D.-P.; Li, Z.-J.; Zhang, X.-B.; Zhang, Y. A Flexible and Wearable Lithium-Oxygen Battery with Record Energy Density Achieved by the Interlaced Architecture Inspired by Bamboo Slips. *Adv. Mater.* **2016**, *28* (38), 8413–8418.

(89) Kim, K.; P. Kim, M.; Lee, W.-G. Preparation and Evaluation of Mesoporous Carbon Derived from Waste Materials for Hybrid-Type Li-Air Batteries. *New J. Chem.* **2017**, *41* (17), 8864–8869.

(90) He, M.; Zhang, P.; Liu, L.; Liu, B.; Xu, S. Hierarchical Porous Nitrogen Doped Three-Dimensional Graphene as a Free-Standing Cathode for Rechargeable Lithium-Oxygen Batteries. *Electrochim. Acta* **2016**, *191*, 90–97.

(91) Nong, J.; Xie, P.; Zhu, A. S.; Rong, M. Z.; Zhang, M. Q. Highly Conductive Doped Carbon Framework as Binder-Free Cathode for Hybrid Li-O_2 Battery. *Carbon* **2019**, *142*, 177–189.

(92) Han, J.; Guo, X.; Ito, Y.; Liu, P.; Hojo, D.; Aida, T.; Hirata, A.; Fujita, T.; Adschiri, T.; Zhou, H.; et al. Effect of Chemical Doping on Cathodic Performance of Bicontinuous Nanoporous Graphene for Li-O_2 Batteries. *Adv. Energy Mater.* **2016**, *6* (3), 1501870.

(93) Wei, M.; Li, B.; Jin, C.; Ni, Y.; Li, C.; Pan, X.; Sun, J.; Yang, C.; Yang, R. A 3D Free-Standing Thin Film Based on N, P-Codoped Hollow Carbon Fibers Embedded with Mop Quantum Dots as High Efficient Oxygen Electrode for Li-O_2 Batteries. *Energy Storage Mater.* **2019**, *17*, 226–233.

(94) Wu, F.; Xing, Y.; Li, L.; Qian, J.; Qu, W.; Wen, J.; Miller, D.; Ye, Y.; Chen, R.; Amine, K.; et al. Facile Synthesis of Boron-Doped rGO as Cathode Material for High Energy Li-O_2 Batteries. *ACS Appl. Mater. Interfaces* **2016**, *8* (36), 23635–23645.

(95) Xu, S.-M.; Liang, X.; Ren, Z.-C.; Wang, K.-X.; Chen, J.-S. Free-Standing Air Cathodes Based on 3D Hierarchically Porous Carbon Membranes: Kinetic Overpotential of Continuous Macropores in Li-O_2 Batteries. *Angew. Chem.* **2018**, *130* (23), 6941–6945.

(96) Oh, D.; Ozgit-Akgun, C.; Akca, E.; Thompson, L. E.; Tadesse, L. F.; Kim, H.-C.; Demirci, G.; Miller, R. D.; Maune, H. Biotemplating Pores with Size and Shape Diversity for Li-Oxygen Battery Cathodes. *Sci. Rep.* **2017**, *7* (1), 45919.

(97) Kim, D. Y.; Kim, M.; Kim, D. W.; Suk, J.; Park, J. J.; Park, O. O.; Kang, Y. Graphene Paper with Controlled Pore Structure for High-Performance Cathodes in Li-O_2 Batteries. *Carbon* **2016**, *100*, 265–272.

(98) Shen, C.; Liu, T.; Zhang, M.; Hendrickson, M. A.; Plichta, E. J.; Zheng, J. P. Macroporous Carbon Nanotube (CNT) Foams as Li-Air Battery Cathodes. *ECS Trans.* **2017**, *77* (11), 239–248.

(99) Torayev, A.; Magusin, P. C. M. M.; Grey, C. P.; Merlet, C.; Franco, A. A. Importance of Incorporating Explicit 3D-Resolved Electrode Mesostructures in Li-O_2 Battery Models. *ACS Appl. Energy Mater.* **2018**, *1* (11), 6433–6441.

(100) Bui, H. T.; Kim, D. Y.; Kim, D. W.; Suk, J.; Kang, Y. Carbon Nanofiber@platinum by a Coaxial Electrospinning and Their Improved Electrochemical Performance as a Li-O_2 Battery Cathode. *Carbon* **2018**, *130*, 94–104.

(101) Huang, H.; Luo, S.; Liu, C.; Wang, Q.; Wang, Z.; Zhang, Y.; Hao, A.; Liu, Y.; Li, J.; Zhai, Y.; et al. Ag-Decorated Highly Mesoporous Co_3O_4 Nanosheets on Nickel Foam as an Efficient Free-Standing Cathode for Li-O_2 Batteries. *J. Alloys Compd.* **2017**, *726*, 939–946.

(102) Yang, J.; Mi, H.; Luo, S.; Li, Y.; Zhang, P.; Deng, L.; Sun, L.; Ren, X. Atomic Layer Deposition of TiO_2 on Nitrogen-Doped Carbon Nanofibers Supported Ru Nanoparticles for Flexible Li-O_2 Battery: A Combined DFT and Experimental Study. *J. Power Sources* **2017**, *368*, 88–96.

(103) Luo, C.; Sun, H.; Jiang, Z.; Guo, H.; Gao, M.; Wei, M.; Jiang, Z.; Zhou, H.; Sun, S.-G. Electrocatalysts of Mn and Ru Oxides Loaded on MWCNTS with 3D Structure and Synergistic Effect for Rechargeable Li-O_2 Battery. *Electrochim. Acta* **2018**, *282*, 56–63.

(104) Kumar, S.; Munichandraiah, N. Nanoparticles of a Pt_3Ni Alloy on Reduced Graphene Oxide (rGO) as an Oxygen Electrode Catalyst in a Rechargeable Li-O_2 Battery. *Mater. Chem. Front.* **2017**.

(105) Leng, L.; Li, J.; Zeng, X.; Song, H.; Shu, T.; Wang, H.; Liao, S. Enhancing the Cyclability of Li-O_2 Batteries Using PdM Alloy Nanoparticles Anchored on Nitrogen-Doped Reduced Graphene as the Cathode Catalyst. *J. Power Sources* **2017**, *337*, 173–179.

(106) Zhao, C.; Yu, C.; Banis, M. N.; Sun, Q.; Zhang, M.; Li, X.; Liu, Y.; Zhao, Y.; Huang, H.; Li, S.; et al. Decoupling Atomic-Layer-Deposition Ultrafine RuO_2 for High-Efficiency and Ultralong-Life Li-O_2 Batteries. *Nano Energy* **2017**, *34*, 399–407.

(107) Huang, J.; Jin, Z.; Xu, Z.-L.; Qin, L.; Huang, H.; Sadighi, Z.; Yao, S.; Cui, J.; Huang, B.; Kim, J.-K. Porous RuO_2 Nanosheet/CNT Electrodes for DMSO-Based Li-O_2 and Li Ion O_2 Batteries. *Energy Storage Mater.* **2017**, *8*, 110–118.

(108) Yang, Y.; Liu, W.; Wu, N.; Wang, X.; Zhang, T.; Chen, L.; Zeng, R.; Wang, Y.; Lu, J.; Fu, L.; et al. Tuning the Morphology of Li_2O_2 by Noble and 3d Metals: A Planar Model Electrode Study for Li-O_2 Battery. *ACS Appl. Mater. Interfaces* **2017**, *9* (23), 19800–19806.

(109) Tan, A.; Reddy, M. V.; Adams, S. Synthesis and Application of Nanostructured MCo_2O_4(M=Co, Ni) for Hybrid Li-Air Batteries. *Ionics* **2017**, 1–14.

(110) Sadighi, Z.; Huang, J.; Qin, L.; Yao, S.; Cui, J.; Kim, J.-K. Positive Role of Oxygen Vacancy in Electrochemical Performance of $CoMn_2O_4$ Cathodes for Li-O_2 Batteries. *J. Power Sources* **2017**, *365*, 134–147.

(111) Wang, J.; Gao, R.; Zhou, D.; Chen, Z.; Wu, Z.; Schumacher, G.; Hu, Z.; Liu, X. Boosting the Electrocatalytic Activity of Co_3O_4 Nanosheets for a Li-O_2 Battery through Modulating Inner Oxygen Vacancy and Exterior Co^{3+}/Co^{2+} Ratio. *ACS Catal.* **2017**, *7* (10), 6533–6541.

(112) Gu, T.-H.; Agyeman, D. A.; Shin, S.-J.; Jin, X.; Lee, J. M.; Kim, H.; Kang, Y.-M.; Hwang, S.-J. α-MnO_2 Nanowire-Anchored Highly Oxidized Cluster as a Catalyst for Li-O_2 Batteries: Superior Electrocatalytic Activity and High Functionality. *Angew. Chem. Int. Ed.* **2018**, *57* (49), 15984–15989.

(113) Gong, Y.; Ding, W.; Li, Z.; Su, R.; Zhang, X.; Wang, J.; Zhou, J.; Wang, Z.; Gao, Y.; Li, S.; et al. Inverse Spinel Cobalt-Iron Oxide and N-Doped Graphene Composite as an Efficient and Durable Bifuctional Catalyst for Li-O_2 Batteries. *ACS Catal.* **2018**, *8* (5), 4082–4090.

(114) Kim, J. G.; Kim, Y.; Noh, Y.; Lee, S.; Kim, Y.; Kim, W. B. Bifunctional Hybrid Catalysts with Perovskite $LaCo_{0.8}Fe_{0.2}O_3$ Nanowires and Reduced Graphene Oxide Sheets for an Efficient Li-O_2 Battery Cathode. *ACS Appl. Mater. Interfaces* **2018**, *10* (6), 5429–5439.

(115) Cong, Y.; Geng, Z.; Sun, Y.; Yuan, L.; Wang, X.; Zhang, X.; Wang, L.; Zhang, W.; Huang, K.; Feng, S. Cation Segregation of A-Site Deficiency Perovskite $La_{0.85}FeO_{3-\delta}$ Nanoparticles toward High-Performance Cathode Catalysts for Rechargeable Li-O_2 Battery. *ACS Appl. Mater. Interfaces* **2018**, *10* (30), 25465–25472.

(116) Kang, J.; Kim, J.; Lee, S.; Wi, S.; Kim, C.; Hyun, S.; Nam, S.; Park, Y.; Park, B. Breathable Carbon-Free Electrode: Black TiO_2 with Hierarchically Ordered Porous

Structure for Stable Li-O_2 Battery. *Adv. Energy Mater.* **2017**, *7* (19), 1700814.

(117) Hu, X.; Wang, J.; Li, Z.; Wang, J.; Gregory, D. H.; Chen, J. MCNTs@MnO_2 Nanocomposite Cathode Integrated with Soluble O_2-Carrier Co-Salen in Electrolyte for High-Performance Li-Air Batteries. *Nano Lett.* **2017**, *17* (3), 2073–2078.

(118) Huang, J.; Zhang, B.; Bai, Z.; Guo, R.; Xu, Z.-L.; Sadighi, Z.; Qin, L.; Zhang, T.-Y.; Chen, G.; Huang, B.; et al. Anomalous Enhancement of Li-O_2 Battery Performance with Li_2O_2 Films Assisted by $NiFeO_x$ Nanofiber Catalysts: Insights into Morphology Control. *Adv. Funct. Mater.* **2016**, *26* (45), 8290–8299.

(119) Zhang, X.; Wang, C.; Chen, Y.-N.; Wang, X.-G.; Xie, Z.; Zhou, Z. Binder-Free $NiFe_2O_4$/C Nanofibers as Air Cathodes for Li-O_2 Batteries. *J. Power Sources* **2018**, *377*, 136–141.

(120) Song, Z.; Qin, X.; Cao, N.; Gao, X.; Liang, Q.; Huo, Y. Mesoporous CoO/Reduced Graphene Oxide as Bi-Functional Catalyst for Li-O_2 Battery with Improved Performances. *Mater. Chem. Phys.* **2018**, *203*, 302–309.

(121) Song, Z.; Cao, N.; Gao, X.; Liang, Q.; Qin, X. Ultrathin Co_3O_4 Nanosheets Highly Dispersed on Reduced Graphene Oxide: An Efficient Bi-Functional Catalyst for Li-O_2 Battery. *Fuller. Nanotub. Carbon Nanostructures* **2017**, *25* (2), 65–70.

(122) Wu, H.; Sun, W.; Wang, Y.; Wang, F.; Liu, J.; Yue, X.; Wang, Z.; Qiao, J.; Rooney, D. W.; Sun, K. Facile Synthesis of Hierarchical Porous Three-Dimensional Free-Standing $MnCo_2O_4$ Cathodes for Long-Life Li-O_2 Batteries. *ACS Appl. Mater. Interfaces* **2017**, *9* (14), 12355–12365.

(123) Sennu, P.; Park, H. S.; Park, K. U.; Aravindan, V.; Nahm, K. S.; Lee, Y.-S. Formation of $NiCo_2O_4$ Rods Over Co_3O_4 Nanosheets as Efficient Catalyst for Li-O_2 Batteries and Water Splitting. *J. Catal.* **2017**, *349*, 175–182.

(124) Lee, Y. J.; Kim, D. H.; Kang, T.-G.; Ko, Y.; Kang, K.; Lee, Y. J. Bifunctional MnO_2-Coated Co_3O_4 Hetero-Structured Catalysts for Reversible Li-O_2 Batteries. *Chem. Mater.* **2017**, *29* (24), 10542–10550.

(125) Xue, H.; Wu, S.; Tang, J.; Gong, H.; He, P.; He, J.; Zhou, H. Hierarchical Porous Nickel Cobaltate Nanoneedle Arrays as Flexible Carbon-Protected Cathodes for High-Performance Lithium-Oxygen Batteries. *ACS Appl. Mater. Interfaces* **2016**, *8* (13), 8427–8435.

(126) Ramakrishnan, P.; Shanmugam, S.; Kim, J. H. Dual Heteroatom-Doped Carbon Nanofoam Wrapped Iron Monosulfide Nanoparticles: An Efficient Cathode Catalyst for Li-O_2 Batteries. *ChemSusChem* **2017**, 1554–1562.

(127) Long, J.; Hu, A.; Shu, C.; Wang, S.; Li, J.; Liang, R. Three-Dimensional Flower-Like MoS_2@Carbon Nanotube Composites with Interconnected Porous Networks and High Catalytic Activity as Cathode for Lithium-Oxygen Batteries. *ChemElectroChem* **2018**, *5* (19), 2816–2824.

(128) Hu, A.; Long, J.; Shu, C.; Liang, R.; Li, J. Three-Dimensional Interconnected Network Architecture with Homogeneously Dispersed Carbon Nanotubes and Layered MoS_2 as a Highly Efficient Cathode Catalyst for Lithium-Oxygen Battery.

ACS Appl. Mater. Interfaces **2018**, *10* (40), 34077–34086.

(129) Zhang, S.; Huang, Z.; Wen, Z.; Zhang, L.; Jin, J.; Shahbazian-Yassar, R.; Yang, J. Local Lattice Distortion Activate Metastable Metal Sulfide as Catalyst with Stable Full Discharge-Charge Capability for Li-O_2 Batteries. *Nano Lett.* **2017**, *17* (6), 3518–3526.

(130) Sun, G.; Zhao, Q.; Wu, T.; Lu, W.; Bao, M.; Sun, L.; Xie, H.; Liu, J. 3D Foam-Like Composites of Mo_2C Nanorods Coated by N-Doped Carbon: A Novel Self-Standing and Binder-Free O_2 Electrode for Li-O_2 Batteries. *ACS Appl. Mater. Interfaces* **2018**, *10* (7), 6327–6335.

(131) Yoon, K. R.; Shin, K.; Park, J.; Cho, S.-H.; Kim, C.; Jung, J.-W.; Cheong, J. Y.; Byon, H. R.; Lee, H. M.; Kim, I.-D. Brush-Like Cobalt Nitride Anchored Carbon Nanofiber Membrane: Current Collector-Catalyst Integrated Cathode for Long Cycle Li-O_2 Batteries. *ACS Nano* **2018**, *12* (1), 128–139.

(132) Yang, Y.; Qin, Y.; Xue, X.; Wang, X.; Yao, M.; Huang, H. Intrinsic Properties Affecting the Catalytic Activity of 3d Transition-Metal Carbides in Li-O_2 Battery. *J. Phys. Chem. C* **2018**, *122* (31), 17812–17819.

(133) Yang, Z.-D.; Chang, Z.-W.; Zhang, Q.; Huang, K.; Zhang, X.-B. Decorating Carbon Nanofibers with Mo_2C Nanoparticles towards Hierarchically Porous and Highly Catalytic Cathode for High-Performance Li-O_2 Batteries. *Sci. Bull.* **2018**, *63* (7), 433–440.

(134) Xing, Y.; Yang, Y.; Chen, R.; Luo, M.; Chen, N.; Ye, Y.; Qian, J.; Li, L.; Wu, F.; Guo, S. Strongly Coupled Carbon Nanosheets/Molybdenum Carbide Nanocluster Hollow Nanospheres for High-Performance Aprotic Li-O_2 Battery. *Small* **2018**, *14* (19), 1704366.

(135) Kozmenkova, A. Ya.; Kataev, E. Yu.; Belova, A. I.; Amati, M.; Gregoratti, L.; Velasco-Vélez, J.; Knop-Gericke, A.; Senkovsky, B.; Vyalikh, D. V.; Itkis, D. M.; et al. Tuning Surface Chemistry of TiC Electrodes for Lithium-Air Batteries. *Chem. Mater.* **2016**, *28* (22), 8248–8255.

(136) Luo, Z.; Ouyang, Y.; Zhang, H.; Xiao, M.; Ge, J.; Jiang, Z.; Wang, J.; Tang, D.; Cao, X.; Liu, C.; et al. Chemically Activating MoS_2 Via Spontaneous Atomic Palladium Interfacial Doping Towards Efficient Hydrogen Evolution. *Nat. Commun.* **2018**, *9* (1), 2120.

Chapter 3 Improving Non-Aqueous Li-O_2 Battery Performance by Tuning Cathodic $NiCo_2O_4$ Nanostructures

3.1. Introduction and Significance

Recent studies in non-aqueous Li-O_2 batteries have focused on developing novel nanostructured cathode materials with a vast variety of morphologies. However, there is a lack of understanding of how the nanostructures of cathode materials can influence their performance in non-aqueous Li-O_2 batteries. This work aims to explore the relationship between cathodic $NiCo_2O_4$ nanostructures and battery performance through systematic investigation of crystal planes, surface areas and active sites of $NiCo_2O_4$. The output provides new insights into future rational design of transition metal oxide cathode materials and paves way for the development of novel macroporous cathodes. The highlights of this work include:

1. For the first time, various $NiCo_2O_4$ nanoplates with identical morphologies but different exposed crystal planes were synthesized, rendering it possible to clarify the authentic impact of crystal planes in lieu of morphology contribution.
2. The crystal plane effect of $NiCo_2O_4$ in non-aqueous Li-O_2 batteries were demonstrated through the investigation of {111} and {112} crystal planes exposed $NiCo_2O_4$ nanoplates, which concluded that {112} crystal planes are more active towards OER than {111} crystal planes.
3. The crucial roles of Ni^{3+} in $NiCo_2O_4$ in non-aqueous Li-O_2 systems were elucidated through the investigations of the {112} crystal planes with different Ni compositions, and it was discovered that Ni^{3+} is able to improve the conductance of $Ni_xCo_{3-x}O_4$ ($0 \leq x \leq 1.5$) as well as the OER activity.

3.2. Improving Non-Aqueous Li-O_2 Battery Performance by Tuning Cathodic $NiCo_2O_4$ Nanostructures

This section is included as an unsubmitted manuscript by Heng Wang, Qi Bi, Haihui Wang, Sheng Dai, Improving Non-Aqueous Li-O_2 Battery Performance by Tuning Cathodic $NiCo_2O_4$ Nanostructures

Statement of Authorship

Title of Paper	Improving Non-aqueous Li-O_2 Battery Performance by Tuning Cathodic $NiCo_2O_4$ Nanostructures
Publication Status	☐ Published ☐ Accepted for Publication ☐ Submitted for Publication ☑ Unpublished and Unsubmitted work written in manuscript style
Publication Details	To be submitted

Principal Author

Name of Principal Author (Candidate)	Heng Wang
Contribution to the Paper	Research plan, material synthesis, material characterization, battery performance evaluation, data analysis, and manuscript drafting and editing.
Overall percentage (%)	85%
Certification:	This paper reports on original research I conducted during the period of my Higher Degree by Research candidature and is not subject to any obligations or contractual agreements with a third party that would constrain its inclusion in this thesis. I am the primary author of this paper.
Signature	Date 30/04/2019

Co-Author Contributions

By signing the Statement of Authorship, each author certifies that:

i. the candidate's stated contribution to the publication is accurate (as detailed above);

ii. permission is granted for the candidate in include the publication in the thesis; and

iii. the sum of all co-author contributions is equal to 100% less the candidate's stated contribution.

Name of Co-Author	Qi Bi
Contribution to the Paper	Discussion of research plan
Signature	Date 02/05/2019

Name of Co-Author	Prof. Haihui Wang
Contribution to the Paper	Help to evaluate and edit manuscript
Signature	Date 30/04/2019

Name of Co-Author	Prof. Sheng Dai
Contribution to the Paper	Supervision for the development of work and manuscript evaluation
Signature	Date 30 April 2019

Please cut and paste additional co-author panels here as required.

Improving Non-Aqueous Li-O_2 Battery Performance by Tuning Cathodic $NiCo_2O_4$ Nanostructures

Heng Wang,[†] Qi Bi,[†] Haihui Wang,[*,†,‡] Sheng Dai [*,†,§]

† School of Chemical Engineering and Advanced Materials, The University of Adelaide, Adelaide, South Australia 5005, Australia

‡ School of Chemistry & Chemical Engineering, South China University of Technology, 381 Wushan Road, Guangzhou 510640, China

§ Department of Chemical Engineering, Brunel University London, Uxbridge, UB8 3PH, United Kingdom

Corresponding author

*E-mail: hhwang@scut.edu.cn

*E-mail: s.dai@adelaide.edu.au

Abstract

Non-aqueous Li-O_2 battery has been considered as a promising energy storage technology due to its high energy density but suffers from low round-trip efficiency and poor long-term stability. Transition metal oxides such as $NiCo_2O_4$ reveal high electrochemical performance, however, there is a lack of understanding of how the nanostructures of these electrocatalysts, especially $NiCo_2O_4$, influence overall battery performance. As a model example, $NiCo_2O_4$ nanoplates were synthesized via a facile hydrothermal approach followed by calcination. The relationship between $NiCo_2O_4$ nanostructure and electrocatalytic performance was systematically evaluated through the investigation of crystal plane effect, surface areas and bulk compositions of cathodic $NiCo_2O_4$ in non-aqueous Li-O_2 systems. The {112} crystal planes of $NiCo_2O_4$ nanoplates are more active than {111} due to their higher dangling bond density and availability of active octahedral Co^{3+} and Ni^{3+}. Ni^{3+} is found to be able to improve the OER activity as well as overall material conductance, which plays an essential role in improving the performance of cathodic $NiCo_2O_4$. The effects of crystal planes, surface areas and Ni^{3+} active sites of $NiCo_2O_4$ in non-aqueous Li-O_2 systems are elucidated, which provides a new strategy for the rational design of high-performance cathodic materials for non-aqueous Li-O_2 batteries.

Keywords: non-aqueous Li-O_2 battery, electrocatalyst, crystal plane effect, surface area, conductance, $NiCo_2O_4$

Introduction

Recently, rechargeable non-aqueous Li-O_2 batteries have gained considerable attention as a promising energy storage technology owing to their remarkably high practical energy densities, i.e., specific energy of ~3600 $W \cdot h \cdot kg^{-1}$.[1] In a typical Li-O_2 battery discharge-recharge cycle, the discharge product of Li_2O_2 is deposited on cathode surfaces during discharge via an oxygen reduction reaction (ORR) ($2Li^+ + O_2 + 2e^- \rightarrow Li_2O_2$). On the other hand, the deposited Li_2O_2 is decomposed during the recharge process via an oxygen evolution reaction (OER) ($Li_2O_2 \rightarrow 2Li^+ + O_2 + 2e^-$). The high polarization, low round-trip efficiency, poor long-term stability and the overall ineffectiveness of the OER process are mainly caused by insulating nature of solid Li_2O_2[2–5]. In order to alleviate the issues of high overpotential and poor cyclability in rechargeable non-aqueous Li-O_2 batteries, a great variety of electrocatalysts, such as precious metals (e.g., Pd), their alloys (e.g., PtRu) and transition metal oxides (e.g., MnO_2, Fe_3O_4)[6–9], have been proposed as cathode materials. Novel nanostructured electrocatalysts (e.g., 3D aerogel constructed from ultrathin MnO_2 nanosheets[10]) and advanced nano-heterostructures (e.g., mushroom-like Au/$NiCo_2O_4$ nanohybrid on 3D graphene grown directly on the skeleton of Ni foam[11]) are also explored as cathode materials to further enhance battery performance. Despite the vast variety in morphology design, there is a lack of understanding of how electrocatalyst nanostructures affect overall ORR and OER activities[12]. Therefore, there is an urgent need to establish the correlation between the nanostructure and the ORR/OER activity of electrocatalysts to guide rational electrocatalyst design for high-performance Li-O_2 batteries.

In a non-aqueous Li-O_2 system, electrochemistry during ORR and OER occurs on cathode surfaces. Therefore, the surface atom arrangement of the electrocatalytic active surfaces on

the cathode can play a critical role in the enhancement of electrocatalytic activity. Experimentally, by the selective synthesis of nanocrystals predominantly exposing specific crystal planes, the surface atom arrangement, exposure of specific active sites and the number of dangling bonds on these nanocrystals can be tuned[13]. Unlike previous morphology control, crystal plane control enables a deeper control over the electrocatalyst active surface at an atomic level. Well-shaped nanocrystals of Pd[14], Au[15], TiO_2[16], etc. enclosed by different crystal planes have been studied extensively as models to probe the surface activity in various reactions such as CO oxidation. Recently, scarce studies on the crystal plane effect of Co_3O_4 in non-aqueous Li-O_2 batteries have been reported[17,18]. Song et al.[17] compared the {001} crystal planes exposed Co_3O_4 nanocubes with the {112} crystal planes exposed Co_3O_4 nanoplates. Co^{3+} on the {112} crystal planes are highly active towards OER and ORR, and the {112} crystal planes with abundant Co^{3+} on surface exhibit considerably improved long-term stability than that of {001} crystal planes. However, these studies on the electrocatalysts with different exposed crystal planes express drastically different morphologies[19–21], and it is difficult to preclude the contribution from morphology.

$NiCo_2O_4$ has been widely investigated in the fields of supercapacitors[22,23], lithium-ion batteries[24,25] and water splitting[26,27], owing to its rich electrochemical properties and relatively high conductivity (two magnitudes higher than Co_3O_4[28]). $NiCo_2O_4$ should be an ideal candidate with promising electrochemical activities to fulfill the requirements for non-aqueous Li-O_2 batteries, and some studies on morphology designs ranging from 0D nanoparticles to 3D nanoflowers have been reported lately[29–33]. However, to our best knowledge, there is no study on how $NiCo_2O_4$ crystal planes and active sites influence the performance of non-aqueous Li-O_2 batteries.

In this study, we systematically investigated the contributions of the crystal planes, surface areas and bulk compositions of $NiCo_2O_4$ as cathode materials to the electrochemical performance in non-aqueous Li-O_2 systems. Both {111} and {112} crystal planes exposed $NiCo_2O_4$ nanoplates with comparable morphologies were prepared to identify crystal plane impact in lieu of morphology contribution. The effect of surface areas as a critical descriptor is investigated by simply tuning the temperature of $NiCo_2O_4$ calcination. The cathodic active sites contribution to battery performance is evaluated by tailoring Ni content in the $NiCo_2O_4$ lattices, and the roles of Ni^{3+} in the improvement of $NiCo_2O_4$ cathode material are highlighted. Through this investigation, an in-depth understanding of catalyst structures - electrochemical performance relationship in non-aqueous Li-O_2 batteries is concluded, where the $NiCo_2O_4$ exposed with highly active {112} crystal planes together with high surface areas and conductance demonstrates structure advantages as an effective electrocatalyst for non-aqueous Li-O_2 batteries.

Experimental

Materials. All regents were of analytical grade and were used as received without further purification**.** Cobalt nitrate hexahydrate ($Co(NO_3)_2 \cdot 6H_2O$), nickel nitrate hexahydrate ($Ni(NO_3)_2 \cdot 6H_2O$), polyvinylpyrrolidone (PVP, M_w = 55,000), hexamethylenetetramine (HMTA) and N-methyl-2-pyrrolidone (NMP) were purchased from Sigma-Aldrich. Sodium hydroxide, acetone, Ketjen black (KB) carbon and polyvinylidene fluoride (PVDF) were supplied by Chem-Supply. Glass fiber membrane (Grade GF/F) was from Whatman. Lithium foil was obtained from China Energy Lithium Co., Ltd. 1 M lithium bis(trifluoromethanesulfonyl)imide (LiTFSI) in tetraethylene glycol dimethyl ether

(TEGDME) was acquired from Suzhou Qianmin Chemical Reagent Co., Ltd. Ultra-high purity (99.999%) O_2 was provided by Coregas.

Synthesis of Cathodic Materials. The {111} crystal planes exposed $NiCo_2O_4$ (111-$NiCo_2O_4$) nanoplates were synthesized according to a previous method with modification[20]. 5.6 mmol $Co(NO_3)_2 \cdot 6H_2O$ and 2.8 mmol $Ni(NO_3)_2 \cdot 6H_2O$ were dissolved in a 20 mL mixed solvent of ethanol: DI water with a 1:1 volume. 2.0 g PVP was added to the above mixture. After stirring at room temperature for 0.5 h, 50 mL 0.4 M NaOH was added dropwise to form a blue suspension, which was transferred to a Teflon-lined autoclave. The autoclave was heated and maintained at 120 ℃ for 15 h and then allowed to cool to room temperature naturally. The product was washed with acetone and water several times, collected via centrifuge and dried at 60 ℃. The dried product was finally heated in air to 350 ℃ at a slow heating rate of 2 ℃ min^{-1} and maintained for 2 h.

The {112} crystal planes exposed $NiCo_2O_4$ (112-$NiCo_2O_4$) nanoplates were synthesized according to a previous method with modification[19]. 3.0 mmol $Co(NO_3)_2 \cdot 6H_2O$ and 1.5 mmol $Ni(NO_3)_2 \cdot 6H_2O$ were dissolved in 30 mL DI water. To this mixture, 1.5 mmol HMTA in another 30 mL DI water was added under constant stirring at room temperature. After stirring for 0.5 h, the pH of the solution was adjusted to 10 with 1 M NaOH. The green suspension was stirred at room temperature for another 2 h and transferred to a Teflon-lined autoclave. The autoclave was heated and maintained at 120 ℃ for 24 h and then allowed to cool to room temperature naturally. The raw product was washed with water several times until the supernatant was clear. The precipitate phase was collected by centrifugation and dried at 60 ℃. The dried product was calcined in air to 350 ℃ at a slow heating rate of 2 ℃ min^{-1} and maintained for 2 h. To prepare the 112-$NiCo_2O_4$ samples with different

surface areas, the dried precursor was calcined at 400 ℃ instead of 350 ℃. The 112-$Ni_xCo_{3-x}O_4$ ($0 \leq x \leq 1.5$) samples with different Ni contents were prepared by varying the initial feed molar ratios of Co and Ni salts (0, 0.2, 1.0 in correspond to the targeted compositions of 112-$Ni_xCo_{3-x}O_4$, x = 0, 0.5, 1.5), followed by the calcination at 350 ℃.

Material Characterization. X-ray diffraction (XRD) measurements were conducted on a Rigaku Miniflex 600 instrument using Cu Kα radiation in the 2-Theta range of 3-80° at a scan rate of 5 ° min^{-1}. Scanning electron microscopy (SEM) images were obtained on an FEI Quanta 450 operating at an accelerating voltage of 30 kV. SEM samples were prepared by dropping ethanol suspensions of the synthesized catalyst samples on silicon wafers. Transmission electron microscopy (TEM) images were obtained on a Tecnai G2 Spirit operating at an accelerating voltage of 120 kV. High-resolution TEM (HRTEM) images were obtained on a Philips CM200 operating at an accelerating voltage of 200 kV. TEM samples were prepared by dropping the ethanol suspensions of samples on carbon-coated copper grids and drying at 60 ℃ overnight. Brunauer-Emmett-Teller (BET) specific surface areas were calculated by nitrogen adsorption-desorption measurements on a Belsorp-Max instrument at 77 K after sample degassing at 100 ℃ overnight, and pore size distributions were calculated via the Barrett-Joyner-Halenda (BJH) method. Fourier transform infrared spectroscopy (FTIR) was conducted on a Nicolet 6700 spectrometer in the wavenumber range of 1000-400 cm^{-1}.

Electrochemical Measurements. To prepare the $NiCo_2O_4$/KB cathode, a slurry of well-mixed $NiCo_2O_4$, KB and PVDF binder (weight ratio 3:6:1) in NMP was coated on a Ni foam and dried at 80 ℃ overnight. The loading of slurry on the cathode was ca. 0.65 mg cm^{-2}. For comparison, the KB cathode with KB and PVDF binder (weight ratio 9:1) but no $NiCo_2O_4$

was also prepared following the same procedure. A coin-type battery was assembled in an argon-filled glove box, with Li foil as an anode, glass fiber membrane as a separator, and 1 M LiTFSI in TEGDME as the electrolyte. The assembled battery was transferred to a glass chamber, which was purged with ultra-high purity O_2 for 15 min. The galvanostatic discharge-charge profile of the battery was measured on a Neware battery testing system within a potential window of 2.0-4.5 V (*vs.* Li/Li^+) at a current density of 200 mA g^{-1}. Cyclic voltammetry (CV) of the battery was performed on a CHI600 electrochemical workstation within a potential window of 2.0-4.5 V (*vs.* Li/Li^+) at a scanning rate of 1 mV S^{-1}. Electrochemical impedance spectroscopy (EIS) was performed on a Zahner IM6 electrochemical workstation at an open circuit voltage (~2.85 V) in the frequency range of 100 mHz to 100 kHz. All specific capacities and current densities have been normalized based on the mass of KB.

Results and Discussion

Material Synthesis and Characterization

The {111} crystal planes exposed $NiCo_2O_4$ (111-$NiCo_2O_4$) nanoplates were synthesized with the aid of PVP via a hydrothermal method followed by calcination. The 111-$NiCo_2O_4$ precursors (Ni-Co mixed hydroxide) from their SEM images (Figure S3.1a) are hexagonal plates with a circumradius of 150-250 nm, featuring smooth surfaces and sharp edges. After calcination at 350 °C, the morphology of 111-$NiCo_2O_4$ is well preserved (Figure 3.1a). The TEM image (Figure 3.1b) displays a typical freestanding 111-$NiCo_2O_4$ nanoplate, containing 2 nm mesopores on the surface. These mesopores are generated from water escape during the decomposition of metal hydroxides to metal oxides. Figure 3.1c shows the lattice

resolved HRTEM image of 111-$NiCo_2O_4$. The corresponding crystal lattices can be indexed to (20-2), (0-22), (2-20) planes with d-spacings of 0.28, 0.28 and 0.28 nm along the [111] axis, which confirms the exposed crystal planes are {111}, in accordance with the FFT pattern (Figure 3.1c insert). Likewise, the {112} crystal planes exposed $NiCo_2O_4$ (112-$NiCo_2O_4$) nanoplates were synthesized with the aid of HMTA. SEM (Figure 3.1d) and TEM (Figure 3.1e) images reveal that 112-$NiCo_2O_4$ nanoplates are mesoporous (~ 2 nm in size) hexagonal nanoplates with a circumradius of 150-250 nm, which resembles the 111-$NiCo_2O_4$ nanoplates. According to the HRTEM image (Figure 3.1f) of a single freestanding 112-$NiCo_2O_4$, the crystal lattices can be indexed to (11-1), (1-31), (0-20) planes with the d-spacings of 0.46, 0.24 and 0.28 nm along the [112] axis and confirming the dominant exposed crystal planes are {112}, in accordance with the FFT pattern (Figure 3.1f insert).

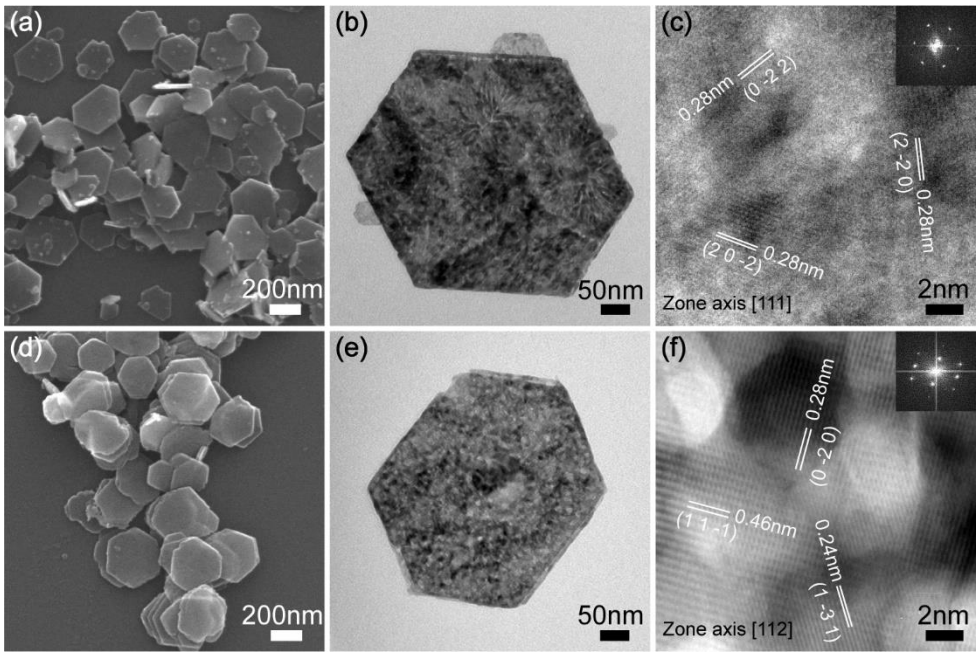

Figure 3.1. SEM (a), TEM (b) and HRTEM (c) images (insert: corresponding FFT pattern) of 111-$NiCo_2O_4$; SEM (d), TEM (e) and HRTEM (f) images (insert: corresponding FFT pattern) of 112-$NiCo_2O_4$.

The crystal structures of 111-$NiCo_2O_4$ and 112-$NiCo_2O_4$ were confirmed by XRD (Figure 3.2a). The XRD patterns of both samples show well-resolved diffraction peaks, which can be indexed to $NiCo_2O_4$ (JCPDS: 73-1702) with a well-crystalline phase. The BET porosities and specific surface areas of 111-$NiCo_2O_4$ and 112-$NiCo_2O_4$ were characterized by measuring their nitrogen adsorption-desorption isotherms at 77 K. As shown in Figure 3.2b, the isotherm curve of 111-$NiCo_2O_4$ can be recognized as a typical type IV adsorption curve with an obvious hysteresis loop at high P/P_0. The pore size distribution (Figure 3.2b insert) confirms the existence of 2.0 nm mesopores with a narrow size distribution. The BET specific surface area is calculated to be 71.4 $m^2\ g^{-1}$. Similarly, 112-$NiCo_2O_4$ exhibits a type IV isotherm curve with a hysteresis loop and its BET surface area is calculated to be 63.4 $m^2\ g^{-1}$ with a narrow mesopore distribution curve centered at 2.0 nm. Both 111-$NiCo_2O_4$ and 112-$NiCo_2O_4$ nanoplates show high specific surface areas and ordered mesopores, which can provide numerous active sites towards ORR and OER[34]. Most importantly, these samples make it possible to investigate the authentic effect of crystal planes to ORR/OER catalytic performance in lieu of morphology contribution.

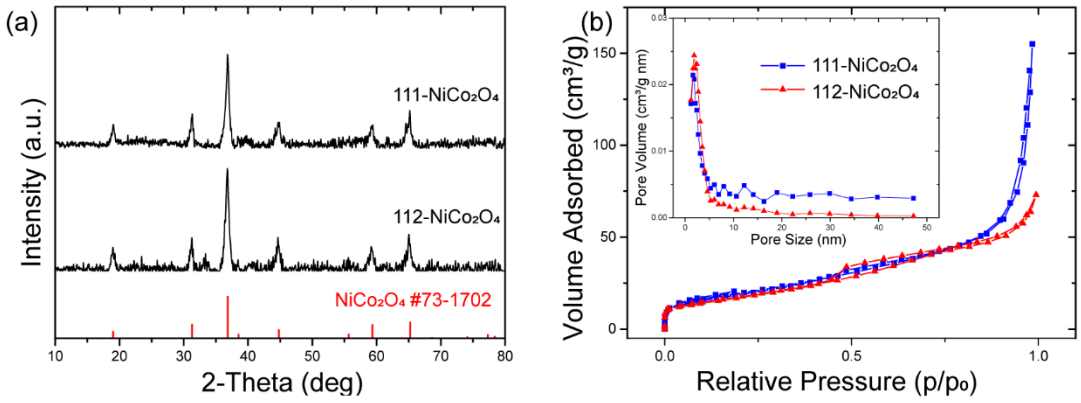

Figure 3.2. (a) XRD patterns of 111-$NiCo_2O_4$ and 112-$NiCo_2O_4$, (b) nitrogen adsorption-desorption isotherms and corresponding pore size distributions (insert) of 111-$NiCo_2O_4$ and 112-$NiCo_2O_4$.

Effect of Crystal Plane

The synthesized 111-$NiCo_2O_4$ and 112-$NiCo_2O_4$ nanoplates were mixed with KB and employed as cathodes for non-aqueous Li-O_2 batteries. Figure 3.3a compares the galvanostatic discharge-charge profiles of the KB, 111-$NiCo_2O_4$/KB and 112-$NiCo_2O_4$/KB cathodes. While being discharged to a cut-off potential of 2.0 V at a current density of 200 mA g^{-1}, they deliver different specific capacities of 4104, 5400, and 5727 mAh g^{-1}. The presence of $NiCo_2O_4$ leads to a slight increase in specific capacity and discharge potential plateau. The capacity difference between 111-$NiCo_2O_4$/KB and 112-$NiCo_2O_4$/KB is marginal, implying weak contribution of the exposed crystal planes to the ORR performance. During recharge, KB cathode can only restore ~1900 mAh g^{-1}, while both 111-$NiCo_2O_4$/KB and 112-$NiCo_2O_4$/KB cathodes can fully restore their specific capacities with the plateaus at ~ 4.2 V. Notably, the charge potential rapidly rises to the plateau at only ~ 30 % state of charge (~1600 mAh g^{-1}) for 111-$NiCo_2O_4$/KB cathode, while the potential of 112-$NiCo_2O_4$/KB cathode grows moderately and does not reach the plateau till being charged to ~ 60 % state of charge (~3500 mAh g^{-1}), suggesting superior OER activity of 112-$NiCo_2O_4$. CV measurements were performed to further probe the electrocatalytic activities of the KB, 111-$NiCo_2O_4$/KB and 112-$NiCo_2O_4$/KB cathodes with their CV curves being shown in Figure 3.3b. For all three cathodes, the peaks at ~2.3 V in the forward direction can be attributed to the formation of Li_2O_2 during ORR, and the peaks at ~3.3V and ~3.6 V in the reverse direction can be attributed to the decomposition of LiO_2 and Li_2O_2 during OER[35]. Compared with 111-$NiCo_2O_4$/KB and KB cathodes, the current improvement in the forward direction for 112-$NiCo_2O_4$/KB is marginal, but the current improvement in the reverse

direction is much more significant. These results confirm the marginally improved ORR and superior OER catalytic activity of 112-$NiCo_2O_4$ as electrocatalysts.

The cyclabilities of KB, 111-$NiCo_2O_4$/KB and 112-$NiCo_2O_4$/KB cathodes were examined at a current density of 200 mA g^{-1} and a cut-off capacity of 500 mAh g^{-1} (Figures 3.3c-e) to evaluate their long-term stability. For the initial discharges, both 111-$NiCo_2O_4$/KB and 112-$NiCo_2O_4$/KB cathodes show marginally lower discharge overpotential (0.28 V) than that of KB (0.30 V). Although both 111-$NiCo_2O_4$ and 112-$NiCo_2O_4$ show improved ORR activity, the improvement is limited. $NiCo_2O_4$ contributes to marginal ORR improvement[36,37], but the contribution to OER is significant and thus, $NiCo_2O_4$ is mainly regarded as an OER electrocatalyst. After recharge, the charge overpotentials of KB, 111-$NiCo_2O_4$/KB and 112-$NiCo_2O_4$/KB cathodes are 1.04, 0.90 and 0.67 V during first cycle. The low charge potential for 112-$NiCo_2O_4$/KB cathode can effectively alleviate the parasitic reactions that dominatingly occur at high potentials, thus prolong the cyclability of cathodes[38]. As a result, the 112-$NiCo_2O_4$/KB cathode can sustain for the first 50 cycles without noticeable degradation and fails after 61 cycles, while the capacities of 111-$NiCo_2O_4$/KB and KB cathodes fade away rapidly after 35 and 18 cycles (Figure 3.3f). Evidently, 112-$NiCo_2O_4$ exhibits superior cycling performance ascribed to its high OER activity. Because 111-$NiCo_2O_4$ and 112-$NiCo_2O_4$ exhibit similar sizes, morphologies and specific surface areas, the only difference contributing to the above performance can be fully identified as the effect of crystal planes.

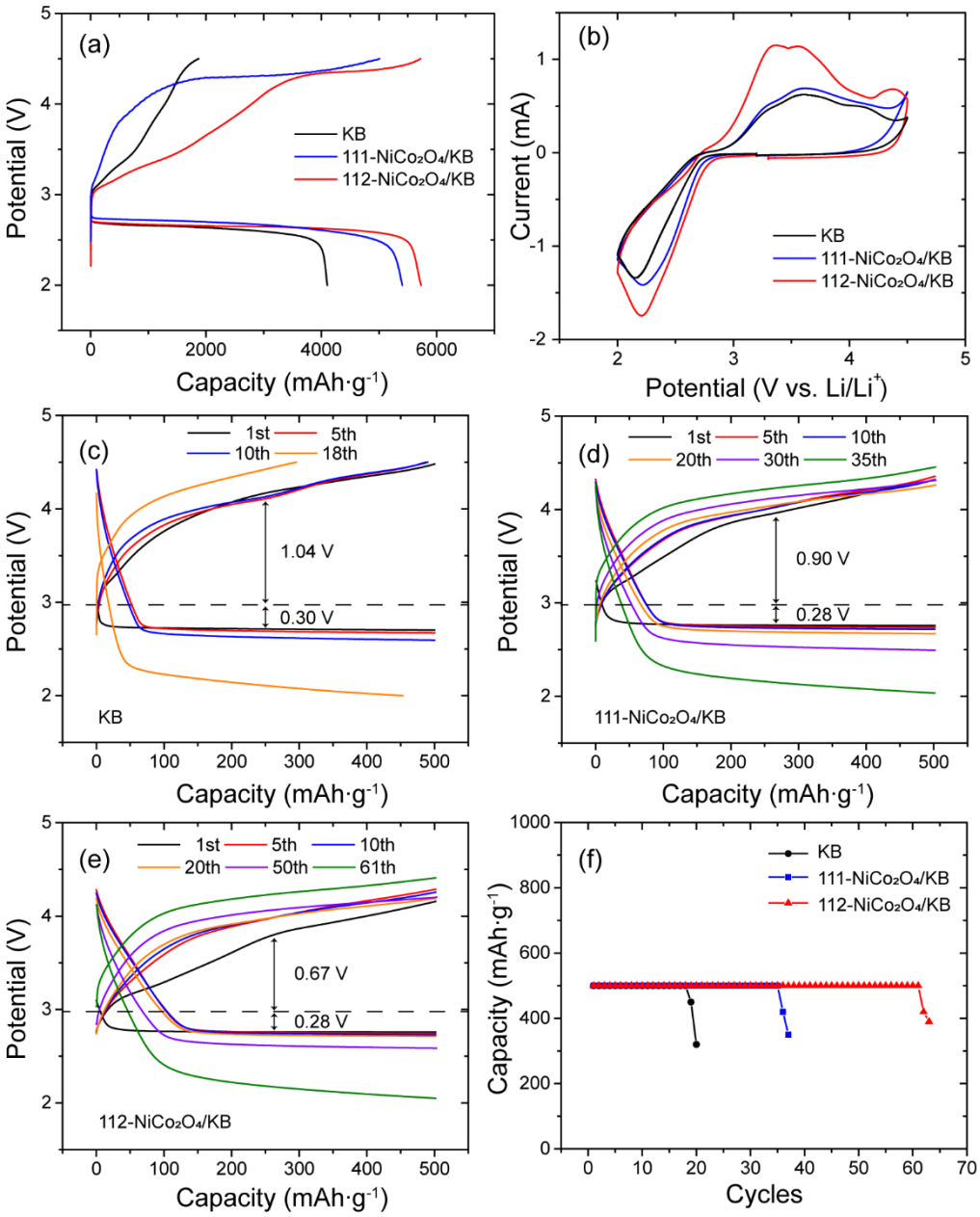

Figure 3.3. (a) Galvanostatic discharge-charge profiles of KB, 111-$NiCo_2O_4$/KB and 112-$NiCo_2O_4$/KB cathodes at a current density of 200 mA g^{-1} and in the potential window of 2.0-4.5 V; (b) the CV curves of KB, 111-$NiCo_2O_4$/KB and 112-$NiCo_2O_4$/KB cathodes; the cycling performance of (c) KB, (d) 111-$NiCo_2O_4$/KB, (e) 112-$NiCo_2O_4$/KB cathodes at 200 mA g^{-1} and limit capacity of 500 mAh g^{-1}; (f) a summary of the cycling performances of KB, 111-$NiCo_2O_4$/KB, and 112-$NiCo_2O_4$/KB cathodes.

The batteries were disassembled so that the cathodes at different discharge and charge status can be characterized by SEM. Figure S3.2a displays a pristine 112-$NiCo_2O_4$/KB cathode, where hexagonal 112-$NiCo_2O_4$ nanoplates scatter across the surface of porous KB. 112-$NiCo_2O_4$/KB is deeply discharged to 2.0 V to better visualize the deposited Li_2O_2 particles on electrode surface (Figure S3.2b). Figures S3.2c and S3.2d illustrate the cathode after being cycled at 200 mA g^{-1} and limited capacity of 500 mAh g^{-1} for 50 and 61 cycles. Even after 50 cycles, the cathode morphology is mostly recovered and no Li_2O_2 particles can be observed. However, after 61 cycles, KB and $NiCo_2O_4$ nanoplates are mostly covered underneath a layer of lithium carbonate by-products, blocking the electrochemically active cathode surface. The dysfunction of non-aqueous Li-O_2 batteries after cycling is mainly due to the irreversible accumulation of these by-products on cathode surfaces.

Effect of Surface Area

Further, it is favorable to develop $NiCo_2O_4$ with large surface areas associated with highly active {112} crystal planes. The specific surface areas of $NiCo_2O_4$ can be controlled by calcination temperature. Figure 3.4a compares the nitrogen adsorption-desorption isotherms and the pore size distributions of 112-$NiCo_2O_4$ nanoplates calcined at 350 and 400 ℃ (labeled as the 112-$NiCo_2O_4$-350C and 112-$NiCo_2O_4$-400C). Compared with 112-$NiCo_2O_4$-350C, 112-$NiCo_2O_4$-400C displays a similar type IV isotherm curve with a hysteresis loop but with a broader pore distribution curve centered at 4.0 nm. At an elevated calcination temperature of 400 ℃, the decomposition of mixed Ni-Co hydroxides is faster and generates larger and less-ordered mesopores, which can be observed from the TEM image as well (Figure S3.3). Consequently, the specific surface area of 112-$NiCo_2O_4$-400C is 41.5 m^2 g^{-1},

which is 35 % smaller than that of 112-$NiCo_2O_4$-350C. Evidently, high calcination temperature does not favor the formation of 112-$NiCo_2O_4$ nanoplates with ordered mesopores and higher specific surface areas. Figure 3.4b compares the first cycle curves of 112-$NiCo_2O_4$-350C/KB and 112-$NiCo_2O_4$-400C/KB cathodes cycled at 200 mA g^{-1} and limited capacity of 500 mAh g^{-1} (detailed profiles shown in Figure S3.4). The 112-$NiCo_2O_4$-400C/KB cathode shows a high charge overpotential of 0.93 V, which is 0.26 V higher than that of $NiCo_2O_4$-350C/KB. The 112-$NiCo_2O_4$-400C/KB cathode is only stable for 29 cycles (Figures 3.4c and S3.4). The reduced surface areas of 112-$NiCo_2O_4$-400C offer fewer active sites towards OER, which results in a higher charge potential and poor long-term stability. These results confirm that a high specific surface area plays a critical role in OER.

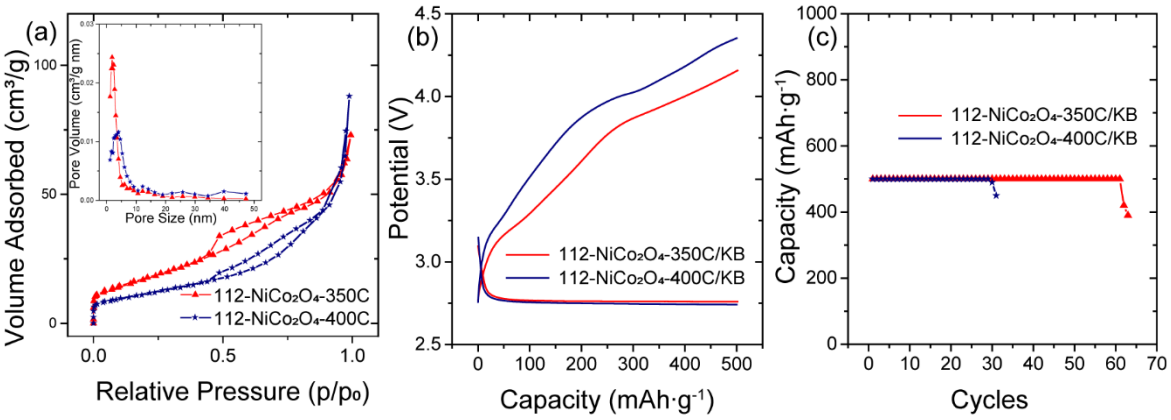

Figure 3.4. (a) The nitrogen adsorption-desorption isotherms and corresponding pore size distributions (insert) of 112-$NiCo_2O_4$-350C and 112-$NiCo_2O_4$-400C; (b) comparison on the first cycle curves of 112-$NiCo_2O_4$-350C/KB and 112-$NiCo_2O_4$-400C/KB cathodes at 200 mA g^{-1} and limit capacity of 500 mAh g^{-1}; (c) a summary of cycling performance of 112-$NiCo_2O_4$-350C/KB and 112-$NiCo_2O_4$-400C/KB cathodes.

Effect of Ni Concentration

To better understand why {112} crystal planes show higher OER activity than {111}, the crystal structures of {111} and {112} crystal planes of $NiCo_2O_4$ are examined. The ideal $NiCo_2O_4$ surface models are built by modification of a Co_3O_4 crystal. The octahedral (O_h) sites are occupied by both Co^{3+} and Ni^{3+} with a 1:1 ratio while the tetrahedral (T_d) sites are occupied by Co^{2+} (Figure 3.5)[39]. The stable {111} crystal planes are terminated by tetrahedral Co^{2+} with a single dangling bond, in comparison, the high-index {112} crystal planes are rough and feature more atomic kinks and steps with 3 Co^{2+} and 7 Co^{3+}/Ni^{3+} dangling bonds. It is well-known that the density of dangling bonds on a specific surface is directly correlated to its surface energy[40]. A large number of unsaturated Co^{2+}, Co^{3+} and Ni^{3+} on {112} crystal planes lead to high surface energy and high catalytic reactivity. In addition, the Ni^{3+} in $NiCo_2O_4$ has been reported to be more active than Co^{3+} in water splitting applications[41,42], but there is no report on its influence of OER activity in non-aqueous Li-O_2 system. Besides the {112} crystal planes providing more accessible $Co^{3+}(O_h)$ and $Ni^{3+}(O_h)$ to facilitate OER, it is hypnotized that $Ni^{3+}(O_h)$ also plays a crucial role in the OER activity.

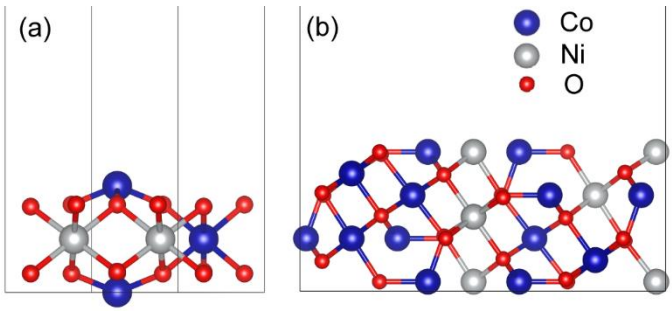

Figure 3.5. The crystal structures of the {111} and {112} crystal planes of $NiCo_2O_4$. The possible arrangement of Co^{3+} and Ni^{3+} at O_h sites is numerous, only a representative case is illustrated here.

The effect of Ni^{3+}on the electrocatalytic performance in non-aqueous Li-O_2 batteries were examined. Various 112-$Ni_xCo_{3-x}O_4$ ($0 \leq x \leq 1.5$) nanoplates were synthesized using the same method as that of 112-$NiCo_2O_4$ but adjusting initial feed molar ratios of Ni and Co salts. Through EDS analysis (Figure S3.5), the corresponding bulk compositions of 112-$Ni_xCo_{3-x}O_4$, at the initial feed Ni: Co molar ratios of 0, 0.2 and 1.0, are determined to be Co_3O_4, $Ni_{0.5}Co_{2.5}O_4$ and $Ni_{1.3}Co_{1.7}O_4$ (labeled as 112-Co_3O_4, 112-$Ni_{0.5}Co_{2.5}O_4$ and 112-$Ni_{1.3}Co_{1.7}O_4$) with details summarized in Table 3.1. Notably, at a high Ni feed ($x > 1$), the obtained sample cannot reach its theoretical composition of $Ni_{1.5}Co_{1.5}O_4$, since Ni incorporation requires extra energy[43]. The XRD patterns (Figure 3.6a) of 112-Co_3O_4, 112-$Ni_{0.5}Co_{2.5}O_4$, 112-$NiCo_2O_4$ and 112-$Ni_{1.3}Co_{1.7}O_4$ reveal that all samples can be indexed to the spinel phase $NiCo_2O_4$, confirming Ni incorporation does not fundamentally alter the crystal structure from the stoichiometric $NiCo_2O_4$. The calculated lattice constant *a* increases from 8.0850 Å to 8.1147 Å as Ni^{3+} increases (Table 3.1), which confirms the presence of Ni^{3+} in the octahedral sites of spinel crystal structures[44]. Finally, the SEM images (Figure S3.6) of 112-Co_3O_4, 112-$Ni_{0.5}Co_{2.5}O_4$ and 112-$Ni_{1.3}Co_{1.7}O_4$ nanoplates illustrate the thin and hexagonal morphologies that resemble the 112-$NiCo_2O_4$ nanoplates.

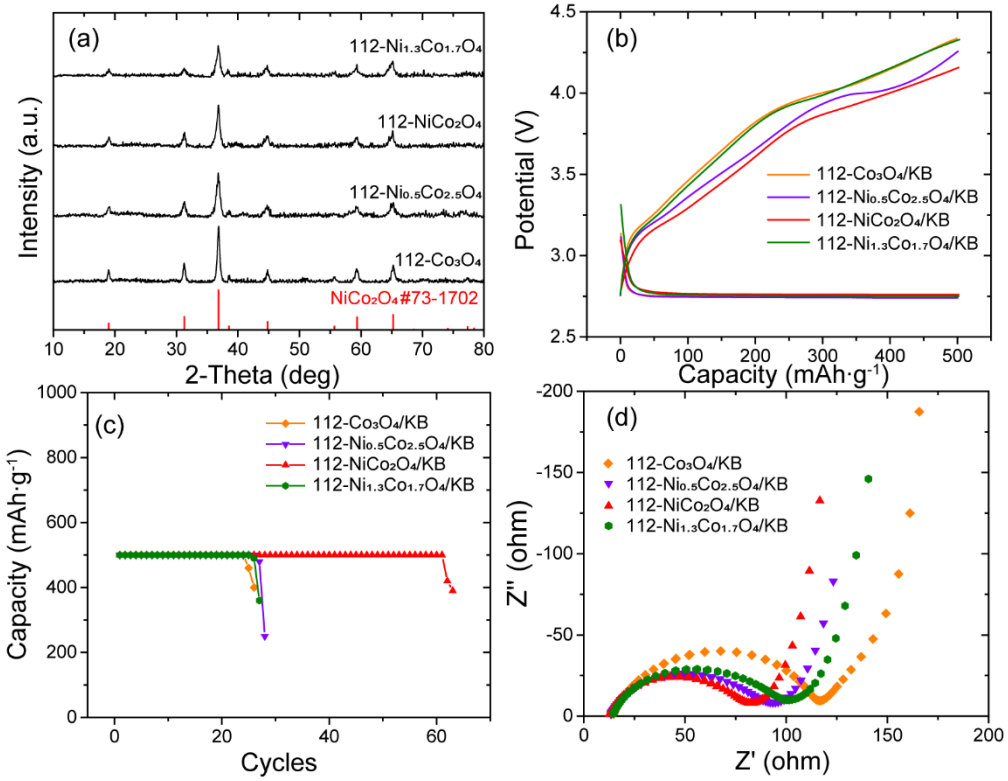

Figure 3.6. (a) The XRD patterns of 112-Co_3O_4, 112-$Ni_{0.5}Co_{2.5}O_4$, 112-$NiCo_2O_4$ and 112-$Ni_{1.3}Co_{1.7}O_4$; (b) a comparison on the first cycle curves of 112-Co_3O_4/KB, 112-$Ni_{0.5}Co_{2.5}O_4$/KB, 112-$NiCo_2O_4$/KB and 112-$Ni_{1.3}Co_{1.7}O_4$/KB cathodes at 200 mA g^{-1} and limit capacity of 500 mAh g^{-1}; (c) a summary of the cycling performance of corresponding cathodes; (d) EIS spectra of corresponding pristine cathodes.

Table 3.1. The compositions and crystal parameters of various 112-$Ni_xCo_{3-x}O_4$

Feed ratio (Ni: Co)	Theoretical composition	Experimental composition [a]	Lattice constant (Å) [b]
0	Co_3O_4	Co_3O_4	8.0810
0.2	$Ni_{0.5}Co_{2.5}O_4$	$Ni_{0.5}Co_{2.5}O_4$	8.0850
0.5	$Ni_{1.0}Co_{2.0}O_4$	$Ni_{1.0}Co_{2.0}O_4$	8.0978
1.0	$Ni_{1.5}Co_{1.5}O_4$	$Ni_{1.3}Co_{1.7}O_4$	8.1147

[a] Calculated based on the results of EDS

[b] Calculated from the d-spacings of the (3 1 1) plane

Figure 3.6b compares the first cycle curves of the 112-Co_3O_4/KB, 112-$Ni_{0.5}Co_{2.5}O_4$/KB, 112-$NiCo_2O_4$/KB and 112-$Ni_{1.3}Co_{1.7}O_4$/KB cathodes cycled at 200 mA g^{-1} and limited capacity of 500 mAh g^{-1}. 112-$NiCo_2O_4$/KB displays the lowest charge potential, followed by 112-$Ni_{0.5}Co_{2.5}O_4$/KB, 112-$Ni_{1.3}Co_{1.7}O_4$/KB and finally 112-Co_3O_4/KB. In the range of $x \leq 1$, the charge potentials of 112-$Ni_xCo_{3-x}O_4$/KB cathodes decrease with increasing x. However, when the Ni^{3+} content increases further to 112-$Ni_{1.3}Co_{1.7}O_4$/KB, the charge potential increases significantly. The overall cyclabilities also increases from 24 cycles for 112-Co_3O_4/KB to a peak of 61 cycles for 112-$NiCo_2O_4$/KB and declines to 25 cycles for 112-$Ni_{1.3}Co_{1.7}O_4$/KB (Figure 3.6c, detailed profiles of each cathode are shown in Figure S3.7). The charge transport properties of the cathodes were further characterized by EIS. Figure 3.6d shows the Nyquist plots of the pristine cathodes. The charge-transfer resistance (R_{ct}) was measured from the radius of the semicircles at the high-frequency region. The R_{ct} values for 112-Co_3O_4/KB, 112-$Ni_{0.5}Co_{2.5}O_4$/KB, 112-$NiCo_2O_4$/KB and 112-$Ni_{1.3}Co_{1.7}O_4$/KB are 103.2, 71.0, 63.7 and 78.3 Ω. The R_{ct} results are in alignment with the conductance of bulk $Ni_xCo_{3-x}O_4$ being previously reported[45]. The presence of Ni^{3+} in the crystal lattice of 112-$Ni_xCo_{3-x}O_4$ drastically improves their conductance, however, if the Ni^{3+} content is higher than $x > 1$, a poorly conductive NiO phase tends to form, which can reduce the overall conductance significantly[45]. The NiO phase in 112-$Ni_{1.3}Co_{1.7}O_4$ can be observed in its FTIR spectrum (Figure S3.8), the broad peak at 470 cm^{-1} indicates a poorly crystallized NiO phase that is undetectable in XRD. Based on the above analysis, the charge potentials and cycling performances are also governed by the conductance of the 112-$Ni_xCo_{3-x}O_4$. The superior cycling performance of 112-$NiCo_2O_4$/KB can be further attributed to the high conductance of 112-$NiCo_2O_4$.

Conclusion

For the first time various $NiCo_2O_4$ nanoplates with identical morphologies but different {111} and {112} crystal planes were synthesized as model transition metal oxide cathodes for non-aqueous Li-O_2 batteries. The contribution of $NiCo_2O_4$ to Li-O_2 battery performance mainly comes from enhancing OER activity rather than ORR. The {112} crystal planes exhibit superior OER activity than the {111} crystal planes, owing to the presence of numerous dangling bonds on crystal surfaces to expose highly active $Co^{3+}(O_h)$ and $Ni^{3+}(O_h)$ sites. Large surface areas associated with the highly active {112} crystal planes can further contribute to the OER activity of the battery. The presence of Ni^{3+} plays an essential role in improving the OER activity and the overall conductance of $Ni_xCo_{3-x}O_4$. The {112} crystal planes exposed $NiCo_2O_4$ nanoplates can be employed as an effective electrochemical catalyst for non-aqueous Li-O_2 battery, owing to the high activity of Ni^{3+}, highly active {112} crystal planes, large surface areas and good conductance. This study has demonstrated the correlation between nanostructures and electrochemical performance of $NiCo_2O_4$ as model transition metal oxide cathodic materials in non-aqueous Li-O_2 batteries. These results provide a new possible strategy to improve the electrocatalytic activity of $NiCo_2O_4$, such as through the selective exposure of Ni^{3+} active sites on the electrocatalyst surfaces, for the development of high-performance transition metal oxide electrocatalysts in diverse sustainable energy applications.

Associated Content

Supporting Information.

SEM images of 111-$NiCo_2O_4$ and 112-$NiCo_2O_4$ precursors, 112-$NiCo_2O_4$/KB cathode at different discharge and charge states, 112-Co_3O_4, 112-$Ni_{0.5}Co_{2.5}O_4$ and 112-$Ni_{1.3}Co_{1.7}O_4$ nanoplates; TEM image of 112-$NiCo_2O_4$-400C; FTIR spectra of 112-$Ni_{0.5}Co_{2.5}O_4$, 112-$NiCo_2O_4$ and 112-$Ni_{1.3}Co_{1.7}O_4$; EDS analysis of 112-Co_3O_4, 112-$Ni_{0.5}Co_{2.5}O_4$, 112-$NiCo_2O_4$ and 112-$Ni_{1.3}Co_{1.7}O_4$; the cycling performance of 112-$NiCo_2O_4$-400C/KB, 112-Co_3O_4/KB, 112-$Ni_{0.5}Co_{2.5}O_4$/KB and 112-$Ni_{1.3}Co_{1.7}O_4$/KB cathodes.

Acknowledgments

This work was financially supported by the Australian Research Council Discovery Projects DP140104062.

References

(1) Lu, J.; Li, L.; Park, J.-B.; Sun, Y.-K.; Wu, F.; Amine, K. Aprotic and Aqueous Li-O_2 Batteries. *Chem. Rev.* **2014**, *114* (11), 5611–5640.

(2) Li, F.; Zhang, T.; Zhou, H. Challenges of Non-Aqueous Li-O_2 Batteries: Electrolytes, Catalysts, and Anodes. *Energy Environ. Sci.* **2013**, *6* (4), 1125–1141.

(3) Ma, Z.; Yuan, X.; Li, L.; Ma, Z.-F.; Wilkinson, D. P.; Zhang, L.; Zhang, J. A Review of Cathode Materials and Structures for Rechargeable Lithium-Air Batteries. *Energy Environ. Sci.* **2015**, *8* (8), 2144–2198.

(4) Ye, L.; Lv, W.; Cui, J.; Liang, Y.; Wu, P.; Wang, X.; He, H.; Lin, S.; Wang, W.; Dickerson, J. H.; et al. Lithium-Air Batteries: Performance Interplays with Instability Factors. *Chemelectrochem* **2015**, *2* (3), 312–323.

(5) Shao, Y.; Ding, F.; Xiao, J.; Zhang, J.; Xu, W.; Park, S.; Zhang, J. G.; Wang, Y.; Liu, J. Making Li-Air Batteries Rechargeable: Material Challenges. *Adv. Funct. Mater.* **2013**, *23* (8), 987–1004.

(6) Yang, Y.; Liu, W.; Wang, Y.; Wang, X.; Xiao, L.; Lu, J.; Lin Zhuang. A PtRu Catalyzed Rechargeable Oxygen Electrode for Li-O_2 Batteries: Performance

Improvement Through Li_2O_2 Morphology Control. *Phys. Chem. Chem. Phys.* **2014**, *16* (38), 20618–20623.

(7) Leng, L.; Zeng, X.; Song, H.; Shu, T.; Wang, H.; Liao, S. Pd Nanoparticles Decorating Flower-Like Co_3O_4 Nanowire Clusters to Form an Efficient, Carbon/Binder-Free Cathode for Li-O_2 Batteries. *J. Mater. Chem. A* **2015**, *3* (30), 15626–15632.

(8) Ni, W.; Liu, S.; Fei, Y.; He, Y.; Ma, X.; Lu, L.; Deng, Y. Preparation of Carbon Nanotubes/Manganese Dioxide Composite Catalyst with Fewer Oxygen-Containing Groups for Li-O_2 Batteries Using Polymerized Ionic Liquids as Sacrifice Agent. *ACS Appl. Mater. Interfaces* **2017**, *9* (17), 14749–14757.

(9) Shang, C.; Zhang, X.; Shui, L.; Chen, Z.; Liao, H.; Li, M.; Wang, X.; Zhou, G. Fe_3O_4@CoO Mesospheres with Core-Shell Nanostructure as Catalyst for Li-O_2 Batteries. *Appl. Surf. Sci.* **2018**, *457*, 804–808.

(10) Chen, S.; Liu, G.; Yadegari, H.; Wang, H.; Qiao, S. Z. Three-Dimensional MnO_2 Ultrathin Nanosheet Aerogels for High-Performance Li-O_2 Batteries. *J. Mater. Chem. A* **2015**, *3* (6), 2559–2563.

(11) Tu, F.; Xie, J.; Zhang, S.; Cao, G.; Zhu, T.; Zhao, X. Mushroom-Like Au/$NiCo_2O_4$ Nanohybrids as High-Performance Binder-Free Catalytic Cathodes for Lithium-Oxygen Batteries. *J. Mater. Chem. A* **2015**, *3* (10), 5714–5721.

(12) Yao, X.; Dong, Q.; Cheng, Q.; Wang, D. Li-Oxygen Battery: Parasitic Reactions. In *Metal-Air Batteries*; Zhang, X., Ed.; Wiley-VCH Verlag GmbH & Co. KGaA: Weinheim, Germany, 2018; pp 95–124.

(13) Liu, L.; Jiang, Z.; Fang, L.; Xu, H.; Zhang, H.; Gu, X.; Wang, Y. Probing the Crystal Plane Effect of Co_3O_4 for Enhanced Electrocatalytic Performance toward Efficient Overall Water Splitting. *ACS Appl. Mater. Interfaces* **2017**, *9* (33), 27736–27744.

(14) Xu, Z.-N.; Sun, J.; Lin, C.-S.; Jiang, X.-M.; Chen, Q.-S.; Peng, S.-Y.; Wang, M.-S.; Guo, G.-C. High-Performance and Long-Lived Pd Nanocatalyst Directed by Shape Effect for CO Oxidative Coupling to Dimethyl Oxalate. *ACS Catal.* **2013**, *3* (2), 118–122.

(15) Si, R.; Flytzani-Stephanopoulos, M. Shape and Crystal-Plane Effects of Nanoscale Ceria on the Activity of Au-CeO_2 Catalysts for the Water-Gas Shift Reaction. *Angew. Chem. Int. Ed.* **2008**, *47* (15), 2884–2887.

(16) Liu, L.; Gu, X.; Cao, Y.; Yao, X.; Zhang, L.; Tang, C.; Gao, F.; Dong, L. Crystal-Plane Effects on the Catalytic Properties of Au/TiO_2. *ACS Catal.* **2013**, *3* (12), 2768–2775.

(17) Song, K.; Cho, E.; Kang, Y.-M. Morphology and Active-Site Engineering for Stable Round-Trip Efficiency Li-O_2 Batteries: A Search for the Most Active Catalytic Site in Co_3O_4. *ACS Catal.* **2015**, *5* (9), 5116–5122.

(18) Gao, R.; Zhu, J.; Xiao, X.; Hu, Z.; Liu, J.; Liu, X. Facet-Dependent Electrocatalytic Performance of Co_3O_4 for Rechargeable Li-O_2 Battery. *J. Phys. Chem. C* **2015**, *119* (9), 4516–4523.

(19) Mu, J.; Zhang, L.; Zhao, G.; Wang, Y. The Crystal Plane Effect on the Peroxidase-Like Catalytic Properties of Co_3O_4 Nanomaterials. *Phys. Chem. Chem. Phys.* **2014**, *16* (29), 15709–15716.

(20) Su, D.; Dou, S.; Wang, G. Single Crystalline Co_3O_4 Nanocrystals Exposed with Different Crystal Planes for Li-O_2 Batteries. *Sci. Rep.* **2014**, *4*, 5767.

(21) Xiao, X.; Liu, X.; Zhao, H.; Chen, D.; Liu, F.; Xiang, J.; Hu, Z.; Li, Y. Facile Shape Control of Co_3O_4 and the Effect of the Crystal Plane on Electrochemical Performance. *Adv. Mater.* **2012**, *24* (42), 5762–5766.

(22) Du, J.; Zhou, G.; Zhang, H.; Cheng, C.; Ma, J.; Wei, W.; Chen, L.; Wang, T. Ultrathin Porous $NiCo_2O_4$ Nanosheet Arrays on Flexible Carbon Fabric for High-Performance Supercapacitors. *ACS Appl. Mater. Interfaces* **2013**, *5* (15), 7405–7409.

(23) Zhang, G.; Lou, X. W. (David). General Solution Growth of Mesoporous $NiCo_2O_4$ Nanosheets on Various Conductive Substrates as High-Performance Electrodes for Supercapacitors. *Adv. Mater.* **2013**, *25* (7), 976–979.

(24) Sun, Y.; Zuo, X.; Xu, D.; Sun, D.; Zhang, X.; Zeng, S. Flower-like $NiCo_2O_4$ Microstructures as Promising Anode Material for High Performance Lithium-Ion Batteries: Facile Synthesis and Its Lithium Storage Properties. *ChemistrySelect* **2016**, *1* (16), 5129–5136.

(25) Li, J.; Xiong, S.; Liu, Y.; Ju, Z.; Qian, Y. High Electrochemical Performance of Monodisperse $NiCo_2O_4$ Mesoporous Microspheres as an Anode Material for Li-Ion Batteries. *ACS Appl. Mater. Interfaces* **2013**, *5* (3), 981–988.

(26) Tong, X.; Chen, S.; Guo, C.; Xia, X.; Guo, X.-Y. Mesoporous $NiCo_2O_4$ Nanoplates on Three-Dimensional Graphene Foam as an Efficient Electrocatalyst for the Oxygen Reduction Reaction. *ACS Appl. Mater. Interfaces* **2016**, *8* (42), 28274–28282.

(27) Lee, D. U.; Kim, B. J.; Chen, Z. One-Pot Synthesis of a Mesoporous $NiCo_2O_4$ Nanoplatelet and Graphene Hybrid and Its Oxygen Reduction and Evolution Activities as an Efficient Bi-Functional Electrocatalyst. *J. Mater. Chem. A* **2013**, *1* (15), 4754–4762.

(28) Wu, Z.; Zhu, Y.; Ji, X. $NiCo_2O_4$-Based Materials for Electrochemical Supercapacitors. *J. Mater. Chem. A* **2014**, *2* (36), 14759–14772.

(29) Gong, H.; Xue, H.; Wang, T.; Guo, H.; Fan, X.; Song, L.; Xia, W.; He, J. High-Loading Nickel Cobaltate Nanoparticles Anchored on Three-Dimensional N-Doped Graphene as an Efficient Bifunctional Catalyst for Lithium-Oxygen Batteries. *ACS Appl. Mater. Interfaces* **2016**, *8* (28), 18060–18068.

(30) Mohamed, S. G.; Tsai, Y.-Q.; Chen, C.-J.; Tsai, Y.-T.; Hung, T.-F.; Chang, W.-S.; Liu, R.-S. Ternary Spinel MCo_2O_4 (M = Mn, Fe, Ni, and Zn) Porous Nanorods as Bifunctional Cathode Materials for Lithium-O_2 Batteries. *ACS Appl. Mater. Interfaces* **2015**, *7* (22), 12038–12046.

(31) Li, L.; Shen, L.; Nie, P.; Pang, G.; Wang, J.; Li, H.; Dong, S.; Zhang, X. Porous $NiCo_2O_4$ Nanotubes as a Noble-Metal-Free Effective Bifunctional Catalyst for Rechargeable Li-O_2 Batteries. *J. Mater. Chem. A* **2015**, *3* (48), 24309–24314.

(32) Zhang, L.; Zhang, S.; Zhang, K.; Xu, G.; He, X.; Dong, S.; Liu, Z.; Huang, C.; Gu, L.; Cui, G. Mesoporous $NiCo_2O_4$ Nanoflakes as Electrocatalysts for Rechargeable Li-O_2 Batteries. *Chem. Commun.* **2013**, *49* (34), 3540–3542.

(33) Sun, B.; Huang, X.; Chen, S.; Zhao, Y.; Zhang, J.; Munroe, P.; Wang, G. Hierarchical Macroporous/Mesoporous $NiCo_2O_4$ Nanosheets as Cathode Catalysts for Rechargeable Li-O_2 Batteries. *J. Mater. Chem. A* **2014**, *2* (30), 12053–12059.

(34) Mei, J.; Liao, T.; Kou, L.; Sun, Z. Two-Dimensional Metal Oxide Nanomaterials for Next-Generation Rechargeable Batteries. *Adv. Mater.* **2017**, *29* (48), 1700176.

(35) Galiote, N. A.; Jeong, S.; Morais, W. G.; Passerini, S.; Huguenin, F. The Role of Ionic Liquid in Oxygen Reduction Reaction for Lithium-Air Batteries. *Electrochim. Acta* **2017**, *247*, 610–616.

(36) Lin, X.; Su, J.; Li, L.; Yu, A. Hierarchical Porous $NiCo_2O_4$@Ni as Carbon-Free Electrodes for Lithium-Oxygen Batteries. *Electrochim. Acta* **2015**, *168*, 292–299.

(37) Shen, C.; Wen, Z.; Wang, F.; Rui, K.; Lu, Y.; Wu, X. Wave-Like Free-Standing $NiCo_2O_4$ Cathode for Lithium-Oxygen Battery with High Discharge Capacity. *J. Power Sources* **2015**, *294*, 593–601.

(38) Ma, L.; Yu, T.; Tzoganakis, E.; Amine, K.; Wu, T.; Chen, Z.; Lu, J. Fundamental Understanding and Material Challenges in Rechargeable Nonaqueous Li-O_2 Batteries: Recent Progress and Perspective. *Adv. Energy Mater.* **2018**, *8* (22), 1800348.

(39) Gao, C.; Meng, Q.; Zhao, K.; Yin, H.; Wang, D.; Guo, J.; Zhao, S.; Chang, L.; He, M.; Li, Q.; et al. Co_3O_4 Hexagonal Platelets with Controllable Facets Enabling Highly Efficient Visible-Light Photocatalytic Reduction of CO_2. *Adv. Mater.* **2016**, *28* (30), 6485–6490.

(40) Ma, F.; Xu, K.-W. Using Dangling Bond Density to Characterize the Surface Energy of Nanomaterials. *Surf. Interface Anal.* **2007**, *39* (7), 611–614.

(41) Zasada, F.; Gryboś, J.; Indyka, P.; Piskorz, W.; Kaczmarczyk, J.; Sojka, Z. Surface Structure and Morphology of M[CoM′]O_4 (M = Mg, Zn, Fe, Co and M′ = Ni, Al, Mn, Co) Spinel Nanocrystals—DFT+U and TEM Screening Investigations. *J. Phys. Chem. C* **2014**, *118* (33), 19085–19097.

(42) Shi, X.; Bernasek, S. L.; Selloni, A. Oxygen Deficiency and Reactivity of Spinel $NiCo_2O_4$ (001) Surfaces. *J. Phys. Chem. C* **2017**, *121* (7), 3929–3937.

(43) Shi, X.; Bernasek, S. L.; Selloni, A. Formation, Electronic Structure, and Defects of Ni Substituted Spinel Cobalt Oxide: A DFT+U Study. *J. Phys. Chem. C* **2016**, *120* (27), 14892–14898.

(44) Yu. E. Roginskaya; O. V. Morozova; E. N. Lubnin; Yu. E. Ulitina; G. V. Lopukhova; S. Trasatti. Characterization of Bulk and Surface Composition of $Co_xNi_{1-x}O_y$ Mixed Oxides for Electrocatalysis. *Langmuir* **1997**, *13* (17), 4621–4627.

(45) Lapham, D. P.; Tseung, A. C. C. The Effect of Firing Temperature, Preparation Technique and Composition on the Electrical Properties of the Nickel Cobalt Oxide Series $Ni_xCo_{1-x}O_y$. *J. Mater. Sci.* **2004**, *39*, 251–264.

Table of Content

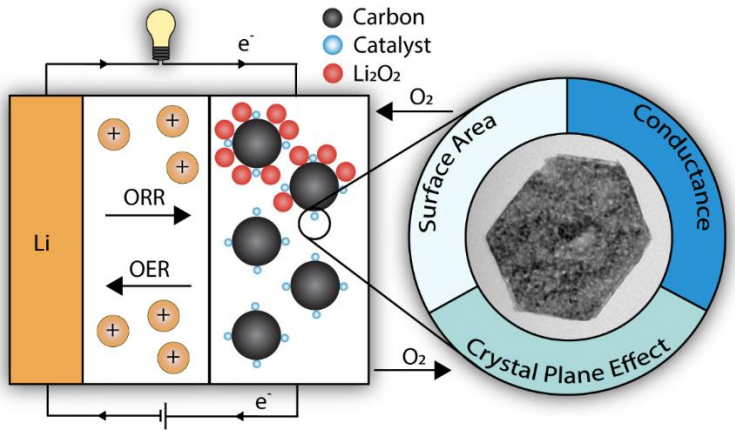

Supporting Information

Improving Non-Aqueous Li-O_2 Battery Performance by Tuning Cathodic $NiCo_2O_4$ Nanostructures

Heng Wang,[†] Qi Bi,[†] Haihui Wang,[*,†,‡] Sheng Dai [*,†,§]

† School of Chemical Engineering and Advanced Materials, The University of Adelaide, Adelaide, South Australia 5005, Australia

‡ School of Chemistry & Chemical Engineering, South China University of Technology, 381 Wushan Road, Guangzhou 510640, China

§ Department of Chemical Engineering, Brunel University London, Uxbridge, UB8 3PH, United Kingdom

Corresponding author

*E-mail: hhwang@scut.edu.cn

*E-mail: s.dai@adelaide.edu.au

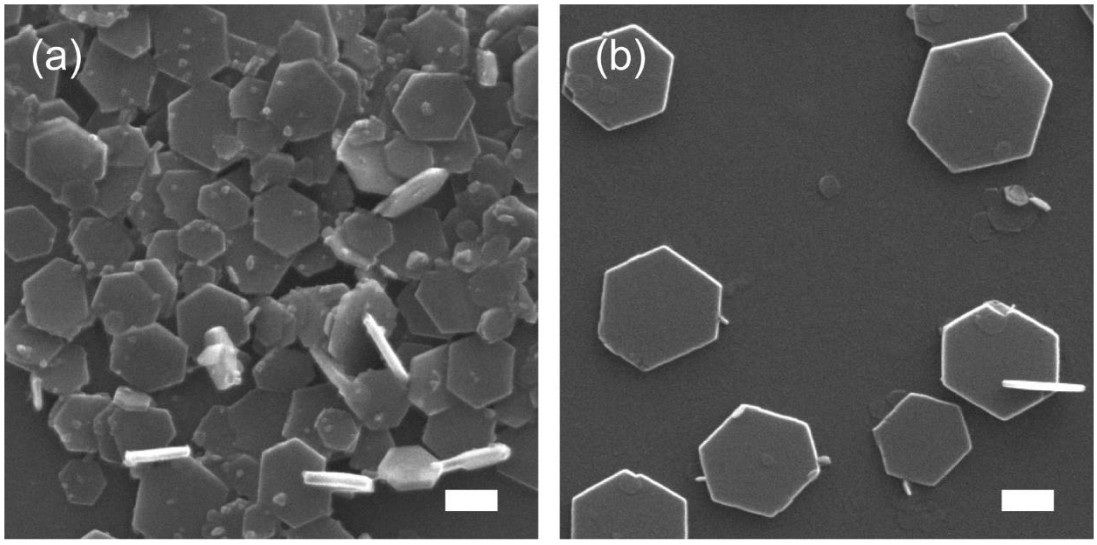

Figure S3.1. SEM images of (a) 111-$NiCo_2O_4$ precursor and (b) 112-$NiCo_2O_4$ precursor. Scale bars indicate 200 nm.

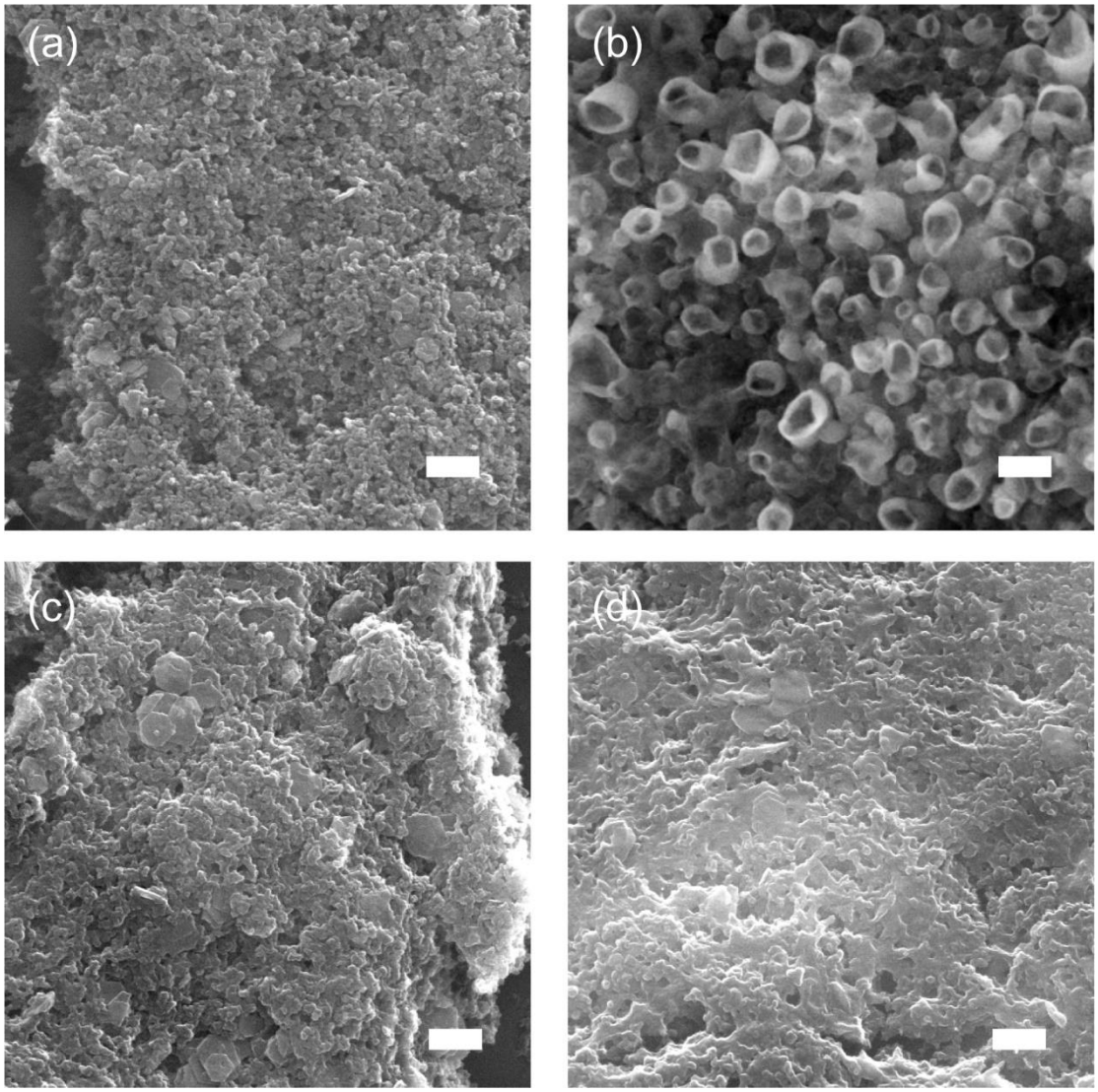

Figure S3.2. SEM images of (a) a typical pristine 112-$NiCo_2O_4$/KB cathode, (b) a cathode discharged to 2.0 V, (c) a cathode after cycled for 50 cycles, (d) a cathode after cycled for 61 cycles. Scale bars indicate 500 nm.

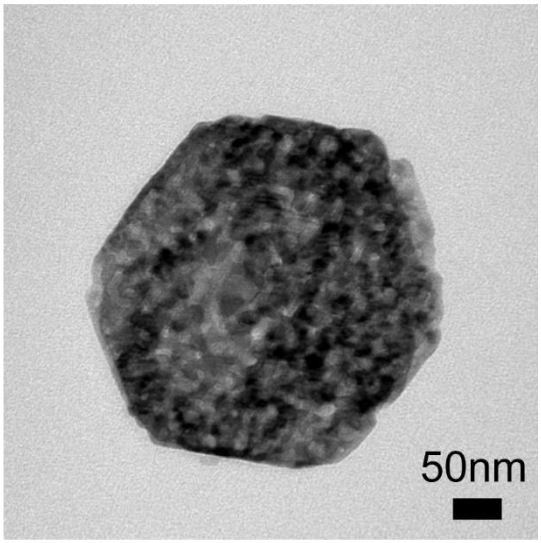

Figure S3.3. A TEM image of 112-$NiCo_2O_4$-400C.

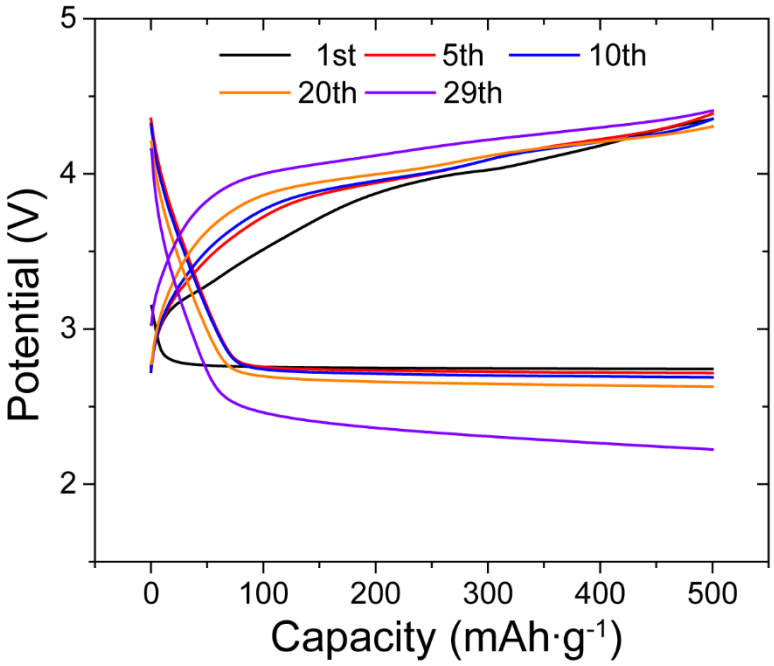

Figure S3.4. Detailed cycling performance of the 112-$NiCo_2O_4$-400C/KB cathode at a current density of 200 mA g^{-1} and limit capacity of 500 mAh g^{-1}.

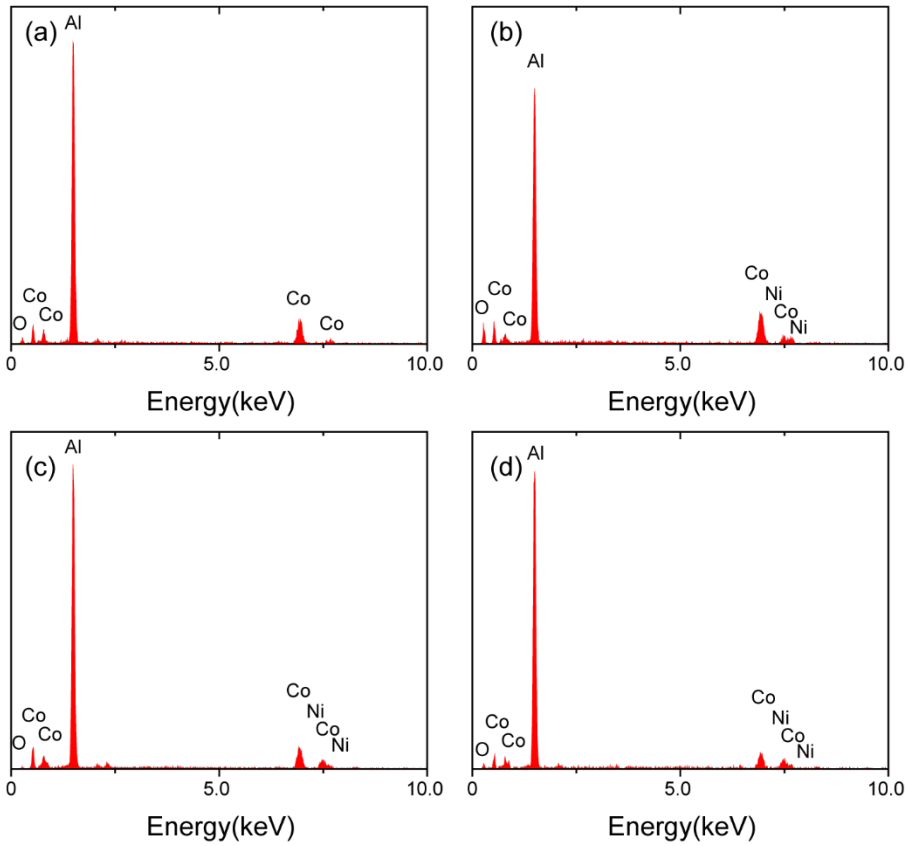

Figure S3.5. EDS analysis of (a) 112-Co_3O_4, (b) 112-$Ni_{0.5}Co_{2.5}O_4$, (c) 112-$NiCo_2O_4$ and (d) 112-$Ni_{1.3}Co_{1.7}O_4$.

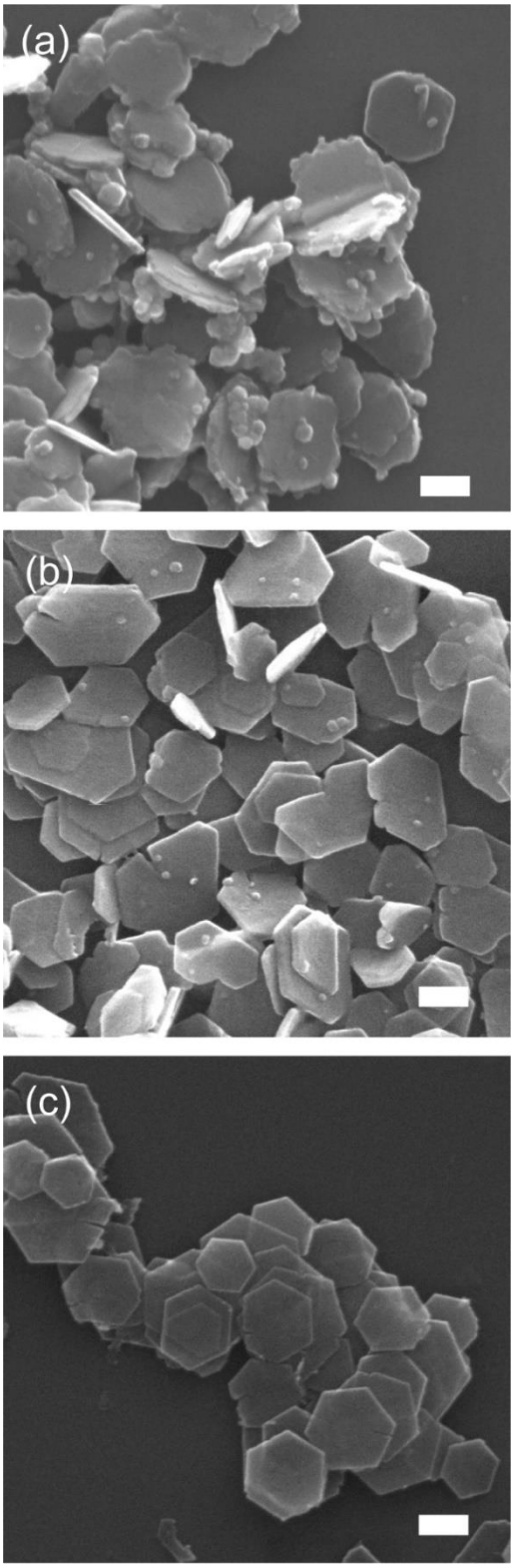

Figure S3.6. SEM images of (a) 112-Co_3O_4, (b) 112-$Ni_{0.5}Co_{2.5}O_4$ and (c) 112-$Ni_{1.3}Co_{1.7}O_4$. The scale bars indicate 200 nm.

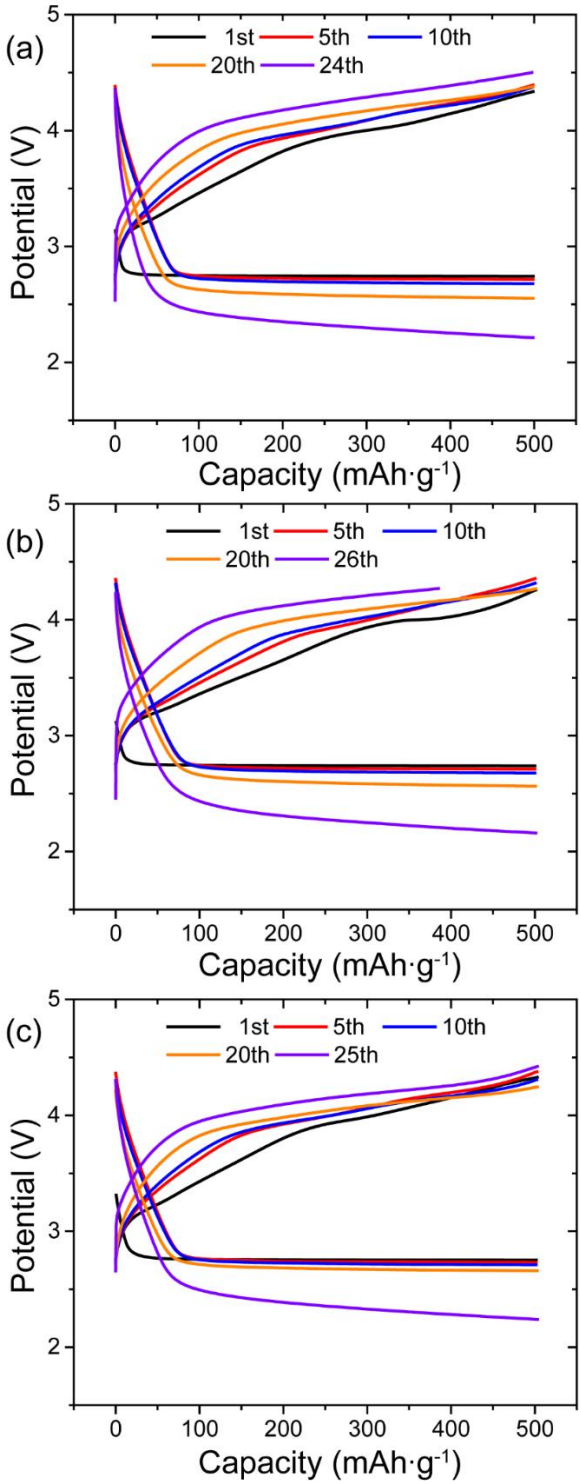

Figure S3.7. Detailed cycling performance of (a) 112-Co_3O_4/KB, (b) 112-$Ni_{0.5}Co_{2.5}O_4$/KB and (c) 112-$Ni_{1.3}Co_{1.7}O_4$/KB cathodes at a current density of 200 mA g^{-1} and limit capacity of 500 mAh g^{-1}.

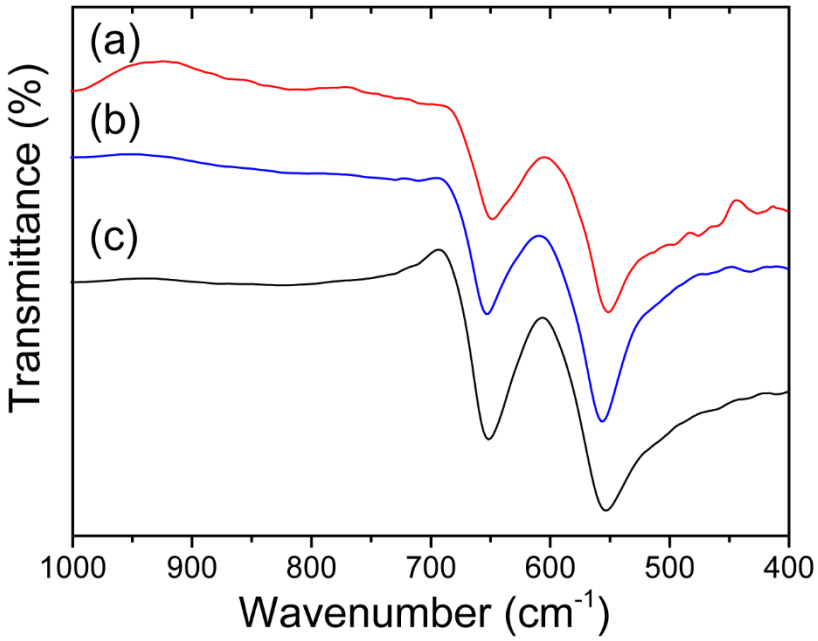

Figure S3.8. FTIR spectra of (a) 112-$Ni_{1.3}Co_{1.7}O_4$, (b) 112-$NiCo_2O_4$ and (c) 112-$Ni_{0.5}Co_{2.5}O_4$. Peaks at ~560 and 650 cm^{-1} in all samples are the typical M-O (M = Ni & CO) vibration bands. The board peak at 470 cm^{-1} in 112-$Ni_{1.3}Co_{1.7}O_4$ can be ascribed to a poorly crystallized NiO, which cannot detectable by XRD.

Chapter 4 Macroporous Nanocomposites of Reduced Graphene Oxide Aerogels and $NiCo_2O_4$ Nanoplates for Non-Aqueous Li-O_2 Battery

4.1. Introduction and Significance

$NiCo_2O_4$ materials are effective electrocatalyst for non-aqueous Li-O_2 batteries, but their relatively low conductivity hinders the improvement of battery performance. Reduced graphene oxide aerogels are highly conductive and possess macropores to accommodate the discharge product but show low electrochemical activity and are suspect to attack from superoxide and peroxide species during electrochemistry. In this work, the synergistic effect between $NiCo_2O_4$ and reduced graphene oxide aerogels is explored through the investigation of a series of nanocomposites of both materials. This work demonstrates a novel strategy to use catalyst as a protective layer for carbon support to enhance the performance of carbon-based macroporous cathode to efficient accommodate Li_2O_2 formed via the solution growth pathway. The highlights of this work include:

1. A series of novel nanocomposites of reduced graphene oxide aerogels and $NiCo_2O_4$ nanoplates were synthesized through a robust one-pot approach.
2. The synergistic effect between $NiCo_2O_4$ and reduced graphene oxide aerogels was found to be regulated by the balance of $NiCo_2O_4$ coverage on walls of macropores and overall cathode conductivity.
3. The dual roles of $NiCo_2O_4$ as both electrocatalyst and protective layer for reduced graphene oxide aerogel were attributed to the excellent battery cycling performance.
4. The freestanding macroporous structure of the cathode also played an essential role in the cyclability of the battery by promoting mass transportation and avoiding binders.

4.2. Macroporous Nanocomposites of Reduced Graphene Oxide Aerogels and $NiCo_2O_4$ Nanoplates for Non-Aqueous Li-O_2 Battery

This section is included as an unsubmitted manuscript by Heng Wang, Qi Bi, Haihui Wang, Sheng Dai, Macroporous Nanocomposites of Reduced Graphene Oxide Aerogels and $NiCo_2O_4$ Nanoplates for Non-Aqueous Li-O_2 Battery.

Statement of Authorship

Title of Paper	Macroporous Nanocomposites of Reduced Graphene Oxide Aerogels and $NiCo_2O_4$ Nanoplates for Non-aqueous Li-O_2 Battery
Publication Status	☐ Published ☐ Accepted for Publication ☐ Submitted for Publication ☑ Unpublished and Unsubmitted work written in manuscript style
Publication Details	To be submitted

Principal Author

Name of Principal Author (Candidate)	Heng Wang
Contribution to the Paper	Research plan, material synthesis, material characterization, battery performance evaluation, data analysis, and manuscript drafting and editing.
Overall percentage (%)	85%
Certification:	This paper reports on original research I conducted during the period of my Higher Degree by Research candidature and is not subject to any obligations or contractual agreements with a third party that would constrain its inclusion in this thesis. I am the primary author of this paper.
Signature	Date 30/04/2019

Co-Author Contributions

By signing the Statement of Authorship, each author certifies that:

i. the candidate's stated contribution to the publication is accurate (as detailed above);

ii. permission is granted for the candidate in include the publication in the thesis; and

iii. the sum of all co-author contributions is equal to 100% less the candidate's stated contribution.

Name of Co-Author	Qi Bi
Contribution to the Paper	Discussion of research plan
Signature	Date 02/05/2019

Name of Co-Author	Prof. Haihui Wang
Contribution to the Paper	Help to evaluate and edit manuscript
Signature	Date 30/04/2019

Name of Co-Author	Prof. Sheng Dai
Contribution to the Paper	Supervision for the development of work and manuscript evaluation
Signature	Date 30 April 2019

Please cut and paste additional co-author panels here as required.

Macroporous Nanocomposites of Reduced Graphene Oxide Aerogels and $NiCo_2O_4$ Nanoplates for Non-Aqueous Li-O_2 Battery

Heng Wang,[†] Qi Bi,[†] Haihui Wang,[*,†,‡] Sheng Dai[*,†,§]

† School of Chemical Engineering and Advanced Materials, the University of Adelaide, Adelaide, South Australia 5005, Australia

‡ School of Chemistry & Chemical Engineering, South China University of Technology, 381 Wushan Road, Guangzhou 510640, China

§ Department of Chemical Engineering, Brunel University London, Uxbridge, UB8 3PH, United Kingdom

Corresponding author

*E-mail: hhwang@scut.edu.cn

*E-mail: s.dai@adelaide.edu.au

Abstract

Owing to their exceptional specific high capacities, non-aqueous Li-O_2 batteries have become increasingly attractive in energy storage applications. The nanostructures of porous cathode materials strongly influence overall battery performance. In this study, a novel freestanding cathode has been developed by hybridizing $NiCo_2O_4$ (NCO) nanoplates on macroporous reduced graphene oxide aerogel (GA) support through a self-assembly approach. The resulting cathode features a unique nanostructure in which the walls of GA macropores are covered by NCO nanoplates, providing abundant active sites toward the electrochemical reactions as well as acting a protective layer against the corrosion of GA support. In addition, macroporous GA support facilitates the mass and electron transportation as well as act as accommodation sites for Li_2O_2 discharge product. After systematic optimization, the nanocomposite with a GA: NCO weight ratio of 1: 4 displays the optimal conductance and NCO coverage on the walls of macropores, resulting in a capacity of 4302 mAh g^{-1} and a cyclability of 82 cycles. This study has demonstrated the synergistic effect between the electrocatalysts and their supports, which provides insights into the rational cathode design for future high-performance Li-O_2 batteries.

Keywords: non-aqueous Li-O_2 battery, freestanding, cathode, macroporous, reduced graphene oxide aerogel, $NiCo_2O_4$

Introduction

Non-aqueous Li-O_2 batteries have attracted tremendous attention in recent years as a promising energy storage technology especially for electric vehicles, owing to their exceptionally high specific energy (~3600 W h kg^{-1})[1–3]. In a typical non-aqueous Li-O_2 system, O_2 is reduced at the cathode during the discharging process through an oxygen reduction reaction (ORR) and combines Li^+ to form Li_2O_2, which is insoluble in electrolyte and deposited on cathode surfaces. During the charging process, the deposited Li_2O_2 is decomposed in an oxygen evolution reaction (OER) associated with O_2 release. However, non-aqueous Li-O_2 system faces numerous challenges, such as high polarization, low round-trip efficiency and poor overall stability[4], which hinder its end-use applications. To overcome these issues, numerous efforts have been devoted to developing various cathodes that are highly active towards OER and ORR as well as able to accommodate solid Li_2O_2 discharge product effectively.

$NiCo_2O_4$ (NCO) has been studied extensively in the fields of supercapacitors[5,6], lithium-ion batteries[7,8] and water splitting[9,10] applications due to its relatively high electrical conductivity among metal oxides[5], rich oxygen vacancies[11] and high electrocatalytic activity[12]. More importantly, NCO has a rich variety of nanostructures that can be carefully tailored for non-aqueous Li-O_2 batteries. Recently, numerous NCO materials, ranging from zero-dimensional nanoparticles to three-dimensional nanoflowers[13–17], have been proposed as cathode materials for non-aqueous Li-O_2 batteries. The lower dimensional NCO materials are generally utilized as effective electrocatalysts in conjunction with commercial carbon as support, while three-dimensional NCO materials can be directly used as freestanding and binder-free cathodes with improved stability. Although freestanding NCO cathodes can

improve long-term stability[18] of the battery, they often exhibit low specific capacities (< 1500 mAh g^{-1})[19,20], due to its heavy weight, limited conductivity (compared to carbon) and low surface areas. Carbon materials, on the other hand, are light-weight, highly conductive and porous in nature, but their low activity towards OER[21] have made them unsuitable as cathodes for non-aqueous Li-O_2 batteries. Therefore, the strategy of incorporating heavy and poorly conductive NCO electrocatalysts to the lightweight and highly conductive porous carbon materials can result in high-performance cathodes for non-aqueous Li-O_2 batteries.

Reduced graphene oxide aerogel (GA) is a macroporous three-dimensional carbon material constructed from two-dimensional reduced graphene oxide (rGO) sheet and has been widely explored in the fields of energy storage[22,23], pollutant adsorption[24,25] and tissue engineering[26,27]. GA materials can be particularly beneficial for non-aqueous Li-O_2 batteries because the highly conductive rGO network can serve as catalyst support and the macropores can adequately accommodate the discharge product. Jiang et al.[21] reported a Ru functionalized GA cathode with a hierarchical porous structure. The three-dimensional network can facilitate electrolyte permeation and oxygen diffusion, and Ru nanoparticles can significantly enhance the OER activity of the cathode and cycling stability of the battery up to 50 cycles. The differential electrochemical mass spectrometry (DEMS) analysis revealed the evolution of CO_2 above 3.8 V (*vs.* Li/Li^+) in Ru functionalized GA because superoxide and peroxide species are highly active and attack the GA support. These parasitic reactions are commonly observed on carbon-based electrode materials[28]. Luo et al.[29] later reported that by coating carbon with a protective layer, such as a non-reactive ZnO, the contact of the superoxide and peroxide species with carbon can be minimized, which effectively suppresses parasitic reactions. Therefore, it is an attractive prospect to rationally design a

GA cathode in which NCO can serve as both an effective electrocatalyst and a protective layer to protect GA from superoxide and peroxide species. To our best knowledge, no study on this topic has been reported.

Here, we introduce a robust approach to prepare novel macroporous nanocomposites of GAs and NCO nanoplates as freestanding cathodes for non-aqueous Li-O_2 batteries. NCO nanoplates were prepared through a hydrothermal method followed by calcination. Sequentially NCO nanoplates were hybridized on the walls of the macropores in GA via a chemical reduction-induced self-assembly method. The influence of NCO loading in GA support on the battery performance was investigated by tweaking the NCO content. The synergistic effect between the NCO electrocatalysts and GA support is highlighted.

Experimental

Materials. All regents were of analytical grade and were used as received without further purification**.** Graphite flake (100 mesh), potassium permanganate ($KMnO_4$), sodium ascorbate, cobalt nitrate hexahydrate ($Co(NO_3)_2 \cdot 6H_2O$), nickel nitrate hexahydrate ($Ni(NO_3)_2 \cdot 6H_2O$), hexamethylenetetramine (HMTA) and N-methyl-2-pyrrolidone (NMP) were purchased from Sigma-Aldrich. Sodium nitrate ($NaNO_3$), sulfuric acid (H_2SO_4, 98%), hydrogen peroxide (H_2O_2, 30%), sodium hydroxide (NaOH) and polyvinylidene fluoride (PVDF) were supplied by Chem-Supply. Lithium foil was from China Energy Lithium Co., Ltd. Glass fiber membrane (Grade GF/F) was from Whatman. 1M lithium bis(trifluoromethanesulfonyl)imide (LiTFSI) in tetraethylene glycol dimethyl ether (TEGDME) was obtained from Suzhou Qianmin Chemical Reagent Co., Ltd. Ultra-high purity (99.999%) O_2 was provided by Coregas.

Cathode Material Preparation. Graphene oxide (GO) was synthesized according to a previous method with modification[30]. 5 g graphite flake, 3.75 g $NaNO_3$ and 150 mL concentrated H_2SO_4 were added in a 1000 mL beaker. To this mixture, 20 g $KMnO_4$ powder was slowly added under constant stirring of an overhead mixer. After 20 h, the stirring was stopped, and a viscous mixture was formed. The mixture was sat still for 5 days with occasional manual stirring, then, 500 mL DI water was slowly added to the mixture under constant stirring, followed by 30 mL H_2O_2. After stirring for another 2 h, the mixture was washed with a large quantity of DI water and GO was collected by centrifuge. The obtained GO solution was dialyzed with DI water for 2 weeks and then freeze dried.

Mildly reduced GO (mrGO) was synthesized by a chemical reduction method. 150 mg sodium ascorbate was dissolved in 200 mL of 0.5 mg mL^{-1} GO solution, which was heated to 60 ℃ under constant stirring and kept at that temperature for 0.5 h. The prepared mrGO was washed with DI water three times and collected via centrifuge.

NCO nanoplates were synthesized according to our previous method reported in Chapter 3. 3.0 mmol $Co(NO_3)_2 \cdot 6H_2O$, 1.5 mmol $Ni(NO_3)_2 \cdot 6H_2O$ and 1.5 mmol HMTA were dissolved in 60 mL DI water and stirred at room temperature for 0.5 h. The pH of the mixture was adjusted to 10 with 1 M NaOH. The obtained green suspension was stirred at room temperature for 2 h and transferred to a Teflon-lined autoclave. The autoclave was heated to 120 ℃ and maintained at that temperature for 24 h before allowing to cool down naturally. The precipitate was washed with a large quantity of DI water until the supernatant was clear, collected via centrifuge, and dried at 60 ℃ overnight. The dried raw product was further heated in an open-end tube furnace to 350 ℃ at a slow heating rate of 2 ℃ min^{-1} and maintained at that temperature for 2 h to obtain the NCO nanoplates.

Macroporous nanocomposites of reduced graphene oxide aerogels and $NiCo_2O_4$ nanoplates (GANCO) were synthesized through a chemical reduction-induced self-assembly approach. 0.5 mL of 1 mg mL^{-1} mrGO solution was mixed with a certain amount of NCO and sonicated for 1 h. 20 μL of 50 mg mL^{-1} sodium ascorbate solution was added to this mixture, which was further sonicated for 5 min. The mixture was transferred to a capped glass vial with an inner diameter of 1 cm, heated to 95 ℃, and kept at that temperature for 6 h before allowing to cool down naturally. The formed gel was dialyzed with DI water for 2 d and freeze dried to obtain GANCO. GANCO with a GA: NCO feed ratio of 1:2, 1:4 and 1:6 (w/w) were labeled as the GANCO2, GANCO4 and GANCO6. In addition, pure GA without adding NCO was also synthesized through the same procedures. The as-prepared GANCOs were used as cathodes directly without further preparation process. For comparison purpose, the non-freestanding cathode with the same bulk composition of GANCO4 (labeled rGONCO4) was prepared as well: GANCO4 was crushed with a mortar and pestle and mixed with PVDF binder (weight ratio 9:1) in NMP to form a slurry, which was coated on a Ni foam and dried at 80 ℃ overnight.

Material Characterization. Scanning electron microscopy (SEM) was carried out on an FEI Quanta 450 operating at a voltage of 30 kV. Transmission electron microscopy (TEM) was carried out on a Tecnai G2 Spirit operating at a voltage of 120 kV. X-ray diffraction (XRD) patterns were obtained on a Rigaku Miniflex 600 instrument using a Cu Kα radiation source at a scan rate of 5 ° min^{-1}. X-ray photoelectron spectroscopy (XPS) was conducted on a Thermo Fisher Scientific K-Alpha$^+$ Spectrometer using a monochromatic Al Kα radiation operating at 12 kV.

Electrochemical Evaluation. A coin-type battery was assembled in an argon-filled glovebox, with a Li foil as an anode, glass fiber membrane as a separator, and 1 M LiTFSI in TEGDME as the electrolyte. The battery was transferred to a glass chamber, which was purged with oxygen for 15 min. Galvanostatic discharge-charge test was performed on a Neware battery testing system. Cyclic voltammetry (CV) was performed on a CHI600 electrochemical workstation at a scanning rate of 2 mV S^{-1}. Electrochemical impedance spectroscopy (EIS) was performed on a Zahner IM6 electrochemical workstation at open circuit voltage in the frequency range of 100 mHz to 100 kHz.

Results and Discussion

Material Synthesis and Characterization

The NCO nanoplates were synthesized via a hydrothermal method followed by calcination. Figure S4.1 reveals that the synthesized Ni-Co mixed hydroxide precursors are thin hexagonal nanoplates with a circumradius of 150-250 nm as well as smooth surface and well-defined edges. After calcination, Figure 4.1a displays that the morphology of nanoplates is well preserved, but the surface roughens. Associated with water escapes, mesopores are formed during calcination. Mesopores of ~2 nm in size can be clearly observed on the TEM image of the NCO nanoplates (Figure 4.1b).

GANCOs were fabricated by a chemical reduction-induced self-assembly method, with the walls of GA macropores being covered by two-dimensional NCO nanoplates. It is worth noting that mrGO is used as the starting material to fabricate GAs and GANCOs. GAs fabricated directly from GO as the starting material display a “shell” structure[31], which consists of densely stacked rGO sheets that cover the entire GA surface and blocks access to

the inner porous structure (Figure S4.2). The lack of pores for Li_2O_2 deposition can be detrimental, as indicated by the poor battery performance (Figure S4.3). The use of mrGO as a starting material enables the one-pot fabrication of GAs and GANCOs with desired dimensions without any laborious and wasteful post-process. The low-resolution SEM image of pure GA (Figure 4.2a) displays an interconnected, three-dimensional porous framework with continuous macropores 2-30 μm in size. The high-resolution SEM image of GA reveals that the walls of the macropores consist of thin rGO nanosheets (Figure 4.2e). With the addition of NCO nanoplates, the interconnected porous network of GANCO2, GANCO4 and GANCO6 remain mostly intact and resemble that of pure GA (Figures 4.2b-d). High-resolution SEM images (Figures 4.2f-h) reveal that NCO nanoplates are dispersed on the walls of GA macropores. For GANCO2 (Figure 4.2f), NCO loading is low, and NCO nanoplates are distributed sparsely on the walls of macropores. With increased NCO loading, NCO nanoplates are densely distributed on the walls of macropores for GANCO4 and cover the majority of walls of macropores (Figure 4.2g). For GANCO6 (Figure 4.2h), the loading of NCO is excessive, and NCO nanoplates start to aggregate. The TEM image of the GANCO4 (Figure S4.4) clearly illustrates the two distinct structures of hexagonal NCO nanoplates and the almost transparent rGO nanosheets.

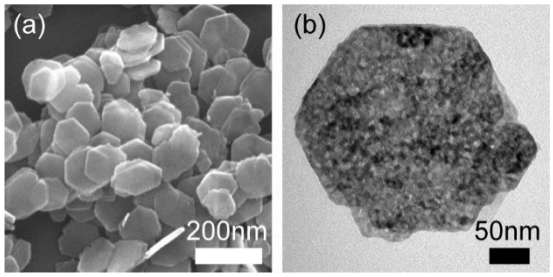

Figure 4.1. (a) SEM image of the NCO nanoplates, (b) TEM image of the NCO nanoplates.

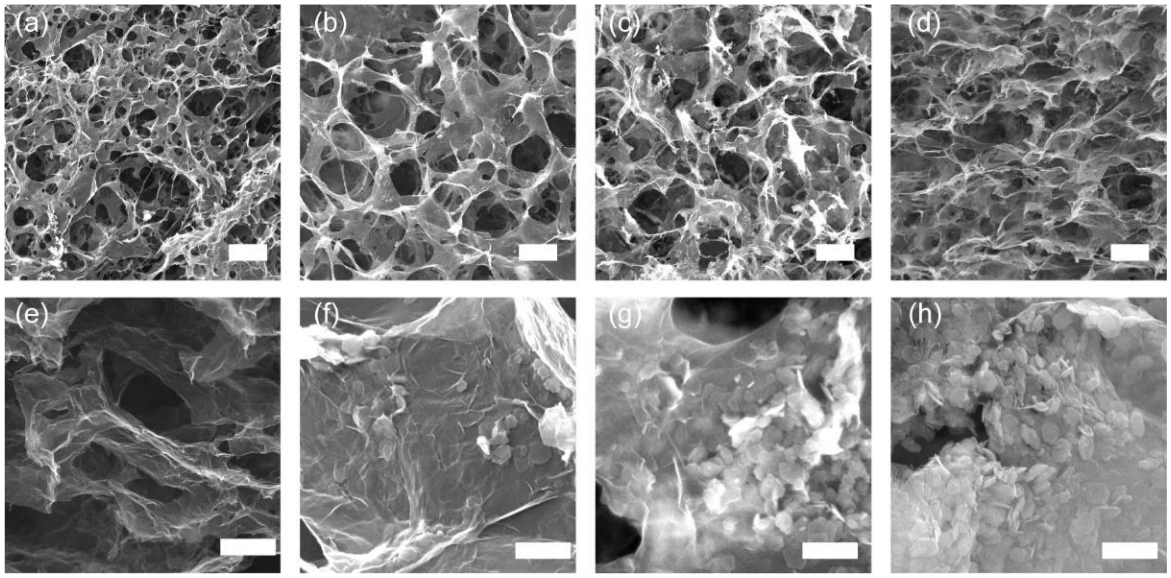

Figure 4.2. Low-resolution SEM images of (a) GA, (b) GANCO2, (c) GANCO4, (d) GANCO6, scale bars indicate 10 μm; high-resolution SEM images of (e) GA, (f) GANCO2, (g) GANCO4, (h) GANCO6, scale bars indicate 1 μm.

The crystal structures of GA, NCO, and GANCOs (represented by GANCO4) were examined by XRD and the results are illustrated in Figure 4.3. GA shows a single broad peak at around 2θ of 25.8°, which corresponds to the (002) diffraction peak of rGO[32]. For NCO, the well-defined peaks at 2θs of 19.0°, 31.2°, 36.8°, 38.5°, 44.8°, 59.0° and 64.6° can be indexed to the (111), (220), (311), (222), (400), (511) and (440) crystal planes of the spinel phase $NiCo_2O_4$ (JCPDS #73-1702). For the GANCO4, both the peaks for rGO and $NiCo_2O_4$ can be identified, confirming the formation of nanocomposite of GAs and NCO nanoplates. Figure 4.4 illustrates the high-resolution XPS spectra of C 1s, O 1s, Co 2p and Ni 2p in GANCO4. The C 1s spectrum can be deconvoluted into four peaks at 284.8, 286.2, 288.3 and 290.9 eV corresponding to the C-C/C=C, C-O, C=O and O=C-O bonds[33]. The peak intensities of O-containing groups are low in comparison to the major C-C/C=C peaks, indicating most O-containing groups are removed after the chemical reduction. The conversion to rGO enhances the conductivity and electrochemical activity of the cathode[34]. The O 1s spectrum displays the metal oxygen bond at 529.6 eV and the C-O bond at 531.5 eV, the peak at 533.1 eV can be attributed to low oxygen coordination species in NCO[35,36], and the small peak at 536.7 eV can be attributed to the chemisorbed O species[37]. The Co 2p spectrum shows the spin-orbit doublet peaks of Co^{2+}, Co^{3+} and two shakeup satellites. The peaks at 779.7 and 794.7 eV can be ascribed to the doublet of Co^{2+} and peaks at 781.2 and 796.4 eV can be ascribed to Co^{3+}. Two satellite peaks of Co can be observed at 786.1 and 802.7 eV[38,39]. The Ni 2p spectrum displays two spin-orbit doublet peaks for Ni^{2+} at 854.2 and 872.4 eV and Ni^{3+} at 855.9 and 874.0 eV. The satellite peaks for Ni can be observed at 861.2 and 879.7 eV[38,39]. These results confirm the formation of NCO with Ni^{2+}/Ni^{3+} and Co^{2+}/Co^{3+} redox couples, providing excellent electrocatalytic activities[40].

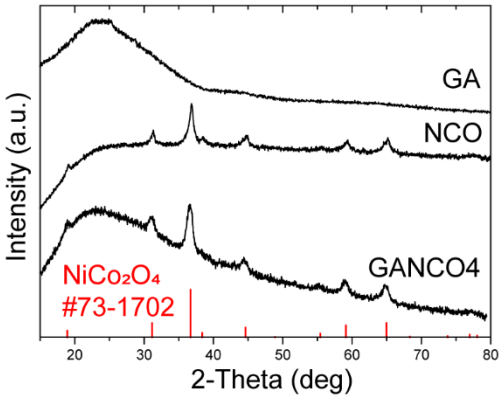

Figure 4.3. Comparison of the XRD patterns of GA, NCO, and GANCO4.

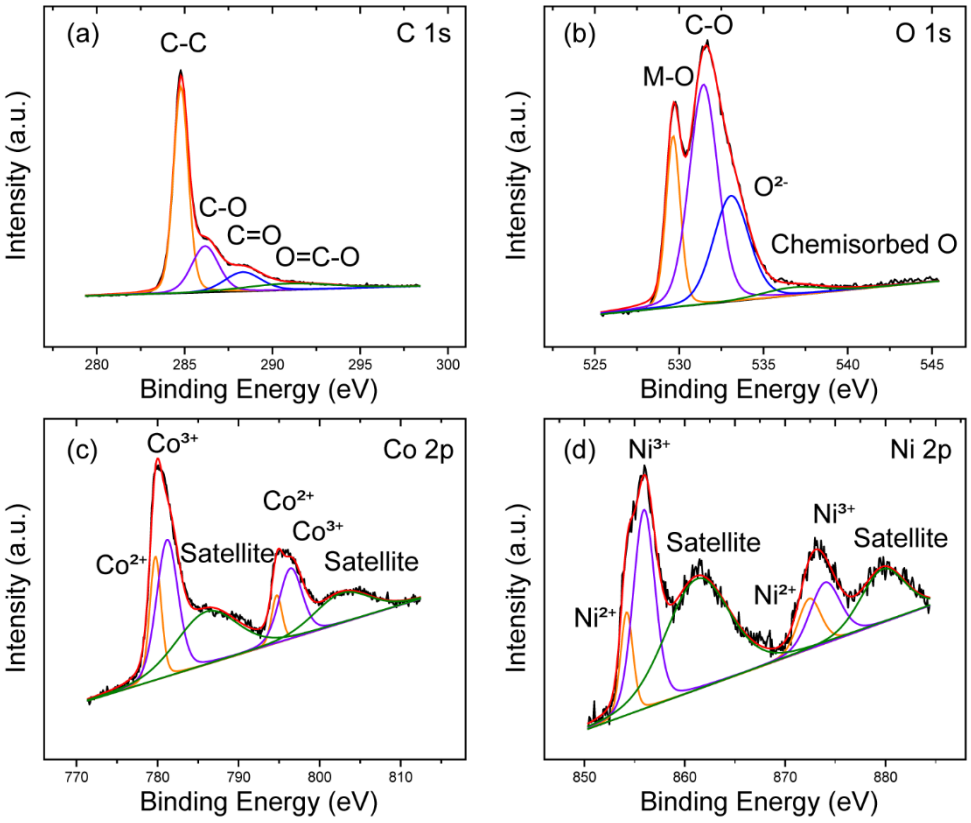

Figure 4.4. XPS spectra of (a) C 1s, (b) O 1s, (c) Co 2p and (d) Ni 2p for GANCO4.

Effect of $NiCo_2O_4$ Loading

The as-prepared GA, GANCO2, GANCO4 and GANCO6 were used directly as freestanding cathodes for non-aqueous Li-O_2 batteries. Their galvanostatic discharge-charge profiles were measured at a current density of 200 mA g^{-1} within the potential window of 2.0-4.5 V (*vs.* Li/Li^+). Figure 4.5a reveals the GA cathode delivers a specific capacity of 3125 mAh g^{-1} with a constant discharge plateau of 2.59 V. During recharge, the potential rises rapidly to the cut-off potential of 4.5 V and consequentially the GA cathode only recovers less than 1000 mAh g^{-1} of capacity, indicating poor OER activity of pure GA cathode. With the introduction of NCO nanoplates, the specific capacities of GANCO2, GANCO4 and GANCO6 are increased to 4078, 4302, and 3916 mAh g^{-1} together with slightly higher discharge plateaus than that of GA, indicating a slight improvement in ORR activity. GANCO4 shows the highest specific capacity, although the difference among these cathodes is marginal. For recharging, all three GANCO cathodes can fully recover their delivered capacities. The charge overpotentials of GANCO2, GANCO4 and GANCO6 are 4.14, 4.03, and 3.91 V. Clearly, the introduction of NCO to GANCOs can promote both ORR and OER activities. Most notably, NCO introduction has a significant impact on the OER activity of cathode, and the content of NCO is directly correlated to the low overpotential. The ORR and OER activities of GANCO2, GANCO4 and GANCO6 cathodes were further characterized by CV measurements with the results shown in Figure 4.5b. The strength of the peaks in both forward (ORR) and backward (OER) directions for all cathodes increases with NCO loading, with GANCO6 being the most active cathode for both ORR and OER, owing to its high NCO loading.

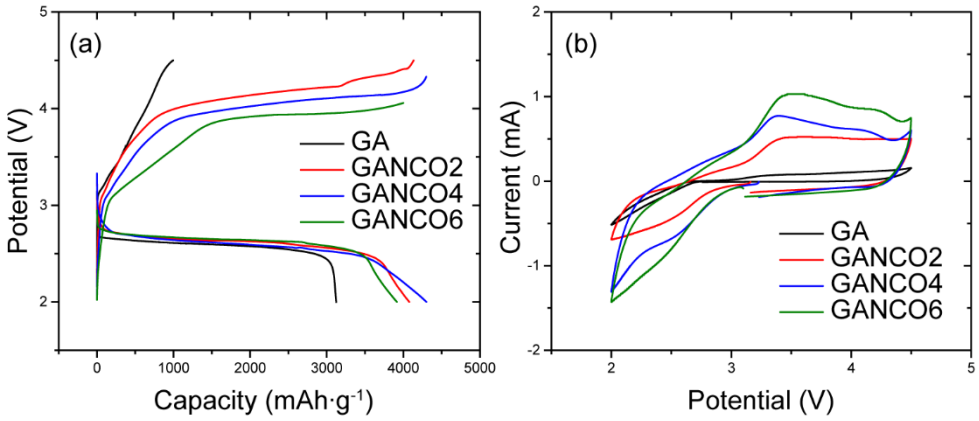

Figure 4.5. (a) The initial galvanostatic discharge-charge profiles of GA, GANCO2, GANCO4 and GANCO6 being measured at a current density of 200 mA g^{-1} in the potential window of 2.0-4.5 V; (b) the CV curves of GA, GANCO2, GANCO4 and GANCO6 being measured at a scanning rate of 2 mV S^{-1} in the potential window of 2.0-4.5 V.

The cycling performance of GA, GANCO2, GANCO4 and GANCO6 cathodes were tested at a current density of 200 mA g^{-1} and limited capacity of 500 mAh g^{-1}. As illustrated in Figure S4.5, the battery with pure GA cathode can only maintain 14 cycles with a high overpotential of 1.55 V during the initial cycle. The overpotentials during the initial cycle of GANCO2, GANCO4 and GANCO6 are 1.06, 0.91 and 0.54 V. Evidently, the introduction of NCO in GANCO cathodes can significantly reduce the overpotentials of the batteries, and the reduction of the overpotentials is correlated to increasing NCO loading. In addition, with the increase of NCO loading, the cycles of the batteries increase from 33 cycles of GANCO2 to 82 cycles of GANCO4. When the loading is further increased, the cycles of GANCO6 drop to 52 cycles. Although high NCO loading can be associated with enhanced OER activity, as indicated by the overpotentials and previous CV results, the cycling performance results suggests that NCO loading is not the only factor that governs the long-term stability of the battery. NCO nanoplates with relatively low conductivity can aggregate on walls of macropores in GANCO6 and hinder the charge transport properties of cathode materials.

EIS measurements were further conducted on pristine GANCO2, GANCO4 and GANCO6 cathodes to characterize their charge transport properties under O_2 atmosphere. Figure S4.6 illustrates their Nyquist plots and the charge transfer resistance (R_{ct}) is calculated by the radius of the semicircles at the high-frequency region. The R_{ct} values of GANCO2, GANCO4 and GANCO6 are 87.7, 115.1, and 148.3 Ω. The impedances of the cathodes are correlated with the content of NCO, and higher NCO loading results in the decline of the conductivity of the cathodes.

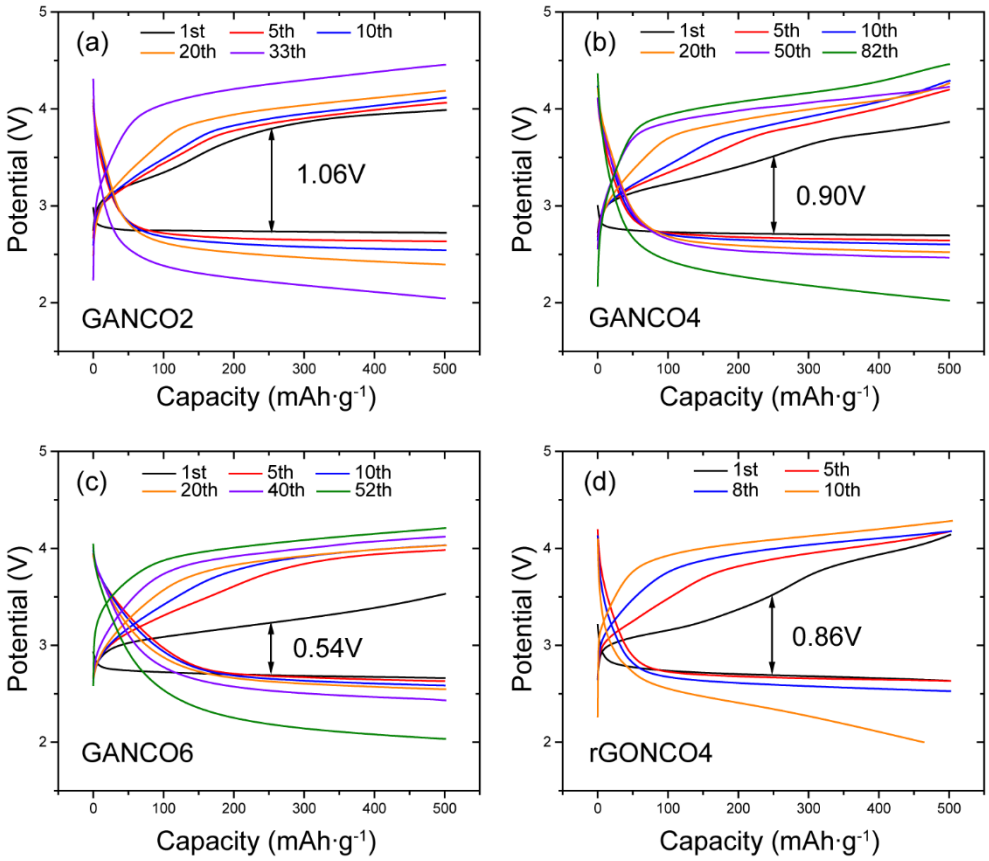

Figure 4.6. The cycling performance of (a) GANCO2, (b) GANCO4, (c) GANCO6 and (d) rGONCO4 cathodes being measured at a current density of 200 mA g^{-1} and limited capacity of 500 mAh g^{-1}.

These results indicate that the overall cycling performance of the battery is regulated by the balance of NCO coverage on walls of macropores and cathode conductivity. The highly catalytical active NCO offers abundant active sites towards OER, and more importantly, these nanoplates can cover the rGO nanosheet entirely to minimize its contact with active peroxide or superoxide species during electrochemistry, which suppresses the decomposition of rGO, alleviates parasitic reactions and improves stability[41]. In this regard, the high loading of NCO is beneficial for the improvement of OER activity and the suppression of parasitic reactions. On the other hand, the high loading of NCO content also reduces the conductivities of the cathodes. For GANCO2, although it shows the highest conductivity, the low NCO coverage on the walls of macropores leads to overall low OER activity. For GANCO6, the NCO nanoplates start to aggregate into a thicker layer of stacked nanoplates. The buried nanoplates under the aggregated layer do not have access to the surface and are not active; these inactive masses can only hinder the overall charge transport properties of the cathodes. GANCO4 shows the optimal balance between high NCO coverage and conductivity. The superior cycling performance of GANCO4 can be ascribed to the synergistic effect of the conductive GA support with an opportune amount of NCO nanoplates. Notably, compared to non-reactive ZnO and Al_2O_3 protective layers being reported in previous literature[29,42], NCO nanoplates reveal its dual roles of protection and OER activity on the performance enhancement of GANCOs. Consequentially, the cyclability of GANCO4 cathode is improved over previously reported GA/electrocatalyst nanocomposite cathodes[21,43] for non-aqueous Li-O_2 batteries.

Effect of Freestanding Macroporous Structure

The advantages of the freestanding macroporous structure of GANCO4 is further evaluated. A rGONCO4 cathode without macropores but has an identical bulk composition as that of GANCO4 cathode was fabricated through a conventional coating method from a slurry of crushed GANCO4 and inactive PVDF binder. The cycling performance of rGONCO4 cathode was compared with that of GANCO4. Figure 4.6d illustrates that during the initial cycle, rGONCO4 cathode shows an overpotential of 0.86 V, which is similar to that of the GANCO4 (0.90 V). This can be ascribed to their identical chemical compositions. However, the GANCO4 cathode can maintain 82 cycles, but the rGONCO4 cathode is only stable for 10 cycles. Obviously, the freestanding and macroporous GANCO4 exhibits far superior stability than the cathode being fabricated with a conventional coating method. As such, the freestanding macroporous structure also provides an extra contribution to the performance of non-aqueous Li-O_2 battery. The large macropores can promote electrolyte permeation and oxygen diffusion[43]. In addition, the freestanding design avoids the usage of binders, which are well-known for their instabilities in non-aqueous Li-O_2 batteries that hinder the long-term stability[18]. The superior cycling performance of GANCO4 can also be ascribed to the freestanding macroporous structure of the cathode materials.

Conclusion

Inspired by the unique characteristics and limitations of NCO and rGO cathodes for non-aqueous Li-O_2 batteries, a series of freestanding and macroporous nanocomposites of GAs and NCO nanoplates were synthesized through a robust one-pot reaction. NCO nanoplates are not only electrocatalysts for the electrochemical reaction but also minimize the contact

of GA with highly reactive superoxide and peroxide species during electrochemistry to minimize GA decomposition. GANCO4 exhibits an optimal GA and NCO feed ratio, where NCO nanoplates fully cover the walls of macropores without hindering the charge transport properties of GA. As a result, it delivers a specific capacity of 4302 mAh g^{-1} when discharged at a current density of 200 mA g^{-1} and cyclability of 82 cycles at a current density of 200 mA g^{-1} and limited capacity of 500 mAh g^{-1}. The freestanding macroporous structure also plays a critical role in cycling performance. The superior performance of GANCO4 cathode can be attributed to the synergistic effect between the GA support and an opportune amount of NCO, as well as the unique freestanding macroporous structure. The three-dimensional macroporous network consists of conductive GA support can provide facile electron and mass transfer, while the NCO occupying on the walls of the macropores can provide abundant active sites for electrochemical reactions, as well as act as a protective layer for GA to suppress the parasitic reactions between GA and superoxides and peroxides.

Associated Content

Supporting Information

SEM image of NCO precursor; TEM image of GANCO4; SEM image of a GA fabricated directly from GO; a galvanostatic discharge-charge profile of GA fabricated directly from GO; cycling performance of GA; EIS spectra of GANCO2, GANCO4, and GANCO6.

Acknowledgments

This work was financially supported by the Australian Research Council Discovery Projects DP140104062.

References

(1) Lu, J.; Li, L.; Park, J.-B.; Sun, Y.-K.; Wu, F.; Amine, K. Aprotic and Aqueous Li-O_2 Batteries. *Chem. Rev.* **2014**, *114* (11), 5611–5640.

(2) Lyu, Z.; Zhou, Y.; Dai, W.; Cui, X.; Lai, M.; Wang, L.; Huo, F.; Huang, W.; Hu, Z.; Chen, W. Recent Advances in Understanding of the Mechanism and Control of Li_2O_2 Formation in Aprotic Li-O_2 Batteries. *Chem. Soc. Rev.* **2017**, *46* (19), 6046–6072.

(3) Aurbach, D.; McCloskey, B. D.; Nazar, L. F.; Bruce, P. G. Advances in Understanding Mechanisms Underpinning Lithium-Air Batteries. *Nat. Energy* **2016**, *1* (9), 16128.

(4) Ma, L.; Yu, T.; Tzoganakis, E.; Amine, K.; Wu, T.; Chen, Z.; Lu, J. Fundamental Understanding and Material Challenges in Rechargeable Nonaqueous Li-O_2 Batteries: Recent Progress and Perspective. *Adv. Energy Mater.* **2018**, *8* (22), 1800348.

(5) Wu, Z.; Zhu, Y.; Ji, X. $NiCo_2O_4$-Based Materials for Electrochemical Supercapacitors. *J. Mater. Chem. A* **2014**, *2* (36), 14759–14772.

(6) Chen, P.; Yang, J.-J.; Li, S.-S.; Wang, Z.; Xiao, T.-Y.; Qian, Y.-H.; Yu, S.-H. Hydrothermal Synthesis of Macroscopic Nitrogen-Doped Graphene Hydrogels for Ultrafast Supercapacitor. *Nano Energy* **2013**, *2* (2), 249–256.

(7) Fu, F.; Li, J.; Yao, Y.; Qin, X.; Dou, Y.; Wang, H.; Tsui, J.; Chan, K.-Y.; Shao, M. Hierarchical $NiCo_2O_4$ Micro- and Nanostructures with Tunable Morphologies as Anode Materials for Lithium- and Sodium-Ion Batteries. *ACS Appl. Mater. Interfaces* **2017**, *9* (19), 16194–16201.

(8) Shen, L.; Yu, L.; Yu, X.-Y.; Zhang, X.; Lou, X. W. (David). Self-Templated Formation of Uniform $NiCo_2O_4$ Hollow Spheres with Complex Interior Structures for Lithium-Ion Batteries and Supercapacitors. *Angew. Chem. Int. Ed.* **2015**, *54* (6), 1868–1872.

(9) Wang, Z.; Zeng, S.; Liu, W.; Wang, X.; Li, Q.; Zhao, Z.; Geng, F. Coupling Molecularly Ultrathin Sheets of NiFe-Layered Double Hydroxide on $NiCo_2O_4$ Nanowire Arrays for Highly Efficient Overall Water-Splitting Activity. *ACS Appl. Mater. Interfaces* **2017**, *9* (2), 1488–1495.

(10) Gao, X.; Zhang, H.; Li, Q.; Yu, X.; Hong, Z.; Zhang, X.; Liang, C.; Lin, Z. Hierarchical $NiCo_2O_4$ Hollow Microcuboids as Bifunctional Electrocatalysts for Overall Water-Splitting. *Angew. Chem.* **2016**, *128* (21), 6398–6402.

(11) Shi, X.; Bernasek, S. L.; Selloni, A. Oxygen Deficiency and Reactivity of Spinel $NiCo_2O_4$ (001) Surfaces. *J. Phys. Chem. C* **2017**, *121* (7), 3929–3937.

(12) Bo, X.; Zhang, Y.; Li, M.; Nsabimana, A.; Guo, L. $NiCo_2O_4$ Spinel/Ordered Mesoporous Carbons as Noble-Metal Free Electrocatalysts for Oxygen Reduction Reaction and the Influence of Structure of Catalyst Support on the Electrochemical Activity of $NiCo_2O_4$. *J. Power Sources* **2015**, *288*, 1–8.

(13) Gong, H.; Xue, H.; Wang, T.; Guo, H.; Fan, X.; Song, L.; Xia, W.; He, J. High-Loading Nickel Cobaltate Nanoparticles Anchored on Three-Dimensional N-Doped Graphene

as an Efficient Bifunctional Catalyst for Lithium-Oxygen Batteries. *ACS Appl. Mater. Interfaces* **2016**, *8* (28), 18060–18068.

(14) Mohamed, S. G.; Tsai, Y.-Q.; Chen, C.-J.; Tsai, Y.-T.; Hung, T.-F.; Chang, W.-S.; Liu, R.-S. Ternary Spinel MCo_2O_4 (M = Mn, Fe, Ni, and Zn) Porous Nanorods as Bifunctional Cathode Materials for Lithium-O_2 Batteries. *ACS Appl. Mater. Interfaces* **2015**, *7* (22), 12038–12046.

(15) Li, L.; Shen, L.; Nie, P.; Pang, G.; Wang, J.; Li, H.; Dong, S.; Zhang, X. Porous $NiCo_2O_4$ Nanotubes as a Noble-Metal-Free Effective Bifunctional Catalyst for Rechargeable Li-O_2 Batteries. *J. Mater. Chem. A* **2015**, *3* (48), 24309–24314.

(16) Zhang, L.; Zhang, S.; Zhang, K.; Xu, G.; He, X.; Dong, S.; Liu, Z.; Huang, C.; Gu, L.; Cui, G. Mesoporous $NiCo_2O_4$ Nanoflakes as Electrocatalysts for Rechargeable Li-O_2 Batteries. *Chem. Commun.* **2013**, *49* (34), 3540–3542.

(17) Sun, B.; Huang, X.; Chen, S.; Zhao, Y.; Zhang, J.; Munroe, P.; Wang, G. Hierarchical Macroporous/Mesoporous $NiCo_2O_4$ Nanosheets as Cathode Catalysts for Rechargeable Li-O_2 Batteries. *J. Mater. Chem. A* **2014**, *2* (30), 12053–12059.

(18) Papp, J. K.; Forster, J. D.; Burke, C. M.; Kim, H. W.; Luntz, A. C.; Shelby, R. M.; Urban, J. J.; McCloskey, B. D. Poly(Vinylidene Fluoride) (PVDF) Binder Degradation in Li-O_2 Batteries: A Consideration for the Characterization of Lithium Superoxide. *J. Phys. Chem. Lett.* **2017**, *8* (6), 1169–1174.

(19) Lin, X.; Su, J.; Li, L.; Yu, A. Hierarchical Porous $NiCo_2O_4$@Ni as Carbon-Free Electrodes for Lithium-Oxygen Batteries. *Electrochim. Acta* **2015**, *168*, 292–299.

(20) Liu, W.-M.; Gao, T.-T.; Yang, Y.; Sun, Q.; Fu, Z.-W. A Hierarchical Three-Dimensional $NiCo_2O_4$ Nanowire Array/Carbon Cloth as an Air Electrode for Nonaqueous Li-Air Batteries. *Phys. Chem. Chem. Phys.* **2013**, *15* (38), 15806–15810.

(21) Jiang, J.; He, P.; Tong, S.; Zheng, M.; Lin, Z.; Zhang, X.; Shi, Y.; Zhou, H. Ruthenium Functionalized Graphene Aerogels with Hierarchical and Three-Dimensional Porosity as a Free-Standing Cathode for Rechargeable Lithium-Oxygen Batteries. *NPG Asia Mater.* **2016**, *8* (1), e239–e239.

(22) Fu, X.; Chen, Y.; Zhu, Y.; Jana, S. C. Synergetic Hybrid Aerogels of Vanadia and Graphene as Electrode Materials of Supercapacitors. *C* **2016**, *2* (3), 21.

(23) Chen, Z.; Li, H.; Tian, R.; Duan, H.; Guo, Y.; Chen, Y.; Zhou, J.; Zhang, C.; Dugnani, R.; Liu, H. Three Dimensional Graphene Aerogels as Binder-Less, Freestanding, Elastic and High-Performance Electrodes for Lithium-Ion Batteries. *Sci. Rep.* **2016**, *6*, 27365.

(24) Shi, L.; Chen, K.; Du, R.; Bachmatiuk, A.; Rümmeli, M. H.; Xie, K.; Huang, Y.; Zhang, Y.; Liu, Z. Scalable Seashell-Based Chemical Vapor Deposition Growth of Three-Dimensional Graphene Foams for Oil-Water Separation. *J. Am. Chem. Soc.* **2016**, *138* (20), 6360–6363.

(25) Liang, Q.; Luo, H.; Geng, J.; Chen, J. Facile One-Pot Preparation of Nitrogen-Doped Ultra-Light Graphene Oxide Aerogel and Its Prominent Adsorption Performance of Cr(VI). *Chem. Eng. J.* **2018**, *338*, 62–71.

(26) Wang, L.; Zhang, X.; He, Y.; Wang, Y.; Zhong, W.; Mequanint, K.; Qiu, X.; Xing, M. Ultralight Conductive and Elastic Aerogel for Skeletal Muscle Atrophy Regeneration. *Adv. Funct. Mater.* **2019**, *29* (1), 1806200.

(27) Asha, S.; Ananth, A. N.; Jose, S. P.; Rajan, M. A. J. Reduced Graphene Oxide Aerogel Networks with Soft Interfacial Template for Applications in Bone Tissue Regeneration. *Appl. Nanosci.* **2018**, *8* (3), 395–405.

(28) Zhao, Z.; Huang, J.; Peng, Z. Achilles' Heel of Lithium-Air Batteries: Lithium Carbonate. *Angew. Chem. Int. Ed.* **2018**.

(29) Luo, X.; Piernavieja-Hermida, M.; Lu, J.; Wu, T.; Wen, J.; Ren, Y.; Miller, D.; Fang, Z. Z.; Lei, Y.; Amine, K. Pd Nanoparticles on ZnO-Passivated Porous Carbon by Atomic Layer Deposition: An Effective Electrochemical Catalyst for Li-O_2 Battery. *Nanotechnology* **2015**, *26* (16), 164003.

(30) Hummers, W. S.; Offeman, R. E. Preparation of Graphitic Oxide. *J. Am. Chem. Soc.* **1958**, *80* (6), 1339–1339.

(31) Hu, K.; Xie, X.; Cerruti, M.; Szkopek, T. Controlling the Shell Formation in Hydrothermally Reduced Graphene Hydrogel. *Langmuir* **2015**, *31* (20), 5545–5549.

(32) Wang, Y.; Liu, Y.; Zhang, J. Colloid Electrostatic Self-Assembly Synthesis of SnO_2/Graphene Nanocomposite for Supercapacitors. *J. Nanoparticle Res.* **2015**, *17* (10), 420.

(33) Sumboja, A.; Foo, C. Y.; Wang, X.; Lee, P. S. Large Areal Mass, Flexible and Free-Standing Reduced Graphene Oxide/Manganese Dioxide Paper for Asymmetric Supercapacitor Device. *Adv. Mater.* **2013**, *25* (20), 2809–2815.

(34) Zeng, G.; Shi, N.; Hess, M.; Chen, X.; Cheng, W.; Fan, T.; Niederberger, M. A General Method of Fabricating Flexible Spinel-Type Oxide/Reduced Graphene Oxide Nanocomposite Aerogels as Advanced Anodes for Lithium-Ion Batteries. *ACS Nano* **2015**, *9* (4), 4227–4235.

(35) Yuan, H.; Li, J.; Yang, W.; Zhuang, Z.; Zhao, Y.; He, L.; Xu, L.; Liao, X.; Zhu, R.; Mai, L. Oxygen Vacancy-Determined Highly Efficient Oxygen Reduction in $NiCo_2O_4$/Hollow Carbon Spheres. *ACS Appl. Mater. Interfaces* **2018**, *10* (19), 16410–16417.

(36) Ko, T.-H.; Devarayan, K.; Seo, M.-K.; Kim, H.-Y.; Kim, B.-S. Facile Synthesis of Core/Shell-like $NiCo_2O_4$-Decorated MWCNTs and Its Excellent Electrocatalytic Activity for Methanol Oxidation. *Sci. Rep.* **2016**, *6* (1), 20313.

(37) Oh, Y. J.; Yoo, J. J.; Kim, Y. I.; Yoon, J. K.; Yoon, H. N.; Kim, J.-H.; Park, S. B. Oxygen Functional Groups and Electrochemical Capacitive Behavior of Incompletely Reduced Graphene Oxides as a Thin-Film Electrode of Supercapacitor. *Electrochim. Acta* **2014**, *116*, 118–128.

(38) Abouali, S.; Akbari Garakani, M.; Xu, Z.-L.; Kim, J.-K. $NiCo_2O_4$/CNT Nanocomposites as Bi-Functional Electrodes for Li Ion Batteries and Supercapacitors. *Carbon* **2016**, *102*, 262–272.

(39) Zheng, Y.; Lin, Z.; Chen, W.; Liang, B.; Du, H.; Yang, R.; He, X.; Tang, Z.; Gui, X. Flexible, Sandwich-like CNTs/$NiCo_2O_4$ Hybrid Paper Electrodes for All-Solid State Supercapacitors. *J Mater Chem A* **2017**, *5* (12), 5886–5894.

(40) Zhang, H.; Li, H.; Wang, H.; He, K.; Wang, S.; Tang, Y.; Chen, J. $NiCo_2O_4$/N-Doped Graphene as an Advanced Electrocatalyst for Oxygen Reduction Reaction. *J. Power Sources* **2015**, *280*, 640–648.

(41) Shang, C.; Dong, S.; Hu, P.; Guan, J.; Xiao, D.; Chen, X.; Zhang, L.; Gu, L.; Cui, G.; Chen, L. Compatible Interface Design of CoO-Based Li-O_2 Battery Cathodes with Long-Cycling Stability. *Sci. Rep.* **2015**, *5*, 8335.

(42) Lu, J.; Lei, Y.; Lau, K. C.; Luo, X.; Du, P.; Wen, J.; Assary, R. S.; Das, U.; Miller, D. J.; Elam, J. W.; et al. A Nanostructured Cathode Architecture for Low Charge Overpotential in Lithium-Oxygen Batteries. *Nat. Commun.* **2013**, *4*, 2383.

(43) Li, L.; Chen, C.; Su, J.; Kuang, P.; Zhang, C.; Yao, Y.; Huang, T.; Yu, A. Three-Dimensional MoS_x ($1 < x < 2$) Nanosheets Decorated Graphene Aerogel for Lithium-Oxygen Batteries. *J. Mater. Chem. A* **2016**, *4* (28), 10986–10991.

Table of Contents

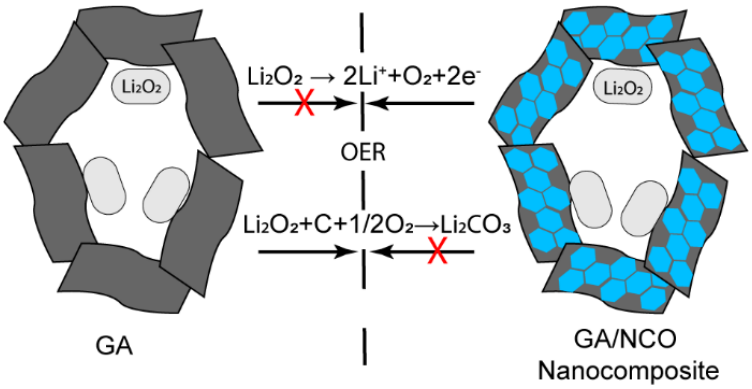

Supporting Information

Macroporous Nanocomposites of Reduced Graphene Oxide Aerogels and $NiCo_2O_4$ Nanoplates for Non-Aqueous Li-O_2 Battery

Heng Wang,[†] Qi Bi,[†] Haihui Wang,[*,†,‡] Sheng Dai [*,†,§]

† School of Chemical Engineering and Advanced Materials, the University of Adelaide, Adelaide, South Australia 5005, Australia

‡ School of Chemistry & Chemical Engineering, South China University of Technology, 381 Wushan Road, Guangzhou 510640, China

§ Department of Chemical Engineering, Brunel University London, Uxbridge, UB8 3PH, United Kingdom

Corresponding author

*E-mail: hhwang@scut.edu.cn

*E-mail: s.dai@adelaide.edu.au

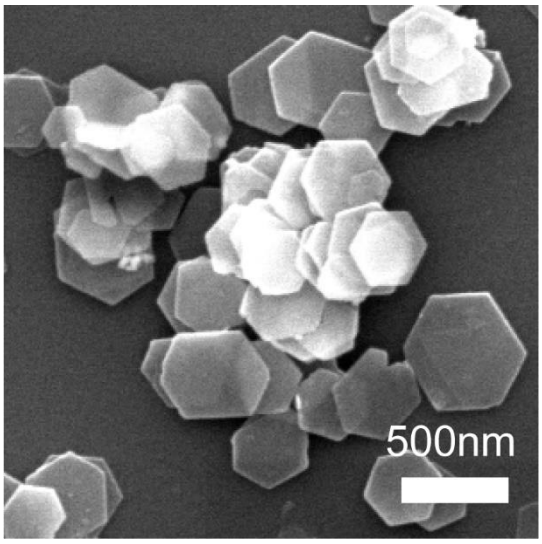

Figure S4.1. The SEM image of the NCO precursor.

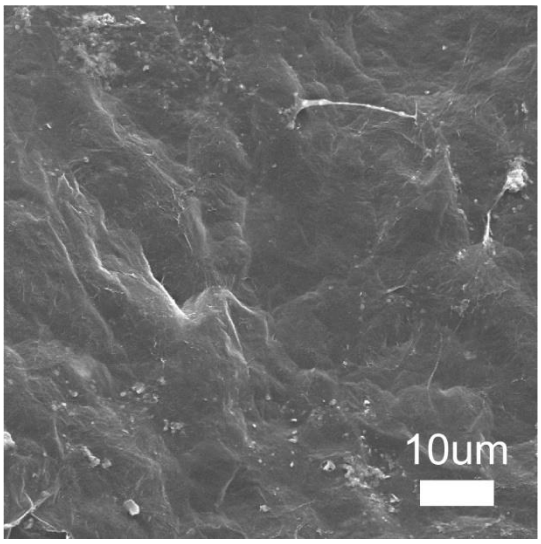

Figure S4.2. SEM image of a GA fabricated directly from GO.

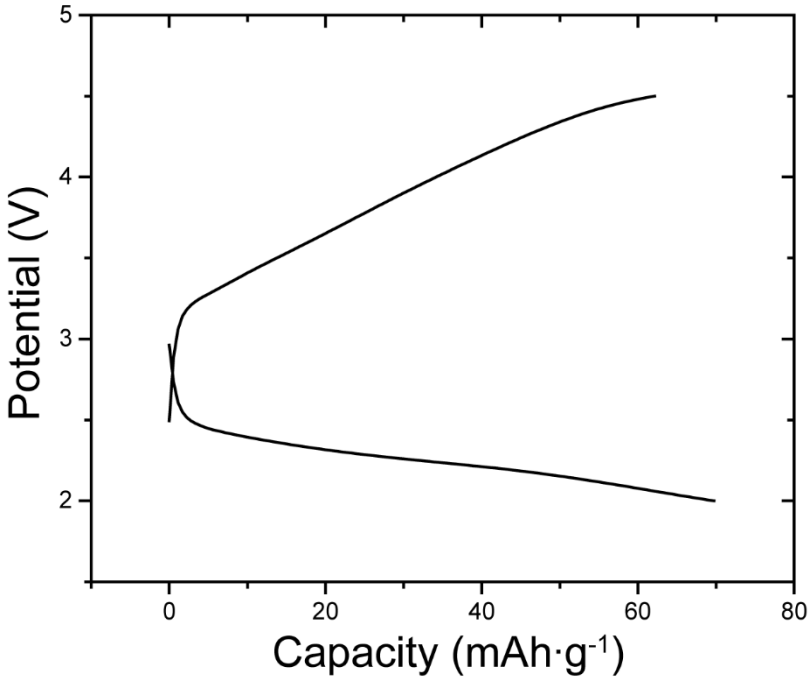

Figure S4.3. The initial galvanostatic discharge-charge profile of the GA fabricated directly from GO measured at a current density of 200 mA g^{-1} in the potential window of 2.0-4.5 V. The minimal capacity suggests the GA fabricated directly from GO has no electrochemical activity for non-aqueous Li-O_2 batteries.

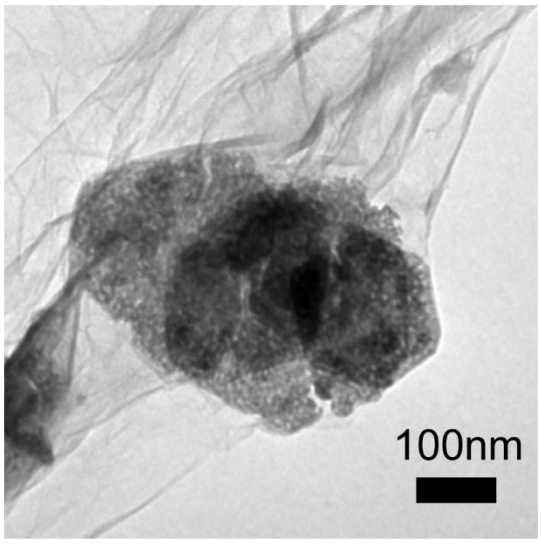

Figure S4.4. TEM image of the GANCO4.

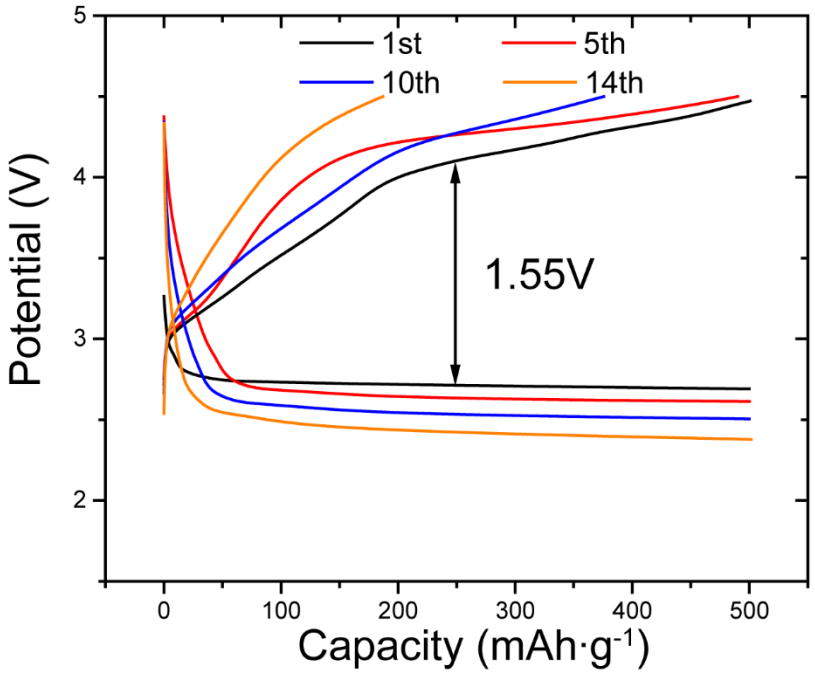

Figure S4.5. Cycling performance of pure GA cathode measured at a current density of 200 mA g^{-1} and limited capacity of 500 mAh g^{-1}.

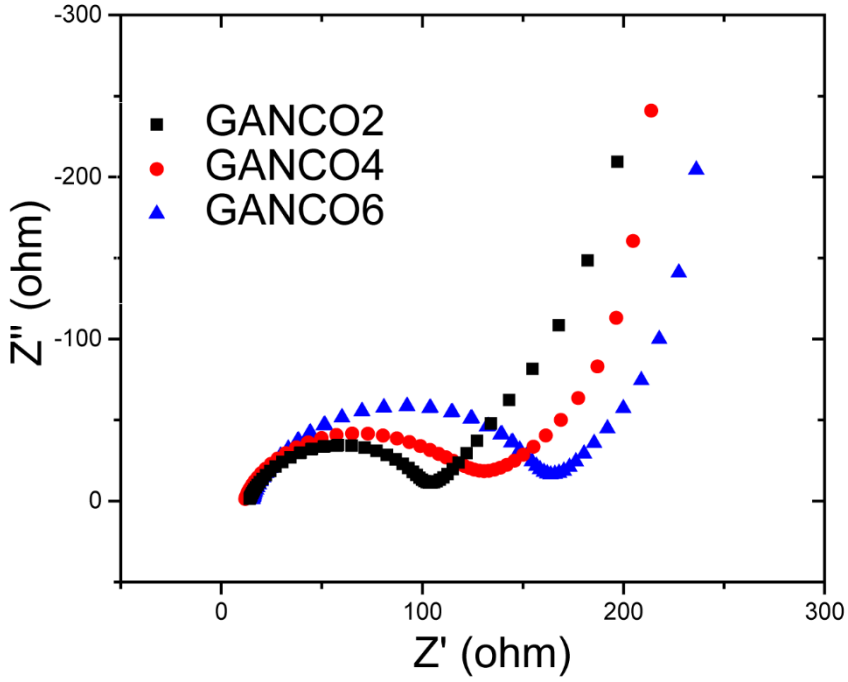

Figure S4.6. EIS spectra of the pristine GANCO2, GANCO4 and GANCO6 cathodes measured in the frequency range of 100 mHz and 100 kHz.

Chapter 5 Controlling Morphology and Crystallinity of Li_2O_2 with Macroporous $NiCo_2O_4$@CNT Cathodes for High-Performance Li-O_2 Battery

5.1. Introduction and Significance

Efficient accommodation of solid Li_2O_2 discharge products in porous cathodes is crucial to achieving the high discharge capacity of non-aqueous Li-O_2 batteries. Although the Li_2O_2 formed through a surface growth pathway can be facilely decomposed and display low potential during charge, the capacity of this pathway is severely limited by the formation of an insulating crystalline Li_2O_2 layer that passivates cathode surfaces. This layer is limited to 5-10 nm, which leads to low Li_2O_2 production and discharge capacity. This work aims to enhance the capacity performance of the surface growth pathway by promoting formation of amorphous Li_2O_2 layers with improved conductivity through rational design of $NiCo_2O_4$@CNT surfaces. The output of this work provides a new strategy to design high-capacity, long-lifespan Li-O_2 batteries via surface growth pathway. The highlights of this work include:

1. For the first time, novel freestanding macroporous $NiCo_2O_4$@CNT cathodes have been designed and synthesized via a self-assembly method.
2. Attributed to defect-rich $NiCo_2O_4$ surfaces, the surfaces of $NiCo_2O_4$@CNT promotes formation of a thick amorphous Li_2O_2 layer.
3. Amorphous Li_2O_2 with improved conductivity delays cathode passivation and promotes the thickness growth of Li_2O_2 layer to boost battery capacity .

4. The layer morphology of amorphous Li_2O_2 reduces charge potential during charge and leads to an excellent cyclability of 343 cycles, which is superior to any previously reported cathodic $NiCo_2O_4$ materials.

5.2. Controlling Morphology and Crystallinity of Li_2O_2 with Macroporous $NiCo_2O_4$@CNT Cathodes for High-Performance Li-O_2 Batteries

This section is included as an unsubmitted manuscript by Heng Wang, Qi Bi, Haihui Wang, Sheng Dai, Controlling Morphology and Crystallinity of Li_2O_2 with Macroporous $NiCo_2O_4$@CNT Cathodes for High-Performance Li-O_2 Batteries.

Statement of Authorship

Title of Paper	Controlling Morphology and Crystallinity of Li_2O_2 with Macroporous $NiCo_2O_4$@CNT Cathodes for High-performance Li-O_2 Batteries
Publication Status	☐ Published ☐ Accepted for Publication ☐ Submitted for Publication ☑ Unpublished and Unsubmitted work written in manuscript style
Publication Details	To be submitted

Principal Author

Name of Principal Author (Candidate)	Heng Wang		
Contribution to the Paper	Research plan, material synthesis, material characterization, battery performance evaluation, data analysis, and manuscript drafting and editing.		
Overall percentage (%)	85%		
Certification:	This paper reports on original research I conducted during the period of my Higher Degree by Research candidature and is not subject to any obligations or contractual agreements with a third party that would constrain its inclusion in this thesis. I am the primary author of this paper.		
Signature	Heng Wang	Date	30/04/2019

Co-Author Contributions

By signing the Statement of Authorship, each author certifies that:

i. the candidate's stated contribution to the publication is accurate (as detailed above);

ii. permission is granted for the candidate in include the publication in the thesis; and

iii. the sum of all co-author contributions is equal to 100% less the candidate's stated contribution.

Name of Co-Author	Qi Bi		
Contribution to the Paper	Discussion of research plan		
Signature		Date	02/05/2019

Name of Co-Author	Prof. Haihui Wang		
Contribution to the Paper	Help to evaluate and edit manuscript		
Signature		Date	30/04/2019

Name of Co-Author	Prof. Sheng Dai		
Contribution to the Paper	Supervision for the development of work and manuscript evaluation		
Signature		Date	30 April 2019

Please cut and paste additional co-author panels here as required.

Controlling Morphology and Crystallinity of Li_2O_2 with Macroporous $NiCo_2O_4$@CNT Cathodes for High-Performance Li-O_2 Batteries

Heng Wang,[†] Qi Bi,[†] Haihui Wang,[*,†,‡] Sheng Dai [*,†,§]

† School of Chemical Engineering and Advanced Materials, the University of Adelaide, Adelaide, South Australia 5005, Australia

‡ School of Chemistry & Chemical Engineering, South China University of Technology, 381 Wushan Road, Guangzhou 510640, China

§ Department of Chemical Engineering, Brunel University London, Uxbridge, UB8 3PH, United Kingdom

Corresponding author

*E-mail: hhwang@scut.edu.cn

*E-mail: s.dai@adelaide.edu.au

Abstract

Non-aqueous Li-O_2 batteries have attracted attention in recent years due to their exceptional theoretical specific capacities. The surface growth pathway for Li_2O_2 production shows superior performance during oxygen evolution reaction (OER) and is therefore ideal for highly stable Li-O_2 batteries. However, the capacity of this pathway is severely limited by the formation of a thin insulating crystalline Li_2O_2 layer that rapidly passivates cathode surfaces. In this study, a novel macroporous $NiCo_2O_4$@CNT cathode was fabricated via a vacuum filtration-assisted self-assembly method with polystyrene microspheres as templates for macropore generation. The $NiCo_2O_4$ coated CNT surfaces are found to promote the formation of amorphous Li_2O_2 with significantly improved conductivity. Consequently, the layer can grow up to 50 nm before the cathode is fully passivated, which boosts Li_2O_2 production and capacity (6165 mAh g^{-1}) of the batteries. The amorphous Li_2O_2 can improve OER kinetics and be facilely decomposed, leading to an excellent cyclability of 343 cycles. This study has demonstrated a novel strategy to circumvent the low capacity issue of surface growth pathway by promoting the formation of amorphous Li_2O_2 with improved conductivity.

Keywords: non-aqueous Li-O_2 batteries, surface growth pathway, macroporous, amorphous Li_2O_2, $NiCo_2O_4$, CNT.

Introduction

Non-aqueous Li-O_2 batteries possess an exceptionally high specific energy of ~3600 $W \cdot h \cdot kg^{-1}$, which is five to ten times larger than the state-of-the-art Li-ion batteries[1]. They have sparked considerable interest in recent years as promising energy storage devices. However, non-aqueous Li-O_2 batteries are still in the early stage of development and are facing numerous issues such as high polarization, low round-trip efficiency and poor stability[2]. In order to overcome these problems, efforts have been made to understand and control the formation and decomposition process of the Li_2O_2 discharge product[3]. In a typical non-aqueous Li-O_2 system, the formation of Li_2O_2 during the oxygen reduction reaction (ORR) follows these reactions[4]:

$$O_2 + e^- \rightarrow O_2^- \tag{5.1}$$

$$O_2^- + Li^+ \rightarrow LiO_2^* \tag{5.2}$$

$$2LiO_2^* \rightarrow Li_2O_2 + O_2;\ \Delta G_c = \text{-}30.86\ \text{kcal} \tag{5.3}$$

or

$$LiO_2^* + Li^+ + e^- \rightarrow Li_2O_2;\ \Delta G_{ec} = \text{-}83.66\ \text{kcal} \tag{5.4}$$

After the surface adsorbed LiO_2^* is generated through (5.1) and (5.2), Li_2O_2 can be produced through either a chemical disproportionation (5.3) process or an electrochemical reduction (5.4) process. Although pathway (5.4) is more thermodynamically favored, the Li_2O_2 formation pathway can be tweaked based on the interaction of LiO_2^* to cathode surfaces. If the absorptivity of LiO_2^* to the cathode is low, LiO_2^* can migrate into the electrolyte to form solvated $LiO_{2(sol)}$, which undergoes the chemical disproportionation process to generate Li_2O_2 via (5.3). When Li_2O_2 is supersaturated in electrolyte, Li_2O_2 crystallites precipitate on cathode surfaces at nucleation sites and grow into large toroids via a process known as the

solution growth pathway[4]. Otherwise, the LiO_2^* on cathode surfaces can directly convert to Li_2O_2 through the electrochemical reduction (5.4) via a process known as the surface growth pathway, which forms Li_2O_2 precipitate in a conformal layer morphology on cathode surfaces. The two different Li_2O_2 formation pathways can affect the morphology and crystallinity of the deposited Li_2O_2 and capacity performance of the battery. More importantly, the morphology and crystallinity of Li_2O_2 have a significant impact on the kinetics of the oxygen evolution reactions (OER) during charge. Therefore, the pathways will also indirectly influence the cyclability of the battery[3].

As Li_2O_2 forms as a solid discharge product on the cathode, the insulating nature of Li_2O_2[5] leads to gradual electrical passivation of cathode surfaces, preventing further discharge and leading to a sharp drop in discharge potential below 2.0 V *vs.* Li/Li^+ (the "sudden death" of the battery). In order to maximize Li_2O_2 production and discharge capacity, the cathode passivation should be delayed as much as possible. To date, the solution growth pathway has been mostly studied because it enables the Li_2O_2 to grow into large toroids away from cathode surfaces, allowing high Li_2O_2 production before cathode surfaces are fully passivated[6]. For example, Liu et al.[7] developed a hierarchical $NiCo_2O_4$ nanowire array on carbon cloth cathode, Li_2O_2 as large as 1 μm in diameter were preferentially grown on the tips of the nanowires and away from carbon surface so as to delay cathode passivation. High donor number (DN) electrolytes (e.g., DMSO, DMA[8–10]) or protic additives (e.g., H_2O, alcohols[11–13]) are introduced to enhance the solvation of LiO_2 to promote this solution growth pathway further, but these electrolytes and additives also encourage parasitic reactions[14]. On the other hand, efficient decomposition of the Li_2O_2 toroids during OER associated with the battery charge and overall cyclability is challenging, because it is difficult to decompose the

large and insulating Li_2O_2 toroids located away from the electrochemically active cathode surfaces[14]. Soluble oxidation mediators such as 2,2,6,6-tetramethylpiperidinyloxyl (TEMPO)[15,16] and LiI[17,18] are proposed to decompose Li_2O_2 from the electrolyte and reduce the overpotential, but they can attack Li anode, which contributes to poor long-term stability[14].

In contrast, the conformal Li_2O_2 layer morphology formed via the surface growth pathway is advantageous for OER, because it is in close contact with cathode surfaces[4] and can be facilely decomposed during charge[19]. Cathode materials with high O_2 (LiO_2) adsorbability are required to drive Li_2O_2 formation to the surface growth pathway[20]. Unfortunately, to meet this requirement, precious metal or their oxides (e.g., Pd[21], Au[22], RuO_2[23], etc.) are usually needed, which will increase the price of the batteries and hinder their mass use. More importantly, Li_2O_2 is a wide band gap insulator[5], which leads to the formation of Li_2O_2 layer with a limited thickness of 5-10 nm[24,25]. Beyond this thickness, electrons cannot tunnel through the insulating Li_2O_2 layer to sustain electrochemistry, leading to rapid cathode passivation, low Li_2O_2 production and small discharge capacity. Therefore, surface growth pathway is generally considered unfavourable[26] and cathodes based on this pathway are scarce. In order to improve discharge capacity, efforts have been made to improve the conductivity of Li_2O_2 so more Li_2O_2 can be produced before the cathode is fully passivated. Yilmaz et al.[23] reported that the Li_2O_2 layer formed on a RuO_2 decorated CNT cathode was partially noncrystalline. The defects in noncrystalline Li_2O_2 can significantly improve the conductivity of the layer, allowing it to grow as thick as 20 nm before cathode passivation, improving Li_2O_2 production. It is hypothesized increasing the amorphous portion of the Li_2O_2 layer will further improve its conductivity, which promotes Li_2O_2 production and

enhances discharge capacity of the battery. So far, amorphous Li_2O_2 formation on cathode surfaces via a surface growth pathway has not been reported.

Here, we report a novel macroporous $NiCo_2O_4$@CNT cathode for non-aqueous Li-O_2 battery. The freestanding cathode was fabricated via a vacuum filtration-assisted self-assembly of the $NiCo_2O_4$@CNT nanotubes with different sized polystyrene microspheres as templates for macropore generation. The influence of $NiCo_2O_4$ (NCO) nanoparticles on the formation pathways and the morphologies of Li_2O_2 discharge product was investigated by comparing the CNT cathodes with and without NCO nanoparticles grown on CNT surfaces. The influence of the NCO nanoparticles on the crystallinity of the Li_2O_2 formed via the surface growth pathway was explored by tweaking the content of NCO nanoparticles on CNT surfaces. The macroporous NCO@CNT cathodes are found to promote the formation of a thick amorphous Li_2O_2 layer on cathode surfaces. The mechanism for forming this thick amorphous layer is proposed, and the implications of this layer on the ORR and OER performance of battery are discussed in detail. The effect of the macropores on the discharge capacity of the battery is also analyzed.

Experimental

Material. All regents were of analytical grade and were used as received without further purification**.** Carbon nanotubes (CNT, multi-walled) were supplied by Chengdu Organic Chemicals Co., Ltd. Styrene, potassium persulfate, sodium dodecyl sulfate (SDS), cobalt nitrate hexahydrate ($Co(NO_3)_2 \cdot 6H_2O$), nickel nitrate hexahydrate ($Ni(NO_3)_2 \cdot 6H_2O$), acetone and toluene were purchased from Sigma-Aldrich. Urea, nitric acid (69 %) and sodium hydroxide were obtained from Chem-Supply. Nylon filter membrane (0.45 μm pore size, 47

mm diameter), cellulose filter membrane (0.45 μm pore size, 47 mm diameter) and glass fiber membrane (Grade GF/F) were from Whatman. Lithium foil was supplied by China Energy Lithium Co., Ltd. 1M lithium bis(trifluoromethanesulfonyl)imide (LiTFSI) in tetraethylene glycol dimethyl ether (TEGDME) was from Suzhou Qianmin Chemical Reagent Co., Ltd. Ultra-high purity (99.999%) O_2 was acquired from Coregas.

Material Synthesis. CNT was first treated with nitric acid. 200 mg CNT were suspended in 60 mL nitric acid (69 %) and refluxed for 3 h. The suspension was cooled to room temperature, diluted with 500 mL DI water and filtered through a nylon membrane on a vacuum filtration apparatus. The filter cake was further washed with a large quantity of DI water until the filtrate reaching pH-neutral and dried at 60 ℃ overnight. Polystyrene (PS) microspheres with diameters of 170 and 410 nm were synthesized according to a previous report[27] and labeled as PS170 and PS410.

The NCO@CNT was synthesized according to a previous method with modification[28]. 25 mg CNT was dispersed in 30 mL DI water by sonication. 1 mmol $Co(NO_3)_2 \cdot 6H_2O$, 0.5 mmol $Ni(NO_3)_2 \cdot 6H_2O$ and 6 mmol urea were added to the above dispersion, stirred for 15 min at room temperature, and transferred to a Teflon-lined autoclave. The autoclave was heated to 95 ℃ and maintained at that temperature for 10 h before naturally cooling down to room temperature. The precipitate was collected, washed with water three times and dried at 60 ℃ overnight. The dried product was heated to 300 ℃ in an open-ended tube furnace at a slow heating rate of 2 ℃ min^{-1} and maintained for 3 h to obtain the NCO@CNT. Another sample with lower NCO loading (labeled as LNCO@CNT) was prepared by decreasing metal salt feeds, i.e., 0.10 mmol $Co(NO_3)_2 \cdot 6H_2O$, 0.05 mmol $Ni(NO_3)_2 \cdot 6H_2O$ and 0.60 mmol urea.

The freestanding macroporous NCO@CNT cathodes (M-NCO@CNT) were fabricated via

a vacuum filtration method followed by PS template removal. To fabricate the M-NCO@CNT-170 cathode with PS170 as a template, 15 mg NCO@CNT, 10 mg PS170, and 100 mg SDS were dispersed in 20 mL DI water and sonicated for 1 h. The mixture was filtered through a cellulose membrane on a vacuum filtration apparatus and washed with DI water. The obtained film was punched into a 1 cm circular disk and treated with acetone followed by toluene to remove the cellulose membrane and PS microspheres. The obtained disk was dried in an oven at 60 ℃ and used as a freestanding cathode directly. In order to investigate the effect of NCO loading, macroporous LNCO@CNT cathode with PS170 as a template (M-LNCO@CNT-170) and macroporous CNT cathode with PS170 as a template (M-CNT-170) were fabricated with LNCO@CNT (6 mg) and CNT (5 mg) instead. The amount of LNCO@CNT and CNT were adjusted, so the carbon (CNT) content in all M-NCO@CNT-170, M-LNCO@CNT-170 and M-CNT-170 cathodes remained the same. In order to investigate the effect of pore size, M-NCO@CNT-410 and M-NCO@CNT-0 cathodes were fabricated with PS410 template and no template instead.

Characterization. Scanning electron microscopy (SEM) images were acquired on an FEI Quanta 450 operating at an accelerating voltage of 30 kV. Transmission electron microscopy (TEM) images were acquired on a Tecnai G2 Spirit operating at an accelerating voltage of 120 kV. X-ray diffraction (XRD) measurements were conducted on a Rigaku Miniflex 600 instrument using a Cu Kα radiation at a scanning rate of 1 ° min^{-1}. X-ray photoelectron spectroscopy (XPS) measurements were conducted on a Thermo Fisher Scientific K-Alpha^{+} Spectrometer using a monochromatic Al Kα radiation at 12 kV.

Electrochemical measurements. The coin-type battery was assembled in an argon-filled glove box, using an as-prepared cathode, a Li foil anode, a glass fiber membrane separate, a

1 M LiTFSI in TEGDME electrolyte and a Ni foam current collector. The assembled battery was transferred to a glass chamber and purged with ultra-high purity O_2 for 15 min. The galvanostatic discharge-charge tests were performed on a Neware battery testing system. In order to perform *ex-situ* characterizations of cathodes, coin-type batteries were disassembled in an argon-filled glove box. The extracted cathodes were soaked in TEGDME for 24 h and pat dried with filter paper. These cathodes were kept in argon at all times until tests were performed.

Results and Discussion

Material Synthesis and Characterization

NCO@CNT was synthesized by *in-situ* growth of NCO nanoparticles on CNT surfaces through a simple hydrothermal method followed by calcination. The crystal structures of CNT and NCO@CNT were characterized by XRD as displayed in Figure 5.1. The strong peak at 2θ of 26.0° in CNT can be indexed to the (002) plane of carbon and the sharpness of this peak suggests the graphitic structure of CNT is preserved after acidic treatment. The remaining peaks at 2θs of 43.7° and 53.9° can be ascribed to the (100) and (004) planes of carbon[29]. For NCO@CNT, peaks at 2θs of 19.0°, 31.2°, 36.8°, 38.5°, 44.8°, 59.0° and 64.6° can be indexed to the (111), (220), (311), (222), (400), (511) and (440) crystal planes of the spinel phase $NiCo_2O_4$ (JCPDS #73-1702). The CNT 2θ peak shifts to 25.0° and broadens, which implies the crystallinity of CNT slightly decreases after calcination[30].

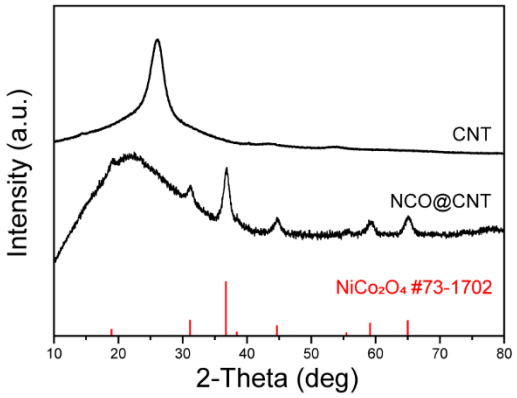

Figure 5.1. The XRD patterns of CNT and NCO@CNT.

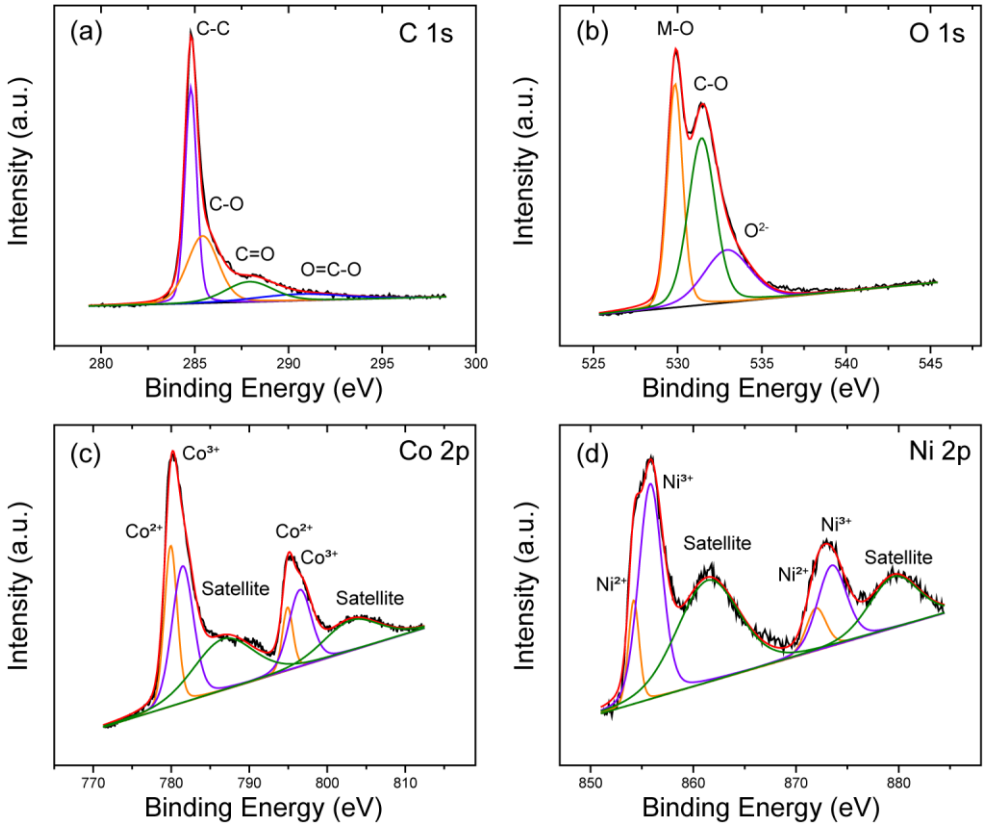

Figure 5.2. XPS spectra of NCO@CNT.

Figure 5.2 illustrates the XPS spectra of C 1s, O 1s, Co 2p and Ni 2p elements in NCO@CNT. The C 1s spectrum shows four peaks at 284.8, 285.4, 287.9 and 290.6 eV corresponding to the C-C, C-O, C=O, and O=C-O bonds[28]. The O 1s spectrum displays the metal-oxygen bond at 529.9 eV and the C-O bond at 531.4 eV. The peak at 532.9 eV can be attributed to defect sites with abundant low oxygen coordination species, indicating the surfaces of NCO@CNT are rich in oxygen defects[31,32]. The Co 2p spectrum is fitted with the spin-orbit doublet peaks of Co^{2+}, Co^{3+} and two shakeup satellites. The peaks at 779.9 and 794.9 eV are indexed to the doublet of Co^{2+} while peaks at 781.5 and 796.5 eV are indexed to Co^{3+}. Two satellite peaks of Co can be observed at 786.7 and 803.1 eV[32,33]. The Ni 2p spectrum shows two spin-orbit doublet peaks for Ni^{2+} at 854.2 and 871.9 eV and Ni^{3+} at 855.8 and 873.5 eV, accompanied by two satellite peaks at 861.4 and 879.5 eV[32,33]. The XPS results confirm the formation of spinel $NiCo_2O_4$ on CNT with rich Ni^{2+}/Ni^{3+} and Co^{2+}/Co^{3+} redox couples.

Figure S5.1 displays that the CNT is 10-20 nm in diameter and several microns in length. The SEM image of NCO@CNT (Figure 5.3a) shows the diameter increases to 20-40 nm, as the result of the uniform deposition of NCO on CNT surfaces. The TEM image (Figure 5.3b) reveals that the NCO nanoparticles of ~10 nm cover the surfaces of CNT adequately. For LNCO@CNT with lower NCO loading, its diameter does not increase as significantly as that of NCO@CNT (Figure 5.3c), and NCO nanoparticles are sparsely distributed on the surface of CNTs (Figure 5.3d). The carboxylic, carbonyl and hydroxyl groups on the acidic treated CNT offer numerous nucleation sites for NCO precursor (Ni and Co mixed hydroxide) to grow into fine nanoparticles without aggregation[34]. The freestanding cathodes were fabricated via a vacuum filtration-assisted self-assembly method. PS microspheres (Figure S5.2) were used as sacrificial templates to generate macropores with desired dimensions.

The SEM image of the M-CNT-170 (Figure 5.4a) shows that after the removal of PS microspheres, interconnected macropores of ~170 nm in size are densely distributed on the highly entangled nanotube framework. It also shows small mesopores (< 20 nm) between crisscrossing nanotubes that are typically presented in CNT films assembled with the aid of vacuum filtration[35]. For M-NCO@CNT-170 (Figure 5.4b), the macropores are less spherical and ordered, because NCO@CNT is more rigid than CNT. Nevertheless, NCO@CNT is long and flexible enough to form an intertwined framework with macropores of 100-200 nm in size together with small mesopores between nanotubes. The M-LNCO@CNT-170 cathode with lower loading of NCO displays a similar macroporous structure to that of M-NCO@CNT-170 (Figure 5.4c).

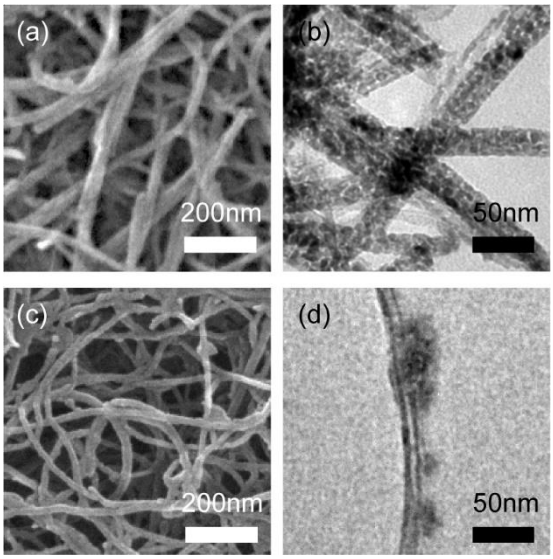

Figure 5.3. (a) SEM and (b) TEM images of NCO@CNT; (c) SEM and (d) TEM images of LNCO@CNT.

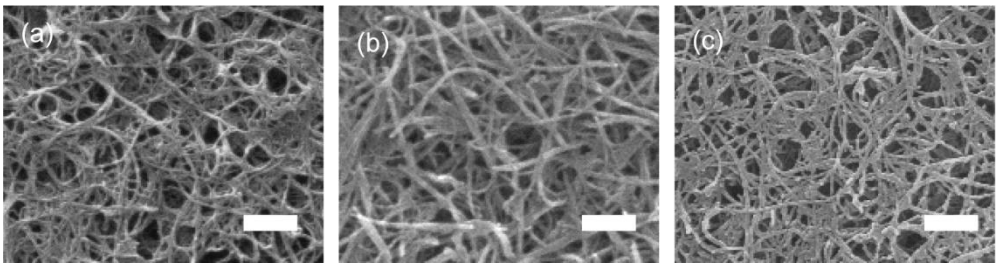

Figure 5.4. SEM images of the pristine (a) M-CNT-170, (b) M-NCO@CNT-170, and (c) M-LNCO@CNT-170 cathodes, scale bars indicate 200 nm.

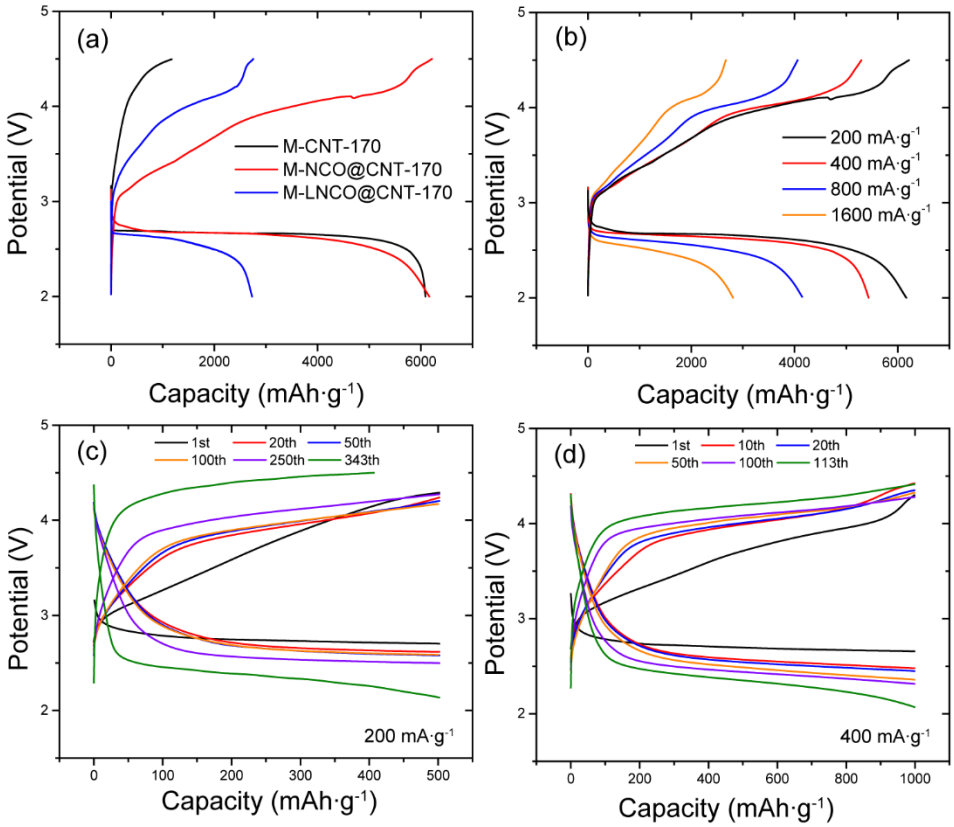

Figure 5.5. (a) The discharge-charge profiles of M-CNT-170, M-NCO@CNT-170 and M-LNCO@CNT-170 at a current density of 200 mA g^{-1}; (b) the rate performance of M-NCO@CNT-170 at current densities of 200, 400, 800 and 1600 mA g^{-1}; the cycling performance of M-NCO@CNT-170 (c) at a current density of 200 mA g^{-1} and limited capacity of 500 mAh g^{-1} and (d) at 400 mA g^{-1} and limited capacity of 1000 mAh g^{-1}.

Effect of NCO on Li_2O_2 Formation

In order to evaluate the contribution of NCO to the battery performance, the galvanostatic discharge-charge profiles of M-CNT-170, M-NCO@CNT-170 and M-LNCO@CNT-170 cathodes were measured at a current density of 200 mA g^{-1} within the potential window of 2.0-4.5 V (*vs.* Li/Li^+), and the results are shown in Figure 5.5a. During first discharge, the specific capacities of M-CNT-170, M-NCO@CNT-170 and M-LNCO@CNT-170 are 6089, 6165 and 2732 mAh g^{-1}. Intriguingly, while M-NCO@CNT-170 delivers a similar discharge capacity to that of M-CNT-170, the low NCO loading in M-LNCO@CNT-170 exhibits a significant negative impact on discharge capacity. In addition, M-CNT-170 displays a nearly constant potential plateau followed by a sharp, faster-than-exponential, potential drop by the end of discharge, but both M-NCO@CNT-170 and M-LNCO@CNT-170 display a sloping curve. The drastically different discharge curves suggest that the addition of NCO may fundamentally change the ORR pathway during discharge. For the recharge, the M-CNT-170 cathode can only recover ~1000 mAh g^{-1}, while M-NCO@CNT-170 and M-LNCO@CNT-170 can fully recover their discharge capacities with a charge potential of 3.9 and 4.0V. A small addition of NCO in M-LNCO@CNT-170 cathode can significantly reduce charge potential and improve OER activity in comparison to the M-CNT-170 cathode, while the higher loading M-NCO@CNT-170 shows overall the highest OER activity.

Figure 5.5b shows the rate performance of M-NCO@CNT-170. The battery capacity decreases as the current density increases. At an increased current density of 400 mA g^{-1}, the capacity sees a marginal reduction from 6165 mAh g^{-1} at 200 mA g^{-1} to 5435 mAh g^{-1}. At a high current density of 800 mA g^{-1}, the discharge capacity is 4134 mA g^{-1}, and even at the super high current density of 1600 mA g^{-1}, the cathode can still retain a capacity of 2809

mAh g^{-1}, indicating the superior rate performance of M-NCO@CNT-170. Figure 5.5c displays the cycling performance of M-NCO@CNT-170 at a current density of 200 mA g^{-1} and limited capacity of 500 mAh g^{-1}. M-NCO@CNT-170 shows small polarization with a discharge overpotential of 0.23 V and a charge overpotential of 0.77 V during the initial cycle. The battery shows minimal degradation over the first 250 cycles and fails after 343 cycles. In contrast, M-CNT-170 cathode maintains 68 cycles (Figure S5.3), and M-LNCO@CNT-170 cathode can maintain 96 cycles (Figure S5.4). Compared to other NCO-based cathodes reported in previous literature (Table S5.1), the M-NCO@CNT-170 cathode shows high capacity and outstanding cycling performance, the latter of which is superior to previous cathodic NCO materials. The excellent stability of M-NCO@CNT-170 is further demonstrated by cycling the cathode at a higher current density of 400 mA g^{-1} at a larger cut-off capacity of 1000 mAh g^{-1}. As shown in Figure 5.5d, the cathode is stable for the first 100 cycles and fails after 113 cycles.

In order to further understand the influences of NCO to battery performance, the batteries using M-CNT-170, M-NCO@CNT-170 and M-LNCO@CNT-170 cathodes were dissembled after the first deep discharge to 2.0 V so that the cathodes can be analyzed via *ex-situ* characterizations. Figure 5.6a shows that on the fully discharged M-CNT-170, the characteristic Li_2O_2 toroids of ~80 nm in thickness and ~300 nm in diameter can be clearly observed, and the macropores in M-CNT-170 are filled by these toroids. For the discharged M-NCO@CNT-170 cathode, no large Li_2O_2 toroids can be observed (Figures 5.6b and S5.5a). Instead, Li_2O_2 is homogenously deposited in a conformal layer morphology with a thickness of up to ~50 nm. Most of the macropores on the cathode surfaces are filled by Li_2O_2. Moreover, the macroporous structure of the M-NCO@CNT-170 framework is

preserved after Li_2O_2 formation, as demonstrated by the SEM image of fully recharged M-NCO@CNT-170 (Figure S5.6). For the discharged M-LNCO@CNT-170 cathode, Li_2O_2 forms a thin layer of less than 10 nm in thickness, which fills in a much smaller percentage of the macropores on the cathode, compared to that of M-NCO@CNT-170 (Figures 5.6c and S5.5b). The crystal structures of discharged M-CNT-170, M-NCO@CNT-170, and M-LNCO@CNT-170 cathodes were further examined by XRD (Figure 5.6d). The peaks at 2θs of 32.9, 35.0° and 58.7° in the discharged M-CNT-170 cathode can be ascribed to the (100), (101), and (110) crystal planes of Li_2O_2 (JCPDS # 09-0355), which confirms the formation of well-crystalline Li_2O_2 on M-CNT-170. For the discharged M-NCO@CNT-170 cathode, however, no visible peaks for crystalline Li_2O_2 can be observed, indicating the formation of amorphous Li_2O_2. For the discharged M-LNCO@CNT-170 cathode, a major peak at 2θ of 32.9° can be indexed to the (100) crystal plane of Li_2O_2, which reveals the discharge product on M-LNCO@CNT-170 possesses reduced crystallinity compared to that on M-CNT-170. These results indicate that the addition of NCO onto CNT can drastically change the morphology of deposited Li_2O_2 from the typical toroid morphology to a layer morphology. The content of NCO on CNT also plays an essential role to influence the crystallinity of the formed Li_2O_2. High NCO contents on CNT promote the formation of amorphous Li_2O_2 together with the increase in the thickness of the Li_2O_2 layer.

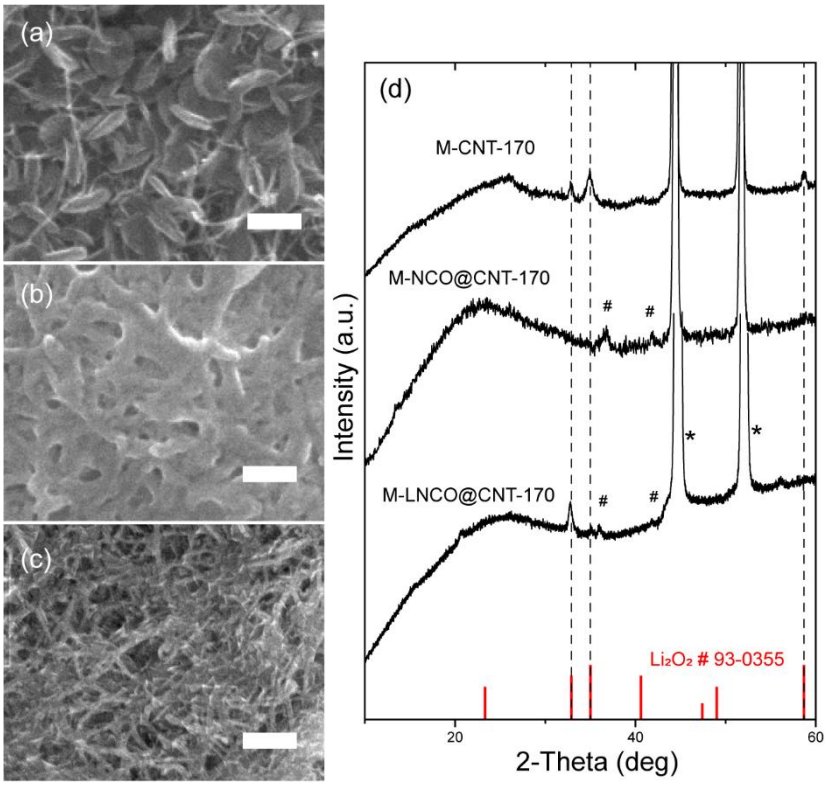

Figure 5.6. The *ex-situ* SEM images of the (a) M-CNT-170, (b) M-NCO@CNT-170 and (c) M-LNCO@CNT-170 after the first full discharge, the scale bars indicate 200 nm; (d) their corresponding XRD patterns (# indicates the peaks of $NiCo_2O_4$ and * indicates the peak of Ni foam current collector)

The morphological analysis of the deposited Li_2O_2 suggests that on M-CNT-170, the Li_2O_2 toroids are formed via a solution growth pathway, while the Li_2O_2 layers on M-NCO@CNT-170 and M-LNCO@CNT-170 cathodes are produced via a surface growth pathway. The different shapes of discharge curves further support their distinct pathways. For M-CNT-170, the growth of Li_2O_2 toroids does not passivate cathode surfaces, so the plateau is constant. Eventually, the macropores of the cathode are filled by large Li_2O_2 toroids, and cathode surfaces are blocked, which leads to a sharp drop in potential[36]. On the other hand, for M-NCO@CNT-170 and M-LNCO@CNT-170, the ohmic overpotential gradually increases as the electron transfer through the deposited Li_2O_2 layer becomes increasingly difficult, resulting in a sloping discharge curve[36]. The different pathways on these cathodes can be

attributed to the different O_2 (LiO_2) absorptivity of cathode surfaces. For M-CNT-170, CNT is known to show a weak O_2 (LiO_2) absorptivity[26]. LiO_2^* generated through reactions (5.1) and (5.2) can readily migrate into the electrolyte and preferably form Li_2O_2 toroids via the solution growth pathway. In contrast, the surfaces of NCO display strong O_2 (LiO_2) adsorption affinity[37] because they are oxygen-deficient[38,39]. The surface adsorbed LiO_2^* on the surfaces of M-NCO@CNT-170 and M-LNCO@CNT-170 can directly undergo surface growth pathway to produce Li_2O_2 layers.

The oxygen-deficient surfaces of NCO can promote the growth of oxygen-rich and lithium-deficient species ($Li_{2-x}O_2$)[23]. The presence of $Li_{2-x}O_2$ introduces defects in the Li_2O_2 layer, leading to reduced crystallinity[23]. In addition, the crystallinity of the deposited Li_2O_2 is related to how LiO_2^* is arranged on the initial adsorption sites[40], which also act as nucleation sites for Li_2O_2 growth. LiO_2^* on the defect-rich NCO surfaces is irregularly arranged, which leads to the growth of Li_2O_2 layer with poor crystallinity. For M-CNT-170, the weak O_2 (LiO_2) absorptivity of CNT surfaces drives the formation of large Li_2O_2 toroids via the solution growth pathway. For M-NCO@CNT-170, the surfaces of the cathode are entirely covered by oxygen-deficient NCO and adsorbs irregularly arranged LiO_2^*, which also promotes the growth of $Li_{2-x}O_2$. Consequently, the overall crystallinity of Li_2O_2 layer formed on this cathode is significantly reduced so as it is below the detection limit of XRD. For M-LNCO@CNT-170, the surfaces consist of a small amount of NCO and a large amount of CNT. Although Li_2O_2 near the NCO nanoparticles shows poor crystallinity, it only constitutes a small portion. The CNT surfaces are relatively well defined, so LiO_2^* on CNT surfaces are orderly arranged[40], this, together with the weak O_2 (LiO_2) absorptivity of CNT surfaces, results in the growth of crystalline Li_2O_2. The overall Li_2O_2 layer on M-

LNCO@CNT-170 shows slightly reduced crystallinity. The detailed mechanisms on the Li_2O_2 formations on the three different cathodes are summarized in Figure 5.7.

The formation of amorphous Li_2O_2 layer can significantly enhance the OER and cycling performance. Compared to large toroids from the solution growth pathway, the layer morphology is in close contact with cathode surfaces, which improves the kinetics during OER[4]. In addition, the amorphous Li_2O_2 can be decomposed with a much lower potential than its crystalline counterpart[41], which reduces the charge overpotential and improves the long-term stability of the battery. The superior cycling performance of M-NCO@CNT-170 can be ascribed to a combination of the layer morphology and amorphous nature of Li_2O_2 induced by NCO nanoparticles on CNT surfaces.

Moreover, the amorphous Li_2O_2 shows improved charge transport properties than its crystalline counterpart[42,43], therefore, it can also be beneficial for ORR. For M-NCO@CNT-170, Li_2O_2 can grow into a much thicker layer (~ 50 nm) than that on M-LNCO@CNT-170 (~ 10nm), before the cathode is fully passivated. Notably, this Li_2O_2 layer on M-NCO@CNT-170 is also much thicker than those from previous reports (< 20 nm)[23,44]. Evidently, the thickness of the Li_2O_2 layer also affects the discharge capacity of the cathodes. The insoluble Li_2O_2 is accommodated in the macropores of cathodes. The discharge capacity of the cathode with a certain pore volume is determined by how much of the pores in the cathode is filled by Li_2O_2, i.e., the utilization ratio of the porous cathode. Because the Li_2O_2 layer on M-NCO@CNT-170 is much thicker compared to that on M-LNCO@CNT-170, the M-NCO@CNT-170 cathode shows a higher cathode utilization ratio, which attributes to its improved capacity performance. Conventionally, the surface growth pathway for Li_2O_2 is much less favorable than the solution growth pathway, because the thin Li_2O_2 layer shows a

low cathode utilization ratio. In order to increase the cathode utilization ratio for Li_2O_2 layer with a thickness of 5-10 nm, an ultra-porous cathode with a small pore size (~ 20 nm) and ultra-high surface areas is required. The development of such cathode remains challenging, especially considering such small pores can be easily blocked. Conversely, in this work, the M-NCO@CNT-170 cathode with a macropore size of 100-200 nm can accommodate ~ 50 nm thick Li_2O_2 layer with a high cathode utilization ratio. It can even deliver a discharge capacity comparable to that of M-CNT-170 via the solution growth pathway because both M-CNT-170 and M-NCO@CNT-170 cathodes display similarly high cathode utilization ratios. These results have demonstrated that the formation of amorphous and layer-like Li_2O_2 can circumvent the small capacity issue of the surface growth pathway.

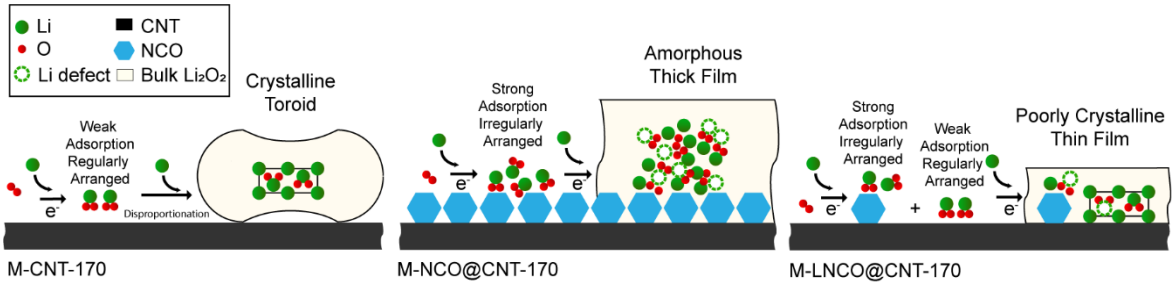

Figure 5.7. The scheme of the Li_2O_2 formation mechanisms on M-CNT-170, M-NCO@CNT-170, and M-LNCO@CNT-170 cathodes.

Effect of Cathode Pore Size

Intuitively, the size of the macropores in the cathode can also influence the cathode utilization ratio. The effect of the macroporous structure on the discharge capacity of the batteries is discussed. The size of the macropores can be adjusted by using different sized PS microspheres. When using larger PS410 microspheres, larger macropores of ~ 400 nm in size are presented in M-NCO@CNT-410 (Figure 5.8a). Without the addition of PS microspheres, the SEM image of M-NCO@CNT-0 (Figure 5.8b) reveals that the cathode is densely packed under the force of vacuum filtration. There are no macropores, and only a small amount of mesopores are present. The SEM image (Figure 5.8c) of the discharged M-NCO@CNT-410 cathode shows that the Li_2O_2 layer cannot fill up the macropores in the cathode with a high utilization ratio. Consequently, the M-NCO@CNT-410 cathode with larger pores shows a reduced capacity of 4834 mAh g^{-1} compared to M-NCO@CNT-170 (6165 mAh g^{-1}) (Figure 5.8e). On the other hand, for the discharged M-NCO@CNT-0, SEM image of the cathode (Figure 5.8d) reveals that it is entirely covered with a formless layer of Li_2O_2 without any pore. Discharge curve (Figure 5.8e) reveals that without any macropores, M-NCO@CNT-0 can only deliver 1221 mAh g^{-1}. The quick surface coverage can block further mass transportation, drastically limiting the overall capacity on M-NCO@CNT-0. Evidently, M-NCO@CNT-170 offers the optimal pore structure that efficiently accommodates the discharge product with a high cathode utilization ratio. The thick Li_2O_2 layer allows cathodes with proper macroporous structures, such as M-NCO@CNT-170, to be facially synthesized to overcome the low capacity issues of the Li_2O_2 formed via surface growth pathway.

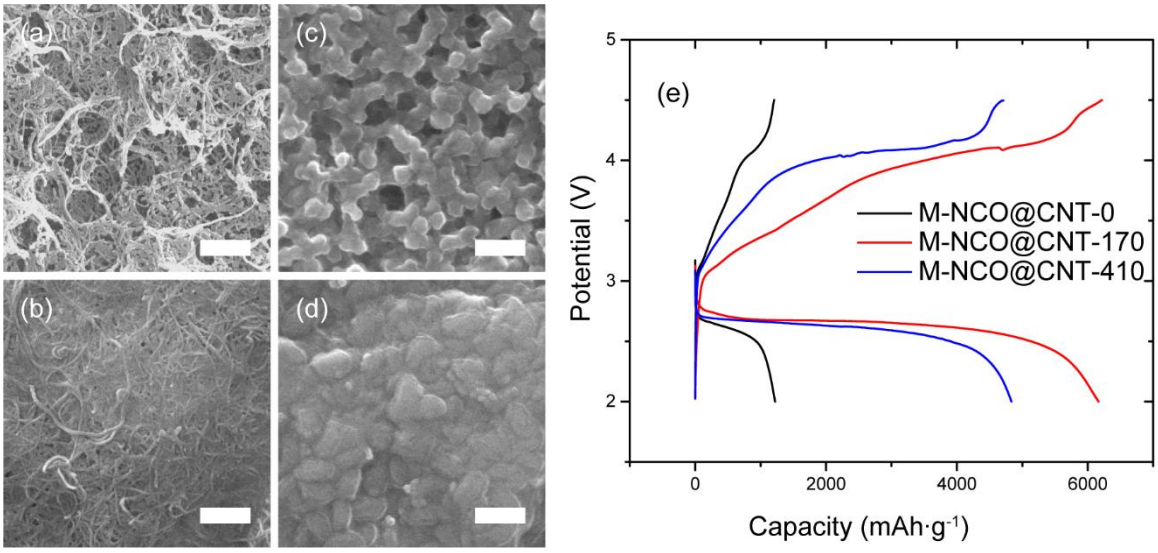

Figure 5.8. The SEM images of the pristine (a) M-NCO@CNT-410 and (b) M-NCO@CNT-0 cathodes; the *ex-situ* SEM images of the (c) M-NCO@CNT-410 and (d) M-NCO@CNT-0 cathodes after the first full discharge, the scale bars indicate 500 nm; (e) the discharge-charge profiles of M-NCO@CNT-410, M-NCO@CNT-170 and M-NCO@CNT-0 at a current density 200 mA g^{-1}.

Conclusion

A non-aqueous Li-O_2 battery using a novel M-NCO@CNT-170 cathode can deliver a capacity of 6165 mAh g^{-1} at 200 mA g^{-1} and excellent cycling performance of 343 cycles at 200 mA g^{-1} and limited capacity of 500 mAh g^{-1}. A unique thick and amorphous Li_2O_2 layer is observed as the discharge product of M-NCO@CNT-170. The oxygen-deficient surfaces of NCO nanoparticles that entirely cover CNT are proposed to promote the formation of amorphous Li_2O_2 layer by adsorbing irregularly arranged LiO_2^*, which grows into defect-rich Li_2O_2 with poor crystallinity. Owing to the improved charge transfer properties of amorphous Li_2O_2, the Li_2O_2 layer can exceed the thickness limit of bulk Li_2O_2 layer (5-10 nm) and grow to a considerably improved thickness of ~50 nm before the cathode is fully passivated. The thick Li_2O_2 layer formation on M-NCO@CNT-170 allows the discharge product to fill the macropores in the cathode with a high utilization ratio, leading to a high

discharge capacity. The amorphous Li_2O_2 layer is in close contact with cathode surfaces and can be facilely decomposed during OER, which attributes to the excellent cycling performance of the M-NCO@CNT-170 cathode. The effect of the pore size structure on the discharge capacity of the batteries is investigated, and the M-NCO@CNT-170 with a macropore size of 100-200 nm is optimal to ensure high cathode utilization ratio. This study has demonstrated that by improving the conductivity of the Li_2O_2 layer in the surface growth pathway, a significantly larger amount of Li_2O_2 can be produced before cathode passivation, which leads to higher discharge capacity. This new strategy can overcome the low capacity issue of the surface growth pathway for future cathode designs of stable and high-capacity non-aqueous Li-O_2 batteries.

Associated Content

Supporting Information

The SEM images of CNT, PS170, PS410, the M-NCO@CNT-170 cathode after a full discharge and charge cycle; the TEM images of discharged M-NCO@CNT-170 and M-LNCO@CNT-170 cathodes; the cycling performance of M-CNT170 and M-LNCO@CNT-170 cathodes.

Acknowledgments

This work was financially supported by the Australian Research Council Discovery Projects DP140104062.

References

(1) Lu, J.; Li, L.; Park, J.-B.; Sun, Y.-K.; Wu, F.; Amine, K. Aprotic and Aqueous Li-O_2 Batteries. *Chem. Rev.* **2014**, *114* (11), 5611–5640.

(2) Li, F.; Zhang, T.; Zhou, H. Challenges of Non-Aqueous Li-O_2 Batteries: Electrolytes, Catalysts, and Anodes. *Energy Environ. Sci.* **2013**, *6* (4), 1125–1141.

(3) Yin, Y.; Gaya, C.; Torayev, A.; Thangavel, V.; Franco, A. A. Impact of Li_2O_2 Particle Size on Li-O_2 Battery Charge Process: Insights from a Multiscale Modeling Perspective. *J. Phys. Chem. Lett.* **2016**, *7* (19), 3897–3902.

(4) Adams, B. D.; Radtke, C.; Black, R.; Trudeau, M. L.; Zaghib, K.; Nazar, L. F. Current Density Dependence of Peroxide Formation in the Li-O_2 Battery and Its Effect on Charge. *Energy Environ. Sci.* **2013**, *6* (6), 1772.

(5) Radin, M. D.; Siegel, D. J. Charge Transport in Lithium Peroxide: Relevance for Rechargeable Metal-Air Batteries. *Energy Environ. Sci.* **2013**, *6* (8), 2370–2379.

(6) Lau, S.; Archer, L. A. Nucleation and Growth of Lithium Peroxide in the Li-O_2 Battery. *Nano Lett.* **2015**, *15* (9), 5995–6002.

(7) Liu, W.-M.; Gao, T.-T.; Yang, Y.; Sun, Q.; Fu, Z.-W. A Hierarchical Three-Dimensional $NiCo_2O_4$ Nanowire Array/Carbon Cloth as an Air Electrode for Nonaqueous Li-Air Batteries. *Phys. Chem. Chem. Phys.* **2013**, *15* (38), 15806–15810.

(8) Xu, D.; Wang, Z.; Xu, J.; Zhang, L.; Zhang, X. Novel DMSO-Based Electrolyte for High Performance Rechargeable Li-O_2 Batteries. *Chem. Commun.* **2012**, *48* (55), 6948–6950.

(9) Walker, W.; Giordani, V.; Uddin, J.; Bryantsev, V. S.; Chase, G. V.; Addison, D. A Rechargeable Li-O_2 Battery Using a Lithium Nitrate/N,N-Dimethylacetamide Electrolyte. *J. Am. Chem. Soc.* **2013**, *135* (6), 2076–2079.

(10) Trahan, M. J.; Mukerjee, S.; Plichta, E. J.; Hendrickson, M. A.; Abraham, K. M. Studies of Li-Air Cells Utilizing Dimethyl Sulfoxide-Based Electrolyte. *J. Electrochem. Soc.* **2013**, *160* (2), A259–A267.

(11) Aetukuri, N. B.; McCloskey, B. D.; García, J. M.; Krupp, L. E.; Viswanathan, V.; Luntz, A. C. Solvating Additives Drive Solution-Mediated Electrochemistry and Enhance Toroid Growth in Non-Aqueous Li-O_2 Batteries. *Nat. Chem.* **2015**, *7* (1), 50–56.

(12) Kwabi, D. G.; Batcho, T. P.; Feng, S.; Giordano, L.; Thompson, C. V.; Shao-Horn, Y. The Effect of Water on Discharge Product Growth and Chemistry in Li-O_2 Batteries. *Phys. Chem. Chem. Phys.* **2016**, *18* (36), 24944–24953.

(13) Gao, X.; Jovanov, Z. P.; Chen, Y.; Johnson, L. R.; Bruce, P. G. Phenol-Catalyzed Discharge in the Aprotic Lithium-Oxygen Battery. *Angew. Chem. Int. Ed.* **2017**, *56* (23), 6539–6543.

(14) Aurbach, D.; McCloskey, B. D.; Nazar, L. F.; Bruce, P. G. Advances in Understanding Mechanisms Underpinning Lithium-Air Batteries. *Nat. Energy* **2016**, *1* (9), 16128.

(15) Bergner, B. J.; Schürmann, A.; Peppler, K.; Garsuch, A.; Janek, J. TEMPO: A Mobile Catalyst for Rechargeable Li-O_2 Batteries. *J. Am. Chem. Soc.* **2014**, *136* (42), 15054–15064.

(16) Bergner, B. J.; Hofmann, C.; Schürmann, A.; Schröder, D.; Peppler, K.; Schreiner, P. R.; Janek, J. Understanding the Fundamentals of Redox Mediators in Li-O_2 Batteries: A Case Study on Nitroxides. *Phys. Chem. Chem. Phys.* **2015**, *17* (47), 31769–31779.

(17) Zhang, T.; Liao, K.; He, P.; Zhou, H. A Self-Defense Redox Mediator for Efficient Lithium-O_2 Batteries. *Energy Environ. Sci.* **2016**, *9* (3), 1024–1030.

(18) Kwak, W.-J.; Hirshberg, D.; Sharon, D.; Shin, H.-J.; Afri, M.; Park, J.-B.; Garsuch, A.; Chesneau, F. F.; Frimer, A. A.; Aurbach, D.; et al. Understanding the Behavior of Li-Oxygen Cells Containing LiI. *J. Mater. Chem. A* **2015**, *3* (16), 8855–8864.

(19) Viswanathan, V.; Nørskov, J. K.; Speidel, A.; Scheffler, R.; Gowda, S.; Luntz, A. C. Li-O_2 Kinetic Overpotentials: Tafel Plots from Experiment and First-Principles Theory. *J. Phys. Chem. Lett.* **2013**, *4* (4), 556–560.

(20) Yang, Y.; Liu, W.; Wu, N.; Wang, X.; Zhang, T.; Chen, L.; Zeng, R.; Wang, Y.; Lu, J.; Fu, L.; et al. Tuning the Morphology of Li_2O_2 by Noble and 3d Metals: A Planar Model Electrode Study for Li-O_2 Battery. *ACS Appl. Mater. Interfaces* **2017**, *9* (23), 19800–19806.

(21) Yang, Y.; Zhang, T.; Wang, X.; Chen, L.; Wu, N.; Liu, W.; Lu, H.; Xiao, L.; Fu, L.; Zhuang, L. Tuning the Morphology and Crystal Structure of Li_2O_2: A Graphene Model Electrode Study for Li-O_2 Battery. *ACS Appl. Mater. Interfaces* **2016**, *8* (33), 21350–21357.

(22) Tu, F.; Hu, J.; Xie, J.; Cao, G.; Zhang, S.; Yang, S. A.; Zhao, X.; Yang, H. Y. Au-Decorated Cracked Carbon Tube Arrays as Binder-Free Catalytic Cathode Enabling Guided Li_2O_2 Inner Growth for High-Performance Li-O_2 Batteries. *Adv. Funct. Mater.* **2016**, *26* (42), 7725–7732.

(23) Yilmaz, E.; Yogi, C.; Yamanaka, K.; Ohta, T.; Byon, H. R. Promoting Formation of Noncrystalline Li_2O_2 in the Li-O_2 Battery with RuO_2 Nanoparticles. *Nano Lett.* **2013**, *13* (10), 4679–4684.

(24) Viswanathan, V.; Thygesen, K. S.; Hummelshøj, J. S.; Nørskov, J. K.; Girishkumar, G.; Mccloskey, B. D.; Luntz, A. C. Electrical Conductivity in Li_2O_2 and Its Role in Determining Capacity Limitations in Non- Aqueous Li-O_2 Batteries. *J. Chem. Phys.* **2011**, *135* (21), 214704.

(25) Wen, R.; Hong, M.; Byon, H. R. In Situ AFM Imaging of Li-O_2 Electrochemical Reaction on Highly Oriented Pyrolytic Graphite with Ether-Based Electrolyte. *J. Am. Chem. Soc.* **2013**, *135* (29), 10870–10876.

(26) Lyu, Z.; Yang, L.; Luan, Y.; Renshaw Wang, X.; Wang, L.; Hu, Z.; Lu, J.; Xiao, S.; Zhang, F.; Wang, X.; et al. Effect of Oxygen Adsorbability on the Control of Li_2O_2 Growth in Li-O_2 Batteries: Implications for Cathode Catalyst Design. *Nano Energy* **2017**, *36*, 68–75.

(27) Gorsd, M. N.; Blanco, M. N.; Pizzio, L. R. Synthesis of Polystyrene Microspheres to

Be Used as Template in the Preparation of Hollow Spherical Materials: Study of the Operative Variables. *Procedia Mater. Sci.* **2012**, *1*, 432–438.

(28) Abouali, S.; Akbari Garakani, M.; Xu, Z.-L.; Kim, J.-K. $NiCo_2O_4$/CNT Nanocomposites as Bi-Functional Electrodes for Li Ion Batteries and Supercapacitors. *Carbon* **2016**, *102*, 262–272.

(29) Chiang, Y.-C.; Lin, W.-H.; Chang, Y.-C. The Influence of Treatment Duration on Multi-Walled Carbon Nanotubes Functionalized by H_2SO_4/HNO_3 Oxidation. *Appl. Surf. Sci.* **2011**, *257* (6), 2401–2410.

(30) Ramoraswi, N. O.; Ndungu, P. G. Photo-Catalytic Properties of TiO_2 Supported on MWCNTs, SBA-15 and Silica-Coated MWCNTs Nanocomposites. *Nanoscale Res. Lett.* **2015**, *10* (1).

(31) Yuan, H.; Li, J.; Yang, W.; Zhuang, Z.; Zhao, Y.; He, L.; Xu, L.; Liao, X.; Zhu, R.; Mai, L. Oxygen Vacancy-Determined Highly Efficient Oxygen Reduction in $NiCo_2O_4$/Hollow Carbon Spheres. *ACS Appl. Mater. Interfaces* **2018**, *10* (19), 16410–16417.

(32) Ko, T.-H.; Devarayan, K.; Seo, M.-K.; Kim, H.-Y.; Kim, B.-S. Facile Synthesis of Core/Shell-like $NiCo_2O_4$-Decorated MWCNTs and Its Excellent Electrocatalytic Activity for Methanol Oxidation. *Sci. Rep.* **2016**, *6* (1), 20313.

(33) Zheng, Y.; Lin, Z.; Chen, W.; Liang, B.; Du, H.; Yang, R.; He, X.; Tang, Z.; Gui, X. Flexible, Sandwich-like CNTs/$NiCo_2O_4$ Hybrid Paper Electrodes for All-Solid State Supercapacitors. *J Mater Chem A* **2017**, *5* (12), 5886–5894.

(34) Zhuo, L.; Wu, Y.; Ming, J.; Wang, L.; Yu, Y.; Zhang, X.; Zhao, F. Facile Synthesis of a Co_3O_4-Carbon Nanotube Composite and Its Superior Performance as an Anode Material for Li-Ion Batteries. *J. Mater. Chem. A* **2012**, *1* (4), 1141–1147.

(35) Whitby, R. L. D.; Fukuda, T.; Maekawa, T.; James, S. L.; Mikhalovsky, S. V. Geometric Control and Tuneable Pore Size Distribution of Buckypaper and Buckydiscs. *Carbon* **2008**, *46* (6), 949–956.

(36) Mahne, N.; Fontaine, O.; Thotiyl, M. O.; Wilkening, M.; Freunberger, S. A. Mechanism and Performance of Lithium-Oxygen Batteries - a Perspective. *Chem. Sci.* **2017**, *8* (10), 6716–6729.

(37) Cheng, F.; Shen, J.; Peng, B.; Pan, Y.; Tao, Z.; Chen, J. Rapid Room-Temperature Synthesis of Nanocrystalline Spinels as Oxygen Reduction and Evolution Electrocatalysts. *Nat. Chem.* **2011**, *3* (1), 79–84.

(38) Shi, X.; Bernasek, S. L.; Selloni, A. Formation, Electronic Structure, and Defects of Ni Substituted Spinel Cobalt Oxide: A DFT+U Study. *J. Phys. Chem. C* **2016**, *120* (27), 14892–14898.

(39) Shi, X.; Bernasek, S. L.; Selloni, A. Oxygen Deficiency and Reactivity of Spinel $NiCo_2O_4$ (001) Surfaces. *J. Phys. Chem. C* **2017**, *121* (7), 3929–3937.

(40) Wong, R. A.; Dutta, A.; Yang, C.; Yamanaka, K.; Ohta, T.; Nakao, A.; Waki, K.; Byon, H. R. Structurally Tuning Li_2O_2 by Controlling the Surface Properties of Carbon

Electrodes: Implications for Li-O_2 Batteries. *Chem. Mater.* **2016**, *28* (21), 8006–8015.

(41) Ganapathy, S.; Adams, B. D.; Stenou, G.; Anastasaki, M. S.; Goubitz, K.; Miao, X.-F.; Nazar, L. F.; Wagemaker, M. Nature of Li_2O_2 Oxidation in a Li-O_2 Battery Revealed by Operando X-Ray Diffraction. *J. Am. Chem. Soc.* **2014**, *136* (46), 16335–16344.

(42) Tian, F.; Radin, M. D.; Siegel, D. J. Enhanced Charge Transport in Amorphous Li_2O_2. *Chem. Mater.* **2014**, *26* (9), 2952–2959.

(43) Zhang, Y.; Cui, Q.; Zhang, X.; McKee, W. C.; Xu, Y.; Ling, S.; Li, H.; Zhong, G.; Yang, Y.; Peng, Z. Amorphous Li_2O_2: Chemical Synthesis and Electrochemical Properties. *Angew. Chem. Int. Ed.* **2016**, *55* (36), 10717–10721.

(44) Huang, J.; Zhang, B.; Bai, Z.; Guo, R.; Xu, Z.-L.; Sadighi, Z.; Qin, L.; Zhang, T.-Y.; Chen, G.; Huang, B.; et al. Anomalous Enhancement of Li-O_2 Battery Performance with Li_2O_2 Films Assisted by $NiFeO_x$ Nanofiber Catalysts: Insights into Morphology Control. *Adv. Funct. Mater.* **2016**, *26* (45), 8290–8299.

Table of Content

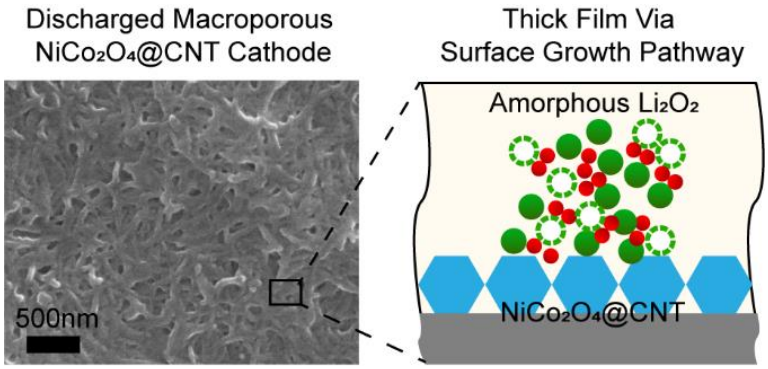

Supporting information

Controlling the Morphology and Crystallinity of Li_2O_2 with Macroporous $NiCo_2O_4$@CNT Cathode for High-Performance Li-O_2 Battery

Heng Wang,[†] Qi Bi,[†] Haihui Wang,[*,†,‡] Sheng Dai [*,†,§]

† School of Chemical Engineering and Advanced Materials, the University of Adelaide, Adelaide, South Australia 5005, Australia

‡ School of Chemistry & Chemical Engineering, South China University of Technology, 381 Wushan Road, Guangzhou 510640, China

§ Department of Chemical Engineering, Brunel University London, Uxbridge, UB8 3PH, United Kingdom

Corresponding author

*E-mail: hhwang@scut.edu.cn

*E-mail: s.dai@adelaide.edu.au

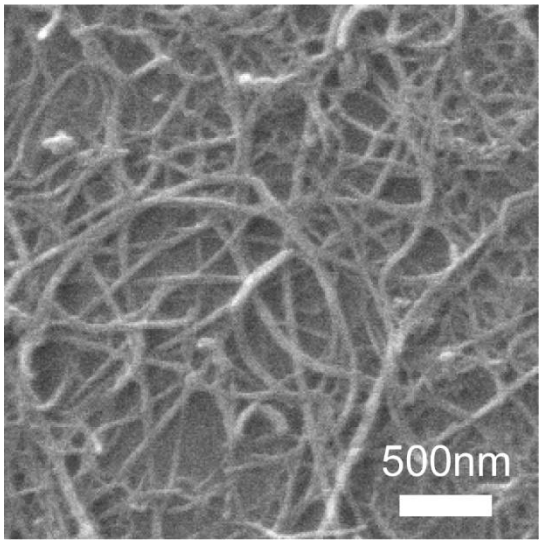

Figure S5.1. The SEM image of CNT after being treated with nitric acid.

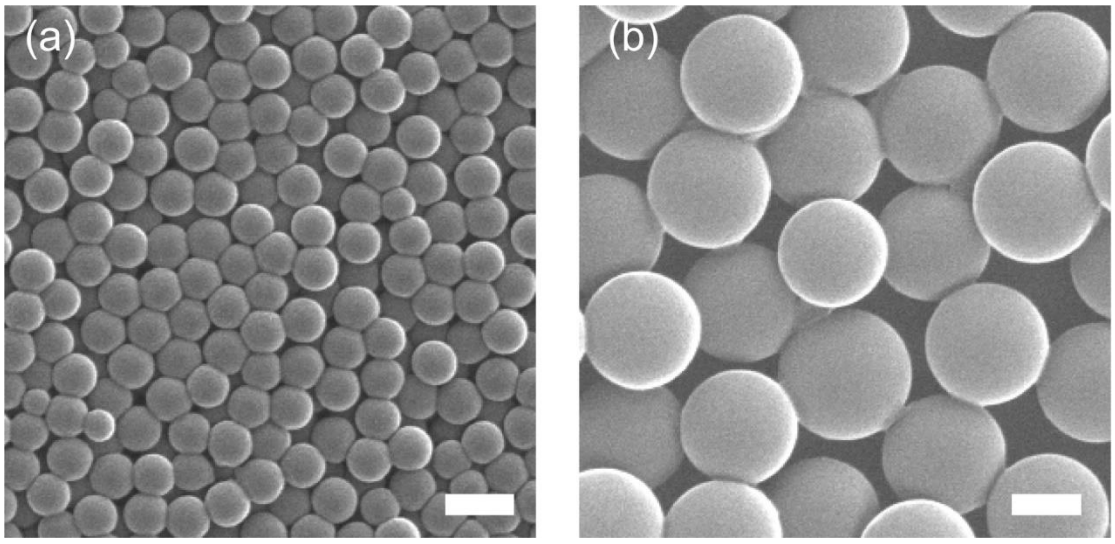

Figure S5.2. The SEM images of (a) PS170 and (b) PS410 microspheres, scale bars indicate 200 nm.

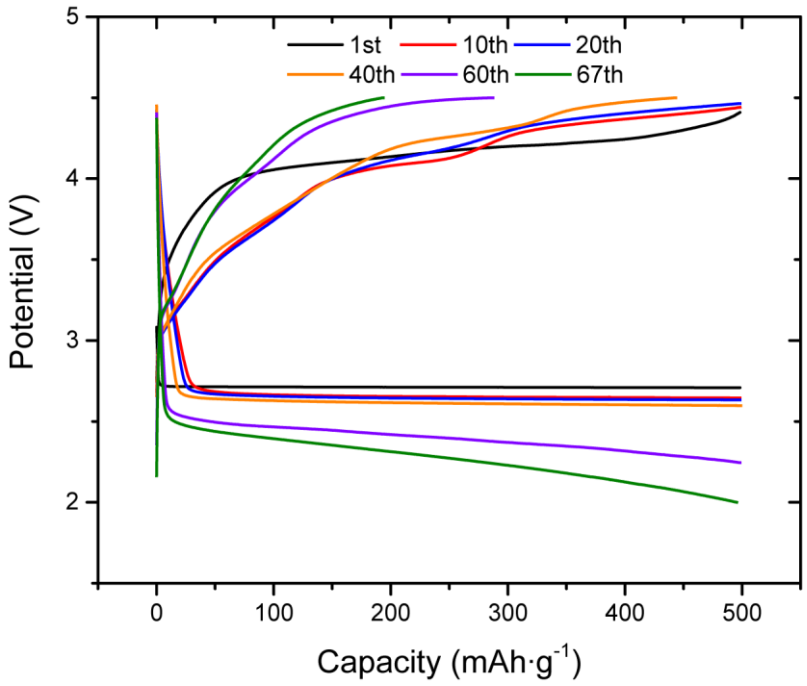

Figure S5.3. The cycling performance of M-CNT-170 cathode at a current density of 200 mA g^{-1} and limited capacity of 500 mAh g^{-1}.

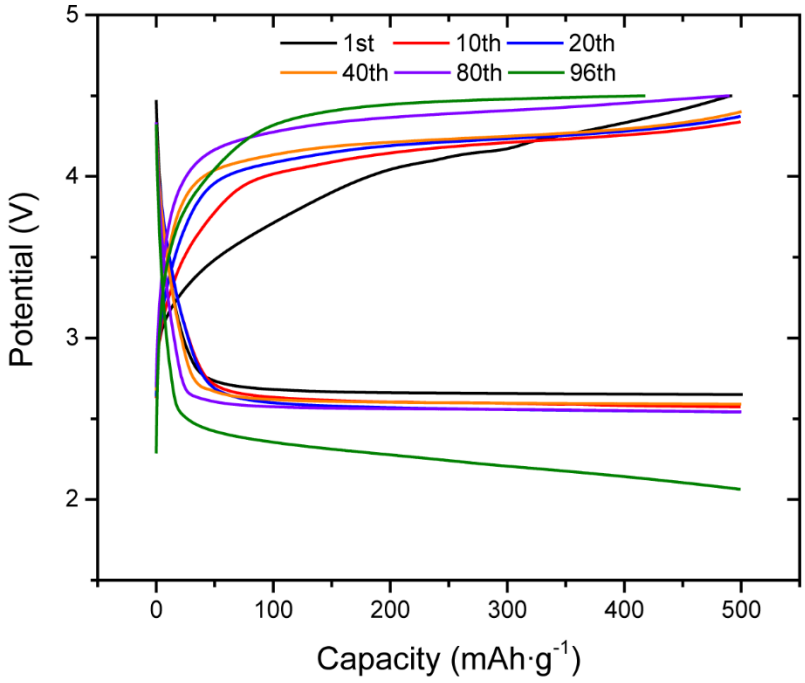

Figure S5.4. The cycling performance of M-LNCO@CNT-170 at a current density of 200 mA g^{-1} and limited capacity of 500 mAh g^{-1}.

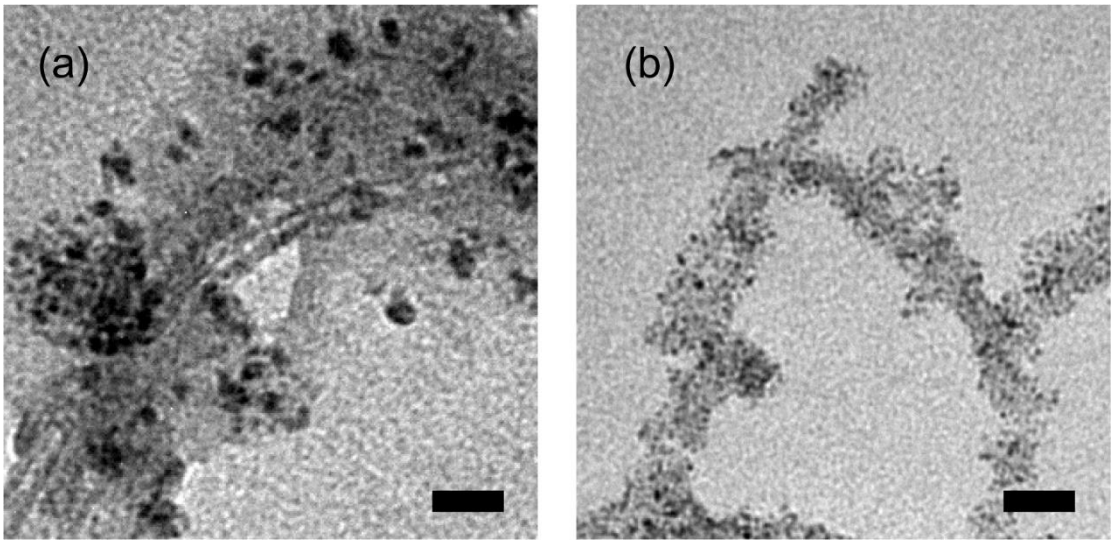

Figure S5.5. The TEM images of the (a) M-NCO@CNT-170 and (b) M-LNCO@CNT-170 cathodes after first discharge, the scale bars indicate 25 nm.

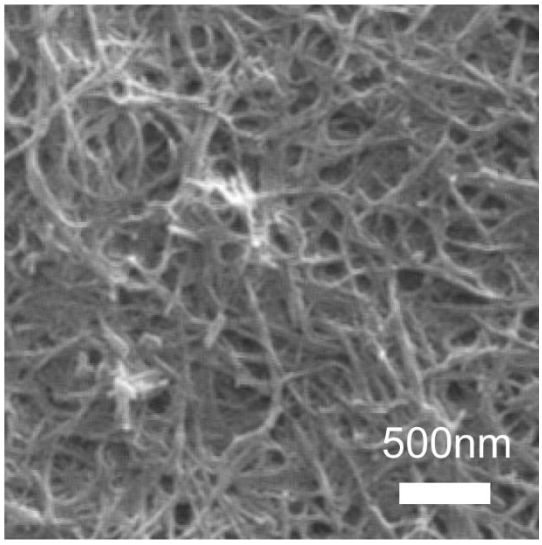

Figure S5.6. The *ex-situ* SEM image of M-NCO@CNT-170 after the first full discharge-charge cycle at a current density of 200 mA g^{-1}.

Table S5.1. Electrochemical performance of the M-NCO@CNT-170 cathode in this study as compared with other NCO-based cathodes reported in literature

Ref	Cathode	Maximum Capacity	Current Density	Limited Capacity	Cycle Number
This work	Freestanding macroporous $NiCo_2O_4$@CNT	6165 mAh g^{-1}	200 mA g^{-1}	500 mAh g^{-1}	343
S1	$NiCo_2O_4$@N-rGO	6716 mAh g^{-1}	200 mA g^{-1}	1000 mAh g^{-1}	112
S2	Pd/PdO on Cr(III)-doped $NiCo_2O_4$	4000 mAh g^{-1}	200 mA g^{-1}	1000 mAh g^{-1}	100
S3	Freestanding $NiCo_2O_4$ nanoneedles @ C fiber	4221 mAh g^{-1}	200 mA g^{-1}	1000 mAh g^{-1}	200
S4	$NiCo_2O_4$ hollow microspheres	8019 mAh g^{-1}	300 mA g^{-1}	1000 mAh g^{-1}	40
S5	$NiCo_2O_4$ rods on Co_3O_4 nanosheets	4386 mAh g^{-1}	0.1 mA cm^{-2}	500 mAh g^{-1}	60
S6	Freestanding $NiCo_2O_4$@N-C fiber	5304 mAh g^{-1}	200 mA g^{-1}	1000 mAh g^{-1}	92
S7	$NiCo_2O_4$@C microspheres	6489 mAh g^{-1}	200 mA g^{-1}	1000 mAh g^{-1}	90
S8	Cr(III)-doped $NiCo_2O_4$	1.23 mAh cm^{-2}	0.1 mA cm^{-2}	0.2 mAh cm^{-2}	45
S9	Freestanding bowl-like $NiCo_2O_4$@C Fiber	9624.2 mAh g^{-1}	100 mA g^{-1}	500 mAh g^{-1}	100
S10	Urchin-like NiO–$NiCo_2O_4$ microsphere	9231 mAh g^{-1}	100 mA g^{-1}	600 mAh g^{-1}	80
S11	3D Foam-Like $NiCo_2O_4$	10137 mAh g^{-1}	200 mA g^{-1}	1000 mAh g^{-1}	80
S12	Freestanding CeO_2@ $NiCo_2O_4$ nanowire array	6300 mAh g^{-1}	100 mA g^{-1}	500 mAh g^{-1}	64

S1 Gong, H.; Xue, H.; Wang, T.; Guo, H.; Fan, X.; Song, L.; Xia, W.; He, J. High-Loading Nickel Cobaltate Nanoparticles Anchored on Three-Dimensional N-Doped Graphene as an Efficient Bifunctional Catalyst for Lithium-Oxygen Batteries. *ACS Appl. Mater. Interfaces* **2016**, *8* (28), 18060–18068.

S2 Gentile, A.; Giacco, D.; De Bonis, A.; Teghil, R.; Marrani, A. G.; Brutti, S. Synergistic Electro-Catalysis of Pd/PdO Nanoparticles and Cr(III)-Doped $NiCo_2O_4$ Nanofibers in Aprotic Li-O_2 Batteries. *J. Electrochem. Soc.* **2018**, *165* (16), A3605–A3612.

S3 Xue, H.; Wu, S.; Tang, J.; Gong, H.; He, P.; He, J.; Zhou, H. Hierarchical Porous

Nickel Cobaltate Nanoneedle Arrays as Flexible Carbon-Protected Cathodes for High-Performance Lithium-Oxygen Batteries. *ACS Appl. Mater. Interfaces* **2016**, *8* (13), 8427–8435.

S4 Zou, L.; Jiang, Y.; Cheng, J.; Gong, Y.; Chi, B.; Pu, J.; Jian, L. Dandelion-Like $NiCo_2O_4$ Hollow Microspheres as Enhanced Cathode Catalyst for Li-Oxygen Batteries in Ambient Air. *Electrochim. Acta* **2016**, *216*, 120–129.

S5 Sennu, P.; Park, H. S.; Park, K. U.; Aravindan, V.; Nahm, K. S.; Lee, Y.-S. Formation of $NiCo_2O_4$ Rods Over Co_3O_4 Nanosheets as Efficient Catalyst for Li-O_2 Batteries and Water Splitting. *J. Catal.* **2017**, *349*, 175–182.

S6 Xue, H.; Mu, X.; Tang, J.; Fan, X.; Gong, H.; Wang, T.; He, J.; Yamauchi, Y. A Nickel Cobaltate Nanoparticle-Decorated Hierarchical Porous N-Doped Carbon Nanofiber Film as a Binder-Free Self-Supported Cathode for Nonaqueous Li-O_2 Batteries. *J. Mater. Chem. A* **2016**, *4* (23), 9106–9112.

S7 Guo, T.; Qin, X.; Hou, L.; Li, J.; Li, X.; Liang, Q. Waxberry-Like Hierarchical $NiCo_2O_4$-Decorated Carbon Microspheres as Efficient Catalyst for Li-O_2 Batteries. *J. Solid State Electrochem.* **2019**.

S8 Giacco, D.; Marrani, A. G.; Brutti, S. Enhancement of the Performance in Li-O_2 Cells of a $NiCo_2O_4$ Based Porous Positive Electrode by Cr(III) Doping. *Mater. Lett.* **2018**, *224*, 113–117.

S9 Wang, J.; Zhan, R.; Fu, Y.; Yu, H.-Y.; Jiang, C.; Zhang, T.-H.; Zhang, C.; Yao, J.; Li, J.-F.; Li, X.; et al. Design and Synthesis of Hierarchical, Freestanding Bowl-Like $NiCo_2O_4$ as Cathode for Long-Life Li-O_2 Batteries. *Mater. Today Energy* **2017**, *5*, 214–221.

S10 Zhao, W.; Li, X.; Yin, R.; Qian, L.; Huang, X.; Liu, H.; Zhang, J.; Wang, J.; Ding, T.; Guo, Z. Urchin-Like NiO-$NiCo_2O_4$ Heterostructure Microsphere Catalysts for Enhanced Rechargeable Non-Aqueous Li-O_2 Batteries. *Nanoscale* **2019**, *11* (1), 50–59.

S11 Liu, L.; Wang, J.; Hou, Y.; Chen, J.; Liu, H.-K.; Wang, J.; Wu, Y. Self-Assembled 3D Foam-Like $NiCo_2O_4$ as Efficient Catalyst for Lithium Oxygen Batteries. *Small* **2016**, *12* (5), 602–611.

S12 Yang, Z.-D.; Chang, Z.-W.; Xu, J.-J.; Yang, X.-Y.; Zhang, X.-B. CeO_2@$NiCo_2O_4$ Nanowire Arrays on Carbon Textiles as High Performance Cathode for Li-O_2 Batteries. *Sci. China Chem.* **2017**, *60* (12), 1540–1545.

Chapter 6 Conclusion and Recommendation

6.1. Conclusions

This thesis aims to develop efficient and stable cathode materials and gain insights into their mechanisms in non-aqueous Li-O_2 batteries. Based on the systematic investigation on the surface atom arrangement and the nanostructure of the $NiCo_2O_4$ (NCO) nanoplates, the syngenetic effect between the NCO nanoplates and reduced graphene oxide aerogel (GA) support and the influence of the NCO@carbon nanotubes (CNT) surfaces on the morphologies and crystallinities of the Li_2O_2 discharge product, the following conclusions are drawn:

(1) NCO nanoplates with identical morphology but exposure to different {111} and {112} crystal planes were synthesized to investigate the crystal plane effect of NCO in Li-O_2 batteries. The contribution of NCO to battery performance is mainly attributed to the improvement of OER rather than ORR. The OER activity of NCO nanoplates is highly dependent on surface atom arrangement. The {112} crystal planes exposed NCO nanoplates show higher OER activity than that of {111} crystal planes. The improved OER activity can be ascribed to the higher density of dangling bonds and the access to the highly active octahedral Co^{3+} and Ni^{3+} sites on {112} crystal planes. The OER activity of NCO is correlated with the surface areas associated with the highly active {112} crystal planes. The presence of Ni^{3+} in crystal lattice plays an essential role in improving the OER activity and the overall conductance of NCO. This work has successfully established the relationship between the crystal plane effect, surface area and Ni^{3+} content on battery performance. The 2D NCO nanoplates can then be used as building blocks for the development of advanced

hetero-nanostructured cathode materials.

(2) A freestanding macroporous nanocomposite of GA and NCO nanoplates cathode was developed through a one-pot self-assembly approach. In this unique nanostructure, NCO nanoplates residing on the walls of the macropores can provide abundant OER active sites and suppress the decomposition of GA, and the macroporous GA support can facilitate electron and mass transfer and act as Li_2O_2 accommodation sites. The macroporous cathode with a weight ratio of GA: NCO = 1: 4 exhibits an optimal ratio, where the NCO nanoplates can adequately cover the walls of macropores without a severe aggregation that hinders the conductivity of the cathode. The macroporous structure can enhance the oxygen and Li ions transport properties, and the freestanding design can avoid the usage of the binder, which is well-known to promote parasitic reactions. Consequently, the macroporous nanocomposite of GA and NCO nanoplates cathode with a weight ratio of GA: NCO = 1: 4 can deliver a specific capacity of 4302 mAh g^{-1} and a cycling performance of 82 cycles. The improved performance can be ascribed to the synergistic effect between GA and an opportune amount of NCO together with the freestanding macroporous structure. This work demonstrates a novel approach to tackle the instability issue with carbon-based macroporous cathode and provides insights into the performance enhancement of solution growth pathway-based Li-O_2 batteries.

(3) The macroporous NCO@CNT cathode was fabricated through a vacuum filtration-assisted self-assembly approach. The NCO-coated CNT surfaces are found to promote the formation of amorphous Li_2O_2 layer through the surface growth pathway, by introducing irregularly arranged LiO_2^* during adsorption and Li defects during

Li_2O_2 growth. Amorphous Li_2O_2 possesses higher conductivity than its crystalline counterpart, which allows the Li_2O_2 layer to grow to a much thicker layer of 50 nm, increasing the Li_2O_2 production before cathode surfaces are fully passivated. As a result, the Li_2O_2 discharge product can fill the macropores in the cathode with a high cathode utilization ratio, leading to a high discharge capacity of 6165 mAh g^{-1} at 200 mA g^{-1} that is comparable to the macroporous CNT cathode via the solution growth pathway. The amorphous Li_2O_2 layer is in close contact with cathode surfaces and can be facilely decomposed during OER, which attributes to the excellent cycling performance of 343 cycles at 200 mA g^{-1} and 500 mAh g^{-1} that overpasses previous reports. Based on the morphology of Li_2O_2, the macroporous NCO@CNT cathode with a pore size of 100-200 nm shows the optimal pore structure to allow Li_2O_2 to fill the macropores with a high cathode utilization ratio. This work has demonstrated the viability of Li-O_2 batteries based on the unconventional surface growth pathway, which can be a promising approach for further high-performance Li-O_2 batteries.

Through these investigations, the correlations between the nanostructures of the cathode materials and the battery performance are uncovered, and both the solution growth pathway and surface growth pathway approaches proposed in Section 2.4 have been systematically studied. The output of this thesis furthers our understandings of the mechanisms of the battery and guides the rational cathode design for large capacity, high efficiency and long lifespan Li-O_2 batteries for a wide range of energy storage applications.

6.2. Future Perspectives

In this project, significant progress on the development of cathode materials has been made to benefit the development of future high-performance Li-O_2 batteries. Future opportunities

stemmed from this research are suggested:

(1) Although the crystal plane effect of NCO has been experimentally demonstrated, the exact mechanism is still unclear. It is suggested that the Ni^{3+} on the octahedral sites may be more catalytic active than Co^{3+}. Computational studies such as density functional theory can be used to clarify the function of Ni^{3+} in electrochemistry. This enables more options for fine tuning the surface atom arrangement, such as cation ordering and surface segregation of Ni^{3+}, for high-performance Li-O_2 battery.

(2) For the macroporous nanocomposite of GA and NCO nanoplates cathode, the large macropores are not efficiently filled by the Li_2O_2 discharge product, and the capacity can be improved further by growing larger Li_2O_2 toroids. Optimization of the electrolyte, such as a high donor number solvent, will promote the growth of larger Li_2O_2 toroids via the solution growth pathway. Redox mediators can be considered to facilitate the oxidation of large Li_2O_2 particles. The stability of the overall system can be compromised by the utilization of high donor number solvent and redox mediators that can introduce more parasitic reactions. Therefore, the cathode design in which NCO nanoplates act as a protective layer for GA support is more valuable in this situation. In addition, the NCO nanoplates are currently bonded with GA through physical interaction. To introduce a large amount of NCO on GA via stronger chemical bonds without compromising the porous structure of the GA support, alternative synthesis routes can be explored, such as growing a protective NCO layer via electrodeposition.

(3) For the macroporous NCO@CNT cathode, the template method, unfortunately, cannot generate highly ordered macroporous cathodes, possibly due to relatively

rigid NCO@CNT nanotubes. This irregularity in pore distribution can reduce the cathode utilization ratio and discharge capacity of the battery. Therefore, an alternative fabrication method that helps to produce ordered macrospores can be explored. In addition, the mechanism of the unique amorphous Li_2O_2 formation is not well-understood. More work is needed to clarify whether this phenomenon is exclusive to the macroporous NCO@CNT cathode, which will help future cathode design based on surface growth pathway.